University of Genova- Istituto Italiano di Tecnologia

Bionanotechnology (DIBRIS)

XXXII cycle

Design and Fabrication of Polymeric Coatings based on Sustainable Materials and Processes

Doctor of Philosophy (PhD) Thesis

Sara Naderizadeh

S4169431

Tutors:

Dr. Athanassia Athanassiou

Dr. Ilker. S. Bayer

Smart Materials Group

2020

Reviewers:

Dr Hab. Konrad Terpilowski

Dr Ugur Cengiz

Thesis submission: Feb 2020

Thesis dissertation: March 2020

Mom and Dad, I have no words to aknowledge the sacrifies you made and the dreams you had to let go, just to give me a shot at achieving mine.

And my sisters that always encourage me in my life to go ahead.

I love you so much

Acknowledgements

I am very thankful to achieve at this stage in my life and career. Surely, I could not get where I am now without the help and support of many people.

First and foremost thanks to Dr. Athanssia Athanassiou who has been as my supervisor for the whole 3 years of PhD. Her understanding, patience and generous guide and support, provided me to work in an interdisciplinary environment at Smart materials group.

I am grateful to Dr. Ilker S. Bayer who was supervising me during all my research activities and being supportive to extend the constructive ideas. His motivation, immense knowledge and impressive guidance helped me to carry out this research.

My sincere thanks also go to Prof. Dimos Poulikakos and Dr. Athanasios Milionis and their group at Laboratory of Thermodynamics in Emerging Technologies, Department of Mechanical and Process Engineering, ETH university in Zurich, who provided me an opportunity to join their team during my PhD and who gave access to the laboratory and reseach facilites.

Many thanks to Dr. Jose A. Heredia-Guerrero for his help and kindness in chemical analysis.

My thanks also go out to our technicians in Smart materials group Lara Marini, Giorgio Mancini and Riccardo Carzino. This work would not be materizalized without their availability, infinite support and help.

Also thanks to Luca Ceseracciu, Simone Lauciello, Doriana Debellis, Marco Salerno and Silvia Dante for their help with different measurements.

I would like to express my gratitude and many thanks to all my friends that made my time in IIT very pleasant. I feel the need to thank each of them personally at the end of this work.

My special thanks to Dr. Javad Shamsi for his kindness and paitence in these 3 years that I would never forget. His attendance here gave me the strength to continue over adversities.

Last but not least, I would like to appreciate my lovely parents and my sisters that they really support me beyond the frontiers that without their comprehensive support I could not dream about reaching to this level in my life. Whitout them nothing would have been possible.

Declaration

I hereby declare that except where specific reference is made to the work of others, the contents of this dissertation are original and have not been submitted in whole or in part for consideration for any other degree or qualification in this, or any other University. This dissertation is the result of my own work and includes nothing which is the outcome of work done in collaboration, except where specifically indicated in the text. This dissertation contains less than 40,000 words including appendices, bibliography, tables and equations and has less than 70 figures.

Sara Naderizadeh

2020

Scientific publications

1. **Interfacing superhydrophobic silica nanoparticle films with graphene and thermoplastic polyurethane for wear/abrasion resistance.**

   Sara Naderizadeh, Athanassia Athanassiou, Ilker S Bayer. Journal of colloid and interface science, **2018**.

2. **Superhydrophobic Coatings from Beeswax-in-Water Emulsions with Latent Heat Storage Capability.**

   Sara Naderizadeh, José Alejandro Heredia-Guerrero, Gianvito Caputo, Silvia Grasselli, Annalisa Malchiodi, Athanassia Athanassiou, Ilker S Bayer. Advanced Materials Interfaces, **2019**.

3. **Stacked-Cup Carbon Nanotube Flexible Paper Based on Soy Lecithin and Natural Rubber.**

   Amirreza Shayganpour, **Sara Naderizadeh**, Silvia Grasselli, Annalisa Malchiodi, Ilker S. Bayer. Nanomaterials, **2019**.

4. **Green Biocomposites for Thermoelectric Wearable Applications.**

   Pietro Cataldi, Marco Cassinelli, José A Heredia-Guerrero, Susana Guzman-Puyol, **Sara Naderizadeh**, Athanassia Athanassiou, Mario Caironi. Advanced Functional Materials, **2019**.

5. **Bioresin-based Superhydrophobic Coatings with Reduced Bacterial Adhesion.**

   Sara Naderizadeh, Silvia Dante, Pasquale Picone, Marta Di Carlo, Riccardo Carzino, Athanassia Athanassiou, Ilker S. Bayer (Under submission in Journal of Colloids and Interface Science), **2020**.

6. **Thermally Conductive Coating Decorated by In-Situ Synthesized Silver Nanoparticles and Graphene Nanoplatelets.**

   Sara Naderizadeh, Muhammad Zahid, Amirreza Shayganpour, Athanassia Athanassiou, Ilker S. Bayer (Under Preparation).

Communications at Conferences

Oral

1. **S. Naderizadeh**, A. Athanassiou, I. S. Bayer

   "Water-repellent coating based on Thermoplastic Polyurethane, Silica Nanoparticles and Graphene Nanoplatelets" ICP 2018, 20th International coference on Polymer. 19-20 Feb 2018. Paris, France.

2. **S. Naderizadeh**, A. Athanassiou, I. S. Bayer

   "Superhydrophobic coatings from water-based beeswax emulsions" 4th edition of International conference on Polymer Science. 4-5 June 2018. London, United Kingdom.

3. **S. Naderizadeh**, J. A. Heredia-guerrero, G. Caputo, S. Grasselli, A. Malchiodi, A. Athanassiou, I. S. Bayer

   "Superhydrophobic coating based on phase-change material and its application in thermal management" ECS 2019, 13th European Coating Symposium. 8-11 Sep 2019. Heidelberg, Germany.

Poster

1. **S. Naderizadeh**, M. Zahid, A. Shayganpour, A. Athanassiou, I. S. Bayer

   "Thermally conductive polymer coating decorated with in-situ synthesized silver nanopartilces and graphene nanoplatelets" EPF 2019, European Polymer Congress. 9-14 June 2019. Crete, Greece.

Table of Contents

List of Figures

List of Tables

List of Acronyms and Abbreviations

Layer-by-layer deposition	LBL
Chemical vapout deposition	CVD
Contact angle	CA
Roll-off angle	RA
Sliding angle	SA
Contact angle hysteresis	CAH
Zinc oxide	ZnO
Specific heat capacity	C_p
Phonon velocity	v
Phonon mean free path	l
Interfacial free energy per unit of solid-gas interface	γ_{sv}
Interfacial free energy per unit of solid-liquid interface	γ_{sl}
Interfacial free energy per unit of liquid-gas interface	γ_{lv}
Perfluorooctanoic acid	PFOA
Perfluorooctane sulfonate	PFOS
Environmental protection agency	EPA
Perfluorohexanoic acid	PFH*x*A
Silica nanoparticles	Si-NPs or SiO_2
Polydimethylsiloxane	PDMS
Hexadecyltrimethoxysilane	HDMTS
Octyltriethoxysilane	OTES
Trichloro(octadecyl)silane	OTS
Carbon nanotubes	CNTs
Boron nitride	BN
Silicon nitride	SN
Thermal conductivity	k
Thermal diffusivity	α

Density	ρ
Light emitting diode	LED
Ultraviolet	UV
Langmuir-Blodgett	LB
Thermoplastic polyurethane	TPU
Graphene nanoplatelets	GnPs
Aluminum	Al
Scanning electron microscopy	SEM
Energy dispersive X-ray	EDX or EDS
Atomic force microscopy	AFM
Quantitative imaging	QI
Fourier transfrom infrared	FTIR
Attenuated total reflectance	ATR
UV-Visible spectroscopy	UV-Vis
Near infrared	NIR
Diffrential scanning calorimetry	DSC
Thermogravimetric analysis	TGA
X-ray diffraction	XRD
Dynamic light scattering	DLS
Bis(triethylsilyl)amine or hexamethyldisilazane	HMDS or $HN[Si(CH3)_3]_2$
Weight percentage	wt%
Built-in grain statistical algorithm	Watershed
Octadecylphosphonic acid	ODP
Poly carbonate	PC
Poly methylmethacrylate	PMMA
Dimethyldichlorosilane	DDS
Vinyltriethoxysilane	VTES
Interpenetrating polymer network	IPN
Polyethylene terphethalate	PET

Indium tin oxide	ITO
Titanium dioxide	TiO_2
Calcium carbonate	$CaCO_3$
Perfluorinated acrylic copolymer dispersion in water	Capstone ST-100 or PFAC
Transmission electron microscopy	TEM
X-ray photoelectron spectroscopy	XPS
Infrared camera	IR-camera
Room temperature	R.T
Full width at half of the maximum of the peak	FWHM
Furfuryl alcohol	FA
Polyfurfuryl alcohol	PFA
Trifluoroacetic acid	TFA
Dulbecco's modified Eagle medium	DMEM
Phosphate-buffered silane	PBS
Bovine serum albumin	BSA
Cell index	C.I.
Escherichia coli	*E.coli*
Staphylococcus aureus	*S.aureus*
Crystal violet	CV
Skewness	Ssk
Kurtosis	Sku
Silver nanoparticles	Ag NPs
Carbon nanofibers	CnFs
Silver trifluoromethanesulfonate or silver triflate	$AgCF_3SO_3$
Silver ions	Ag^+
Silver particles	Ag^0
High resolution scanning electron microscopy	HRSEM
Sodium borohydride	$NaBH_4$

Sodium citrate	$Na_3C_6H_5O_7$
Hydroquinone	$C_6H_6O_2$
Sodium hydroxide	NaOH
Surface plasmon resonance	SPR
Area under the crystalline peak	A_{cryst}
Area under the amorphous peak	A_{am}
First derivative thermogravimetric analysis	DTGA
Edge length of a square film	L
Distabce from the hot plate	x
Sample Temperature	T
Hot plate temperature	T_0
Ambient temperature	T_a

Overview

Polymeric coatings are getting more and more popular, due to their enhanced technical properties. Conventional coatings can be more practical by means of surface modifications to change the surface characteristics such as wetting properties, adhesion, conductivity and etc. This thesis will aim to provide an understanding about some surface properties and tuning the surface composition to obtain a final applications of the polymeric coatings. For this, different polymer nanocomposites were used by focusing on the sustainability of the materials and the simple fabrication process to have the chance to make them in large scale applications. After a general introduction about polymeric coatings, wetting properties, liquid repellent and thermally conductive coatings some of the materials and the methods, which can be used to fabricate these coatings and some applications of them are discussed in chapter 1.

Subsequently, this thesis have been categorized into 5 independent sections with detailed results and discussions about each project that were done during this PhD thesis, followed by a general summary and conclusion. Each of this chapters are about:

Chapter 2. Interfacing superhydrophobic silica nanoparticle films with graphene and thermoplastic polyurethane for wear/abrasion resistance

Chapter 3. Superhydrophobic Coatings from Beeswax-in-water Emulsions with Latent Heat Storage Capability

Chapter 4. Biocompatible liquid-repellent coating with anti-bacterial adhesion property

Chapter 5. Thermally condcutive polymer coating decorated with in-situ synthesized silver nanoparticles and graphene nanoplatelets

Chapter 6. Prespective and future ideas

Chapter 1

Introduction and Literature Review

Coatings history refers further into the past, when most of the prehistoric coatings were only decorative such as painting of the art works. However, today's coatings can be applied for both decorative and protective aspects. These coatings are used for dual aspects, protecting the underneath substrate from corrosion or other possible damages and being decorative. Surface coatings are recognized as an enabling technology with high level of importance in engineering function to obtain an effective exploitation of materials. Involving as they do both the improvement and enhancement of conventional materials in enginerring applications and synthesis of novel materials according to the characteristics of the surface coatings. It means that the final material can show the benefits both from the underneath material and the upper surface coatings, simultaneously.

Polymeric materials are present in our life, from nature-based materials such as polysaccharides and proteins to synthetic plastics and fibers. Their application covers a broad range of demanding areas, like packaging, aerospace, aviation, medical devices and many various industrial applications. These materials are the large molecules, composed of small repeating units, which can have different characteristics depends on the molecular stuctures. One of the most important applications of polymeric materials is the field of polymer coatings comprising industrial paints and adhesives. Some of the applications of polymeric coatings are summarized in Figure 1.

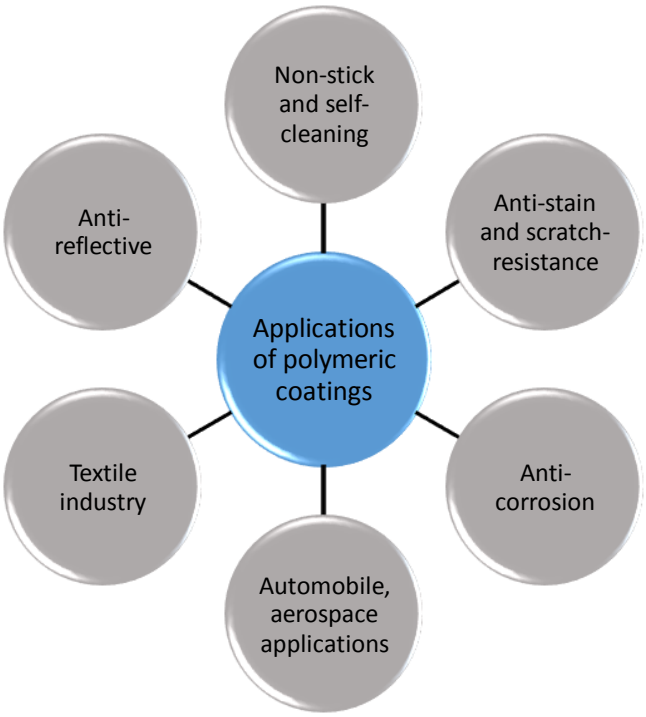

Figure 1. Some of the applications of the polymeric coatings.

The techniques to apply a polymeric coating can be devided into simple brushing or spray coating, spin-coating, dip-coating, sol-gel processing, layer-by-layer deposition (LBL), chemical vapour deposition (CVD), specialized and expensive machinary systems, especially for electronic industry, printing and etc. Depends on the types of the materials, surface area to cover and the final application of the coatings, each of these methods can be used. Among all these techniques, spray coating is considered as one of the most efficient and cheapest one to cover a large area of the surface. The polymer coatings can be applied on different surfaces by using various methods. The underneath substrates can be glass, metals, textiles, papers and etc.

Nowadays, functional coatings could be utilized to change the surface characteristics such as wettability, adhesion, corrosion resistance or add some new properties like anti-bactrial, thermal or electrical conductivity and etc. In this area, functional polymers and special nanoparticles play a key and significant role to obtain an outstanding surface properties compared to the bulky materials.

The objective of this study is to focus on development of liquid-repellent and the conductive coatings, which will be discussed with more details.

1.1. Liquid-repellent polymeric coatings

Wettability has a direct impact on the surface morphology, which has the final effect on the surface behaviour. Here some explanations about the wettability are breifly described.

1.1.1. Wetting parameters

Different wetting behaviours are distinguished with two parameters, namely as static contact angle (CAs) and sliding angles (SAs). Static contact angle is the angle in an interface existing between the liquid and the solid surface. However, the sliding angle, which is called the roll-off anlge (RAs), is the angle between the horizontal line and the tilting surface, where all the liquid droplets roll away on the surface [1]. Another important parameter in wetting characteristics is the contact angle hysteresis (CAH), which is the difference between advancing and receding contact angles, maximum and minimum contact angles, respectively, on the tilted surface, when the droplets is moving. One example is the rain drops on the window; which the gravity force pulls down the droplets, while hysteresis keep them in place. Figure 2 shows a schematic of the wetting parameters explanation.

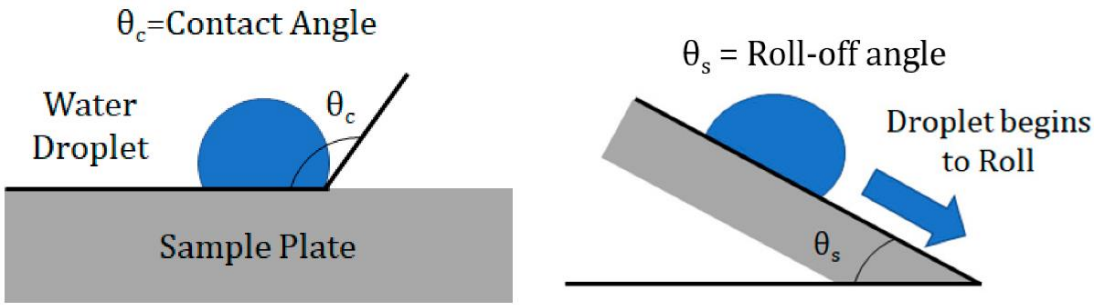

Figure 2. Schematic of illustration of CAs and RAs [2].

1.1.2. Different wetting models

1.1.2.1. Young's equation for flat surfaces

If the solid surface is assumed as a smooth and flat surface, the young's equation is applied to study the surface characteristics, which is explained as follows (See equation 1). This equation displays the equilibrium between the solid surface and the liquid.

$$\cos\theta = (\gamma_{sv} - \gamma_{sl}) / \gamma_{lv} \qquad \textbf{Equation 1}$$

where γ_{sv}, γ_{sl} and γ_{lv} are the interfacial free energies per unit of the solid-gas, solid-liquid and liquid-gas interfaces. According to this equation, the only method to increase the hydrophobicity of the surface is to decrease the surface energy of the solid. The lowest value for the surface energy is estimated around 6.7 mJ m^{-2}, which is attributed to the surface with regularly aligned hexagonal close-packed CF_3 groups, with maximum CA around 120˚ [3–5].

1.1.2.2. Wenzel state and Cassie-Baxter state for textured surfaces

However, if there is roughed structures on the surface or about the textured surface, there are two main states of liquid-solid interactions, namely as Wenzel and Cassie-Baxter states [6,7]. These two models are described below (See Figure 3).

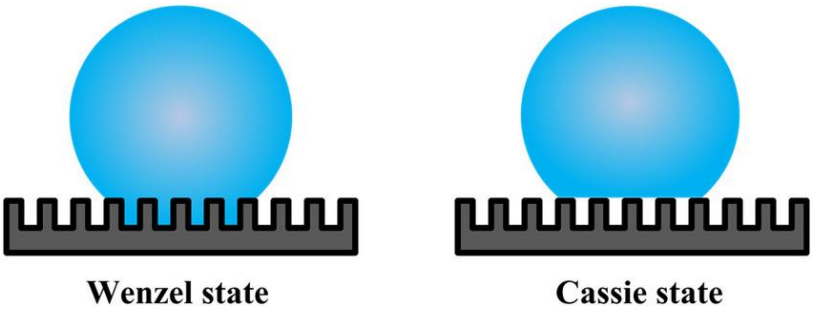

Figure 3. The illustration of Wenzel and Cassie-Baxter states [8].

Wenzel or wet state refers to the contact of the liquid droplets with each point on the solid surface, while Cassie-Baxter or dry state describes the state that liquid droplets are in contact with only top features of the solid surface [9].

These two models can be merged into a general model to cover the state that the contacting area are not smooth by themselves. From this combination, it can be concluded that not only by decreasing the surface energy, but also by increasing the surface roughness, the hydrophobicity of the surface can be improved [10].

1.1.3. Different wetting behaviours

According to the wetting properties, the behaviours were classified into four groups, namely as superhydrophobic, hydrophobic, hydrophilic and superhydrophilic ones. Depends on the surface chemistry, surface roughness, surface energy and final application, each of them can be fabricated through different materials and methods. Liquids usually show non-spreading behaviour on the low surface energy solids [11]. Figure 4 displays the different wetting behaviours.

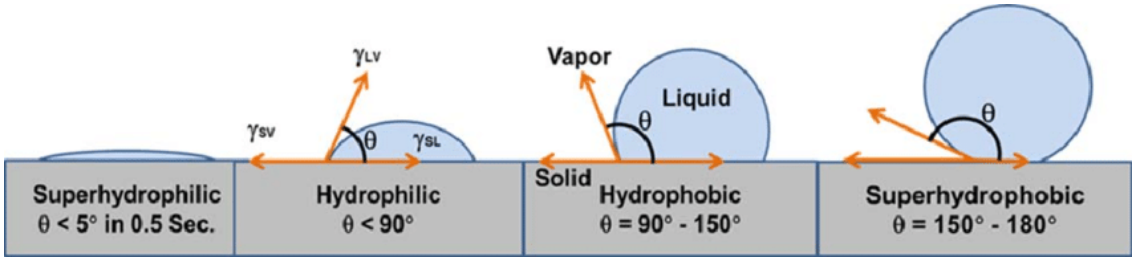

Figure 4. The concept of different wetting behaviours [12].

As it can be seen in Figure 4, the CAs define the wetting behaviour of the surface. If the CA is smaller than 90˚, the surface is regarded as hydrophilic, while the superhydrophilic surface is considered as a surface with compelete wetting (CA near 0˚). On the other hand, if the CA increase more than 90˚, the surface is hydrophobic, and if it is larger than 150˚, then the surface is regarded as superhydrophobic ones, which is close to the non-wetting state. However, Vogler et.al. showed that the real boundary for hydrophobic to hydrophilic region is 65˚ rather than 90˚, which is coming from the repulsive forces between surfaces and some experimental results. According to this theory flat surfaces with contact angles less than 65˚ will be more hydrophilic by increasing the surface roughness parameters, while the surfaces with contact angles more than 65˚ will be more hydrophobic by increasing the surface roughness [13–15].

Here, in this thesis it will be more focused on the superhydrophobic surfaces, so the characteristics of this kind of surfaces will be discussed with more details.

1.2. Superhydrophobic surface characteristics

1.2.1. Lotus leaf structure

Inspiring from nature is always creates new ideas for the researchers towards a “biomimetic surfaces”. Some plants and animals have evolved in such a way that their surface can remain dry and clean naturally. For example this phenomena can be seen in lotus leaf, which has two levels of micro and nano structures on the surface that composed of micrometer-scale bumps and nano-scale hair-like structures (See Figure 5). Low surface energy waxes supported by micro/nano-structured papillae (2-5 μm) are the main responsible for superhydrophobicity and self-cleaning properties of the lotus leaf [16,17], which causes the high water CA and low RA around 160˚ and 2˚, respectively. In this kinds

of surfaces by trapping air under the water droplets on the surface, the water CAs increased and droplets can be rolled on the surface to maintain the surface dry and clean. However, lotus leaf is not the only example of superhydrophobic surface in nature, there are many of other plants or animals that has this property, which they have been widely studied by different groups like Neinhuis and Barthlott [18,19], Cerman and co-wokers [20], Guo and Liu [21] and etc. Some of these surfaces are rice leaf, India canna, taro leaf, rose petals, butterfly's wing, duck feathers, gecko feet and etc [19,22]. All these surfaces have been attracted researchers to mimic them and obtain similiar characteristics in artifial surfaces, due to the broad range of applications, which have been increasing exponentially since 2000s [23–26].

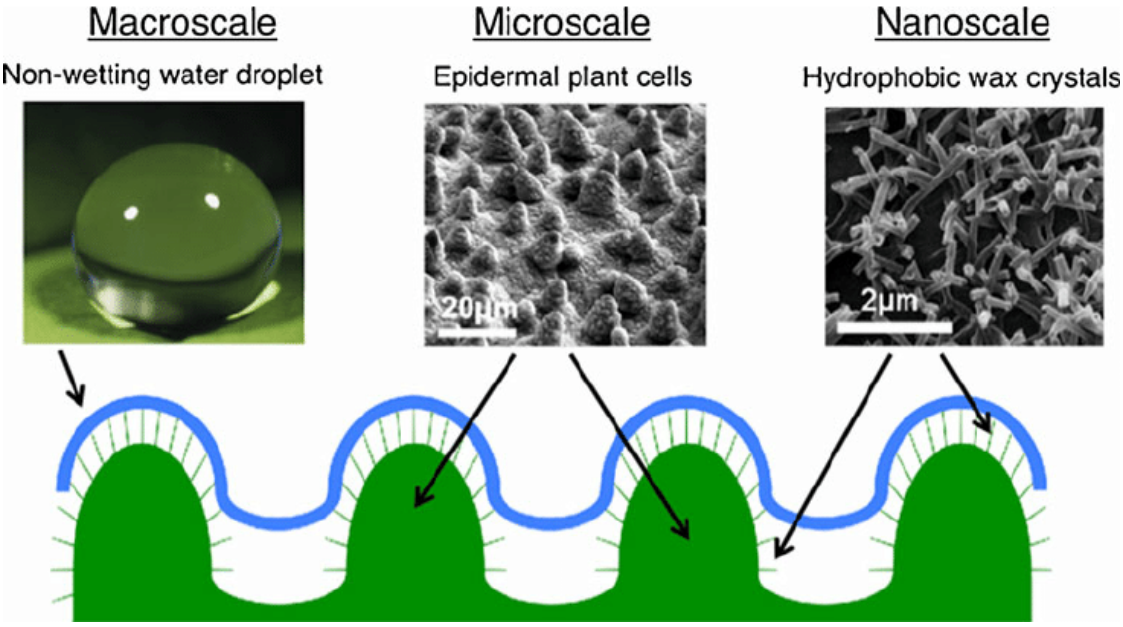

Figure 5. The hierarchical surface structure of the lotus leaf at the micro- and nanoscale [27].

Similiar synthetic surfaces could be fabricated by designing the surface with some micro-nano heirarchical stuctures and also focusing on the surface chemistry by applying a great variety of organic and inorganic materials using different techniques. Here, some of the selected materials and the more common techniques, which are using to fabricate the superhydrophobic coatings will be discussed as follows.

1.2.2. Common approaches to obtain superhydrophobicity

These coatings can be produced by using different composites, composed of dispersed nanoparticles into the polymer matrix or even by fabrication of nanoparticle films. Surface modification techniques by using low surface free energy materials, such as fluorinated polymers and incorporated nanostrctures such as modified silica nanoparticles, Zinc oxide (ZnO) nanorods and etc are the great

interest for industry and academia [28,29]. Here some of the approaches that can be used in the fabrication of superhydrophobic surfaces are breifly discussed.

1.2.2.1. Sustainable processes

Using the sustainable materials and processes are more common recently, due to the environmetal issues by pertoleum-based materials or using some organic solvents, which causes toxicity or bioaccumulation hazards [30]. Sustainability in the composition can be obtained by using biodegradable and natural materials like cellulose-based [31], natural wax-based materials [32], silicone-based biocompatible materials [33] and fluorine free substances [34]. Furthermore, the fabrication process also can be sustainable by using waterborne spray systems [35,36], green solvents including alcoholic solvent environment [37] and etc.

1.2.2.2. Bio-based materials

The application of bio-based materials in the fabrication of superhydrophobic surfaces is increasing, due to the environmental pollution, low cost and high availability of these materials. These materials can be hydrophobic by themselves like wax materials or even they can be hydrophilic such as starch, polyfurfuryl alcohol and etc and can be treated with low surface energy materials to act as a hydrophobic material.

One of the key componenet in lotus leaf structure is the natural wax in the form of wax tubules, which makes this surface a superhydrophobic ones with self-cleaning properties [36]. For instance, a superhydrophobic coating was fabricated based on the blend of two types of edible and natural waxes, namely as beeswax and carnauba wax [32]. The material was applied through a simple and cheap spray coating method. The low surface energy plus the microscale rough structures on the surface, was the main responsible for the superhydrophobicity behaviour.

1.2.2.3. Fluorinated polymers

More than the sustainable materials and processes, fluorinated polymers, especifically those that have C8 chemistry (with long fluorinated chains), shows a low surface free energy around 18 mN m^{-1} [38], which can be used to transform the surfaces to hydrophobic ones. Despite their good water-repellency, C8 fluorinated polymers are considered as a hazardous material for the environment, due to the degradation of these materials into perfluorooctanoic acid (PFOA) and perfluorooctane sulfonate (PFOS). The produced compounds have very low bio-elimination rate and they are regarded as carcinogenic materials [39,40]. So, the Environmental protection agency (EPA) forbids the use of these kinds of polymers and asked the major manufacturers to replace them with some of the environmentally-friendly polymers [41]. So, the new C6 fluorinated polymers with ≤ 6 fluorinated carbon atoms were developed to substitute the previous versions. This new type of fluorinated

polymers are considered as environmentally-friendly polymers, which degrade into perfluorohexanoic acid (PFH*x*A) that has high bio-degradation rate [42].

Fo instance, a simple procedure was used to fabricate a transparent superhydrophobic coating and a translucent superamphiphobic coating through spray coating silica-fluoropolymer hybrid nanoparticles without any treatment on the substrate. The micro/nanoscale rough structures was created by the nanoparticles and the fluoropolymer acts as a low surface energy matrix. By increasing the silica nanoparticles concentration the transition between superhydrophobic/transparent and superamphiphobic/translucent states was facilitated. This transition caused by increment in the discontinuities in the three-phase (solid-liquid-gas) contact line and in the light-scattering characteristics, which is occured by changing the nanoparticles concentration that affects on the micropapillae [43].

1.2.2.4. Silicon-based polymers

One of the most common materials to produce superhydrophobic surfaces is the one utilizing silicone polymers such as PDMS, polydimethylsiloxane. For example, a superhydrophobic surface was produced by using ZnO nanoparticles blended into PDMS, by a simple wet chemical process [44]. The ZnO nanopaowders with average particle size around 14 nm were synthesized through a low-temperature solution combustion techniqus. The fabricated coating from these nanomaterials shows the water CA around 108˚, however after modification with PDMS, the CA increased to 155˚ and the RA was recorded as <5˚ and the surface became superhydrophobic. Here, the superhydrophobicity is acheived by creation of roughed surface from assmebling of ZnO nanopowders by using the benefit of the hydrophobicity of PDMS.

PDMS is not the only silicone-based matrix, which is used in the fabrication of superhydrophobic surfaces. The other silicone-based materials are inclusing, hexadecyltrimethoxysilane (HDMTS) [45], octyltriethoxysilane (OTES) [46,47], trichloro(octadecyl)silane (OTS) [48] and etc.

1.2.2.5. Nanoparticle films

Various superhydrophobic surfaces can be fabricated by deposition of nanopartilce layers on different sublayers. It's worth noting that the nanoparticle surface should be hydrophobically functionalized [49]. For example, a transparent superhydrophobic nanoparticle film was produced by using silica nanoparticles [50]. The nanoparticle films were fabricated by using layer-by-layer assembly technique. This method was used to control the level of aggregation and the location of different sized nanoparticles, to fabricate a multilayer nanoparticle film. Due to the optimization of surface roughness followed by a really low CAH, the light scattering was diminished. Along with

superhydrophobicity, the high level of transparency was achieved, with very low reflectivity at specified visible wavelengths.

1.2.3. Various techniques to fabricate the superhydrophobic surfaces

The techniques to fabricate the superhydrophobic surfaces usually needs the roughening of the surface to obtain a micro-nanostructures on the surface, followed by surface modification, which causes to acheive the low surface energy. Some methods like solution-immersion process, spray coating and electrodeposition are based on the surface modification with coating materials after surface roughening, while the other methods such as template deposition and laser electrodeposition do not require any surface modifications. What's important is the durability, corrosion resistance and storability of the superhydrophobic coatings, regardless of the method that is used to fabricate them [51]. Another important issues are the time consumption, cost-effectiveness, versatility and the possible large-scale production of the suerhydrophobic coatings. The other techniques including lithography, layer-by-layer deposition (LBL), chemical vapor deposition and etc can also be used to fabricate this kinds of surfaces.

1.2.4. Applications of superhydrophobic surfaces

Water-repellent surfaces and coatings as mentioned earlier have a unique behaviour towards water droplets, which opens the new applications for these surfaces, including self-cleaning [52], anti-icing [53], anti-bacterial [54], corossion resistant surfaces [47] and the materials for oil-water separation [55] and etc. In all these applications, the important issue is the existance of hydrophobic materials, as well as the surface roughness.

1.3. Thermally-conductive polymeric coatings

Today, by advancement in the miniaturizing and integrating electronic components, the challenges about thermal dissipation is getting more important. Thermal dissipation becomes a challengng problem in the fabrication of flexible electronics and light emitting diodes. Therefore, efficient thermally conductive materials are being critical to to help address this challenge [56,57].

In solid materials, heat can be transfered via charge carriers, such as electrons and holes or via phonons. For semiconductors and insulators, the heat transportation is through the contributions of phonons, while for metals the electronic contribution is playing the main role. For most of the polymers, thermal conductivity is due to the phonons contribution [58]. The thermal conductivity of the polymers is described by the following equation (equation 2) that is called Debye equation:

$$k = C_p \nu l / 3 \qquad \textbf{Equation 2}$$

Where C_p is the specific heat capacity per unite volume, v is the phonon velocity and l is the phonon mean free path. For most of the polymers, due to the scattering with other phonons, defects and grain

boundries, *l* is extremelly small, which causes the low thermal conductivity in the range of 0.1 - 0.5 W/mk. This level of thermal condcutivity is not enough for many applications that needs higher heat transfer [59]. Despite the low thermal conductivity in polymers, they have other advantages such as light weight, corrosion resistance, low cost and good processability. According to these benefits, polymer-based thermally conductive composites are desirable for many applications. In the following section, more details about the these types of coatings are disscused.

1.3.1. Thermally-conductive fillers

There are many heat conductive fillers, including carbon nanotubes (CNTs) [58], graphene [60], metal particles [61], ceramic materials [62] and etc, which can be introduced into the polymer matrix to obtain a highly thermal conductive composites. The thermal conductivity of the final composites is based on the conductivity of both polymers and the fillers, however this value for the polymers is really low respect to the condcutive fillers, which can be neglected. The key parameter in this case, is the creation of continuous filler network in the polymer matrix to allow heat transportation, which is depends directly to the filler content [63]. As the filler loading level increased, this netwrok formation may behave inversly, causes poor processability, poor mechanical properties and high cost, which is not good in many applications. The interactions between polymer and fillers is also critical in thermal conductivity of the final composites. Imroving the interfacial interactions between the components can improve the thermal conductivity of the composite [59].

The other parameters are the filler type, loading level, filler shape, geometry and filler size. Here, the schematic illustration of some conductive fillers with different shape are shown in Figure 6.

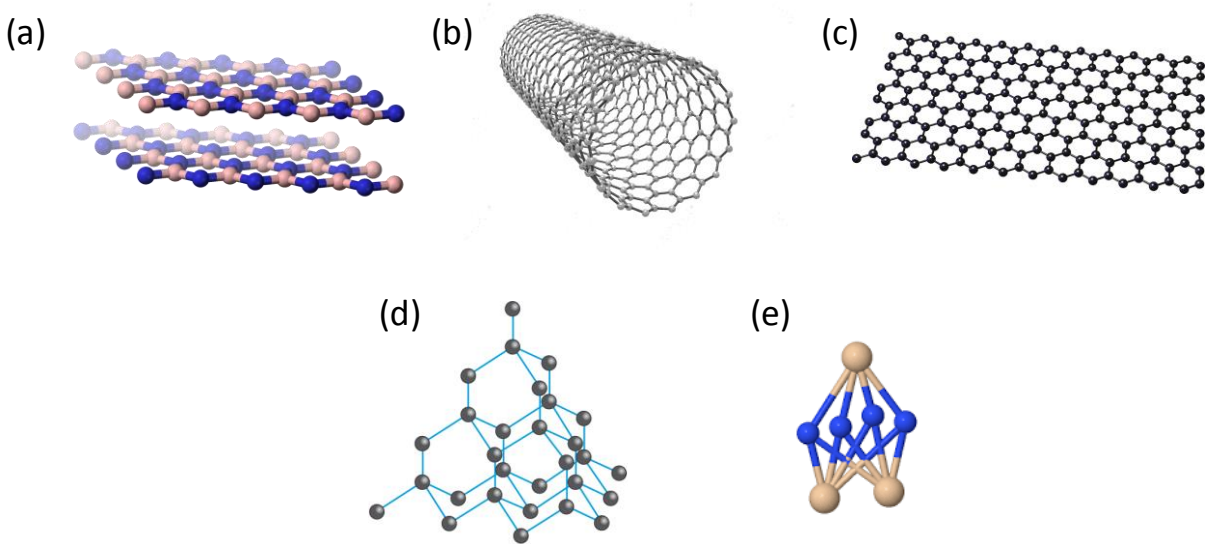

Figure 6. The schematic illustration of (a) boron nitride (BN), (b) carbon nanotubes, (c) graphene nanosheets, (d) diamond and (e) silicone nitride (SN), as thermally conductive fillers.

1.3.2. Thermally-conductive measurement techniques

The main techniques to measure the thermal conductivity is divided into two groups, namely as steady-state and transient methods. Steady-state methods are used when the system reached to stable state, means that temperature changes across the sample, but is generally time-independent. Then the thermal conductivity is measuring based on the calculations of heat flux and temperature gradient. These techniques include the hot plate method, axial flow method, pipe method and heat flow meter measurements [64,65]. The transient techniques are applied during the process of heating or cooling of the materilas. This method is based on the measurement of thermal diffusivity as a function of time, by recording temperature during the time that a transient or periodic heat is exposed to the sample surface. Thermal conductivity can be calculated through the equation 3, as is described below:

$$k = \alpha C_p \rho \qquad \textbf{Equation 3}$$

Where k is the thermal conductivity, α is the thermal diffusivity, ρ is the density and C_p is the specific heat. These methods are much faster compared to the steady-state methods, but with lower accuracy and more data analysis. Some of these techniques are including flash method, transient hot wire and transient plane source methods [66–68].

1.3.3. Thermally-conductive coating applications

Nowadys, the conductive materials are attracting a high attention, due to the increasing of cooling demand in emerging industries. Conductive polymeric materials has some advantages compared to the other thermally conductive materials, including metals, ceramics and carbon materials. Some of these benefits of polymers are listed below:

- light weight
- corrosion resistance
- simple processability
- good miscibility with the conductive fillers
- good compliance with the adjacent rough surfaces

Some emerging applications of thermally conductive polymer composites are LED devices [69,70], solar cells [71], electronic assembly [56] and batteries [72].

Here, the main goals of this thesis and the approaches to acheive them are summarized in Figure 7. Mostly, it’s focused on using the sustainable process, materials and simple methods to fabricate the functional coatings for different applications such as non-wetting surfaces with various extra properties such as biocompatibility, anti-bacterails adhesion and thermal storage properties. Also working on thermally conductive coatings for lightening strike protection and water vapor

condensation study. The comprehensive characterization of these coatings materials and properties are shown in this doctoral thesis with focusing on some laboratory applications of the abovementioned coatings, which can be tuned to industrial applications in the future.

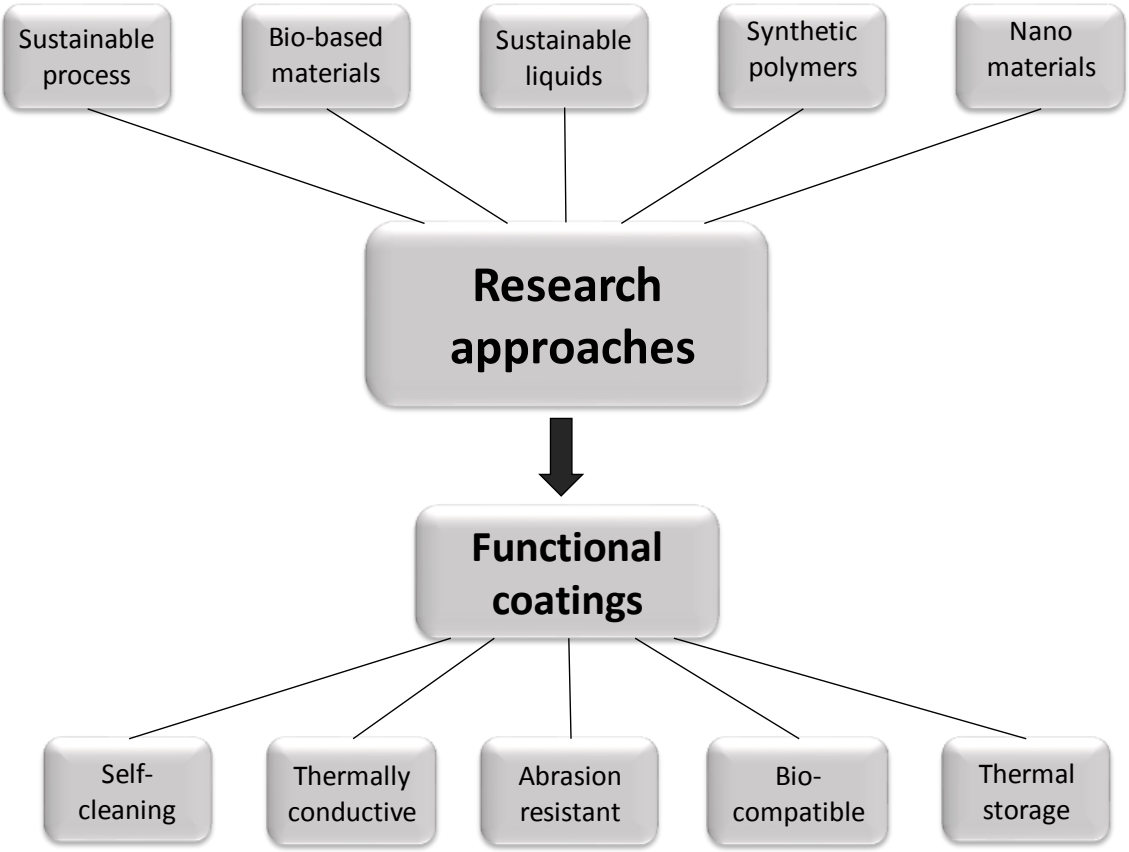

Figure 7. The schematic of these research works.

Chapter 2

Interfacing superhydrophobic silica nanoparticle films with graphene and thermoplastic polyurethane for wear/abrasion resistance

2.1. Introduction

Nanoparticles like silica ones have been widely used in the fabrication of superhydrophobic coatings, due to their abundance and low cost [73]. They can be deposited on the surfaces by various industry-friendly techniques such as dip coating or spray painting on large areas [74,75]. Mechanical stability or coating durability of these nanoparticle films is essential for the target applications [76]. One of the most important issues attributed to the stability of these nanoparticle films is their ability to attach or adhere to the underneath surface, while it is not easy to permanently bond the nanoparticle films onto the metallic or ceramic surfaces [77,78]. One option could be thermal embedding to weld or attach the nanoparticle films on surfaces. However, this technique needs generally high temperatures (>600˚C) for embedding of ceramic or metallic nanoparticles into the substrates like glass [77], but recently it was performed at lower temperatures [78]. Another method is to use a thin thermoplastic polymer layer as a primer on substrates to act as an embedding matrix for nanoparticle films at much lower temperatures [79–82]. In this work, we focus on this approach, to study the durability and wear abrasion resistance of silica nanoparticle films on aluminium substrates covered with a thin thermoplastic polyurethane (TPU).

TPUs are one of the most fastest growing polymers [83,84], which are well-known for their prominent versatility co-polymer chemistry structures that can be transfered from soft rubbery elastomer to soft-hard hybrid materials and even rigid plastics, so they can have various range of toughness, elongation, thermal properties and abrasion resistance [85,86]. TPUs has high flexibilty at low temperatures [87], good abrasion resistance [88], and good biocompatibilty [89]. The presence of rubbery matrix in the coatings structure can be useful for improving the abrasion resistance of non-wetting coatings [90]. Since TPU has both soft and hard segments in the structure, the soft segment can act as rubbery mechanical energy dampening sites [91].

In this study, we indicate that spray-deposited nanoparticle films from commercial fumed silica nanoparticles modified with organosilane, can be wear abrasion resistant by thermally embedding into TPU matrix. Further, we demonstrate that the presence of thermal interface graphene nanoplatelets between nanoparticle film and TPU thin layer can be helpful to improve the wear abrasion resistance of the final coating, while maintaining the non-wetting state.

2.2. Materials and Methods

2.2.1. Materials

The hydrophobic fumed silica nanoparticles (silica NPs), Aerosil R-812, with an average particle size (7–40 nm) were kindly donated by Evonik Industries, Germany. Polyether-based thermoplastic polyurethane (TPU), Elastollan 1185A granules with density 1.12 g/cm^3 and melting temperature of about 92˚C was purchased from BASF, Germany. Graphene nanoplatelets (GnPs, with commercial name Pure G$^+$), with thickness: 8 nm, lateral size: 600 nm and number of layers: > 8 [92] were kindly donated by Directa Plus, S.p.A. Italy. Commercial aluminum (Al) foils (2 cm × 2 cm, thickness: 1 mm) were used as substrates. Reagent grade chloroform, acetone, isopropanol and cyclopentanone were purchased from Sigma-Aldrich and used as received.

2.2.2. Preparation of coatings

All samples were fabricated by spray coating method from various organic solvents. for the polymer solution, TPU pellets were dissolved in chloroform to make a 2 wt% solution. Silica NPs and GnPs were dispersed in chloroform, separately, to form 2 wt% and 1 wt% dispersions, respectively. The polymer solution and nanomaterials dipsersions were ultrasonic processed for 1 min duration with probe sonic processing (SONICS, Vibra cell, USA) followed by 2 h in an ultrasonic bath at 59 Hz (SAVATEC, Strumenti scientifici, LCD Series, Italy). The solutions were spray deposited onto the Al foils by using an internal mix airbrush spray system (model VL-SET, Paasche), with 200 kPa pressure. The spraying process was done at 15 cm distance between the nozzle and substrate. Some coatings were thermally annealed at 150˚C for 10 min on a hotplate after half an hour solvent evaporation in room temperature. Different sample formulations are summarized in Table 1, to obtain the more robust and wear resistant coating.

Table 1. Various nanoparticle films, which fabricated in this work.

Sample code	Primer	Interlayer	Nanoparticle film	Annealing Temperature (˚C)	Annealing time (min)
S1	TPU	-	-	-	-
S2	TPU	-	-	150	10
S3	TPU	-	Silica NPs	-	-
S4	TPU	-	Silica NPs	150	10
S5	TPU	GnPs	Silica NPs	-	-
S6	TPU	GnPs	Silica NPs	150	10

2.2.3. Wetting Properties

Water CAs and RAs were measured by sing (Data physics, Germany) contact angle goniometer. Five different areas from different coatings were selected for these measurements in an identical conditions. For each measurements, 8 µL water droplets were dispensed onto the coating's surface and CA values were measured. In order to measure the RAs, 8 µL water droplets were dispensed on the surface followed by continuous stage tilting with angular velocity of 1.42˚/sec. The tilting angles which all the droplets can roll away on the coatings were recorded as RAs.

2.2.4. Morphological study of the coatings

The surface morphology of the fabricated coatings was analyzed by JSM-6490AL scanning electron microscope, SEM (JEOL, Japan) using 10 kV acceleration voltage. The coatings were sputter-coated by a thin layer of gold (15 nm) before experiments. To obtain cross-section SEM images, the coatings were cryogenically fractured in liquid nitrogen, followed by coating the fractures by a thin layer of gold (15 nm) again. To identify the elemental distribution of the coatings, Energy dispersive X-ray (EDX or EDS) analysis were performed at 10 mm working distance and 10 kV acceleration voltage by doing 15 sweep counts per each samples.

Topographical analysis were studied by using a NanoWizard III AFM system (JPK Instruments, Berlin). The AFM force-distance curves (256 × 256) were obtained in Quantitative Imaging (QI) mode. To select the areas for the analysis, an Axio Observer D1 inverted optical microscope (Carl Zeiss, Germany), coupled with the AFM system was used. Areas of 10 × 10 μm^2 were scanned by using single-beam PPP-NCHR cantilevers (Nanosensors, USA) with a spring constant of about 42 mN m^{-1} with a nominal tip diameter <10 nm. The experiments were done in air in a vibration-insulated environment at ambient temperature. The relative set point was adjusted to 500 nN. Watershed algorithm was used to examine the roughness characteristics of the coating's surface. AFM topography images are segmented into various zones with a special average roughness value. The total mean roughness of the area is calculated by making average from the values of different areas [93].

2.2.5. Fourier Transform Infrared spectra (FTIR) analysis

Chemical stuctures of the coatings before and after thermal annealing were studied by using an ATR accessory (MIRacle ATR, PIKE Technologies) coupled with FTIR spectrophotometer (Equinox 70 FTIR, Bruker). All measurements were performed in the range from 4000 to 600 cm^{-1} resolution by doing 64 scans per each samples. To confirm the reproducibility of the results, the experiments were done on three samples of each coatings.

2.2.6. UV-Visible spectroscopy

Cary spectrophotometer 6000i was used to identify the transparency of silica dispersions in different solvents. The experiments were performed by using UV-VIS-NIR light source in the range from 300 to 800 nm at room temperature.

2.2.7. Thermal analysis

Differential scanning calorimetry (DSC) was used to obtain the melting temperature of TPU pellets by using a Diamond DSC-Perkin Elmer instrument. Almost 18 mg of TPU pellets was encapsulated in an Al pan in order to heat from -50˚C to 210˚C by a heating rate of 20˚C/min followed by maintaining at this temperature for 1 min. Then the sample was cooled down to -50˚C and heated to 210˚C with the same rate, again. The measurement was done under nitrogen atmosphere at a flow rate of 20 ml/min.

In order to complete the analysis, other thermal properties were evaluated by using thermogravimetric analysis (TGA), TGA Q500 (TA Instruments, USA). The experiments was done on 15-20 mg of TPU pellets under nitrogen atmosphere in Al pans. The sample were heated from 25˚C to 800˚C with the heating rate of 10˚C/min.

2.2.8. X-ray disffraction analysis

X-ray diffraction technique was used to study the crystallinity structure of TPU, before and after of thermal annealing with PANalytical Empyrean X-ray Diffractometer. The measurements was performed by using Cu radiation with $\lambda = 0.1541874$ nm at 45 kV and 40 mA. Scans were done at diffraction angle from $2\theta = 10^{\circ}$ to $2\theta = 45^{\circ}$.

2.2.9. Wear abrasion resistancy

A linear abrader (Taber® Linear abrader/Abraser, Model 5750) was used to analyze the robustness of the coatings under a constant load of 20 kPa applied pressure. In general, this pressure is higher than some pressures reported in the literature (equal or less than 10 kPa) [94–97], with constant stroke speed at 15 cycles/min. During these tests, CAs and RAs were measured after each linear abrasion cycles. A disk-shaped material (1.27 cm in diameter) known as CS-10F Calibrase was used as an abradant to produce mild abrading action under light loads with stroke distance of 10 cm (See Figure 8).

Figure 8. The schematic illustration of Taber abrader.

2.3. Results and Discussion

2.3.1. Silica NPs and TPU coatings

First, we discovered the morphology of the spray-coated silica NPs film on Al substrate from different organic solvents, to investigate the best film formation ability from the most stable and agglomerate-free nanoparticle dispersions. As the nanoparticle's surface were chemically modified with the hydrophobic materials, they could just disperse in organic solvents. we selected some organic solvents such as chloroform, acetone, isopropanol and cyclopentanone, which the last three are environmentally- friendly solvents [98].

Transparency of silica dispersions in different solvents was studied by UV-Vis spectroscopy and the results are shown in Figure 9, a. It can be seen that relative absorbance of the chloroform dispersion is insignificant respected to the others. This observation also can be confirmed in Figure 9, b, which shows the photograph of the silica dispersions in various organic solvents. It's obvious that the silica dispersion in chloroform is the most transparent ones, followed by cyclopentanone. However, for cyclopentanone the dispersion shows slight yellowing during the time. The relative absorbance for the silica dispersions in acetone and isopropanol is higher, which can be a witness for the milky and hazy color of the dispersions.

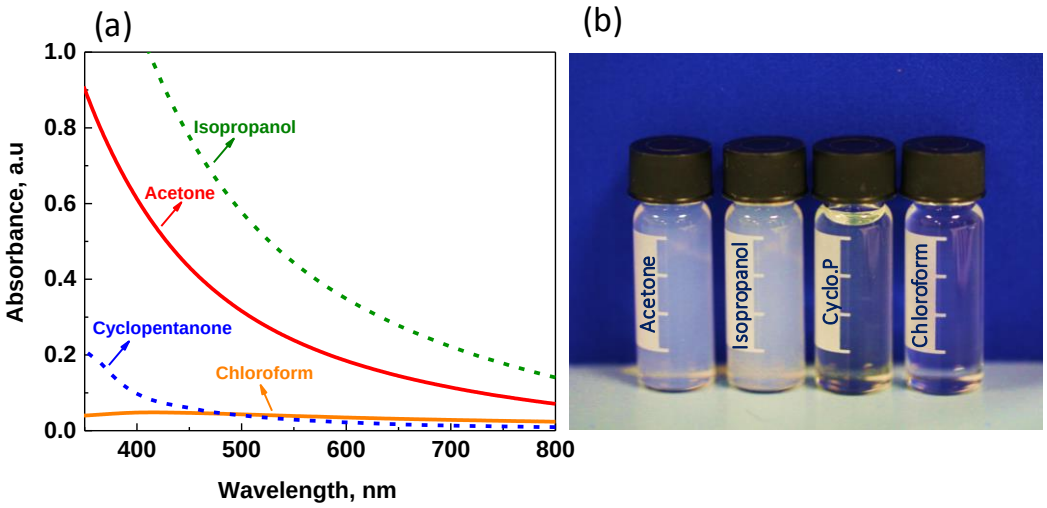

Figure 9. (a) Transparency of silica dispersions by UV-Vis spectroscopy. (b) The photograph of silica dispersions.

Dynamic light scattering (DLS) analysis was used to investigate the average size distributins in silica dispersions and the results are shown in Figure 10. The graph showed the average size distribution for colloidal silica agglomerate is around 192.33 ± 0.55 nm for chloroform dispersion, which is the lowest among others, which can also confirm the most transparency of the silica dispersion in chloroform. However, the amount of agglomeration is higher for isopropanol and acetone dispersions and is about 960.6 ± 14.41 nm and 483.93 ± 3.7 nm, which shows a broader distributions that related to hazy state of these dispersions. Also, for cyclopentanone dispersion, this value is around 323.3 ± 2.19 nm and this caused the hazing effect in this dispersion.

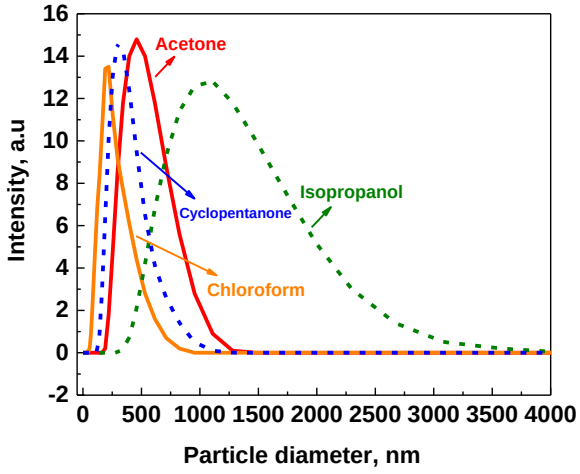

Figure 10. Dynamic light scattering results for silica dispersions in different organic solvents.

The main problem of the nanoparticle film was that they removed from the surface with fine touching or rubbing on the surface, as they had no adhesion onto the substrate. The nanoparticle surface was functionalized with bis(triethylsilyl)amine known as hexamethyldisilazane or HMDS,

$HN[Si(CH3)_3]_2$, which makes it hydrophobic. Thermal annealing at different temperatures were performed to investigate if the hydrophobic HMDS groups can be bonded into the Al substrate by means of heat. So the nanoparticle films (regardless of the solvent that used) were annealed on hotplate with different temperatures up to 300˚C, but no binding effect was observed. Furthermore, the nanoparticle films lost their hydrophobicity after 220˚C, which couls be related to the degradation of HMDS moieties [99]. Hence, we studied the interfacing the nanoparticle films by using TPU and graphene layers.

For this reason, we analyzed the film formation property of TPU polymer from chloroform solution, which is spray coated onto the Al substrate. The cross section SEM image of a substrate coated with TPU layer is shown in Figure 11, a and the EDX analysis is indicated in inset (Al in blue, C atoms in red). The coating was dried under ambient temperature. It can be seen that TPU displays a good conformal surface coverage and affinity toward Al substrate. However, sudden solvent evaporation during spraying, forms a rather rough surface, which can be alleviated by thermal annealing treatment. Figure 11, b shows the cross section SEM image of the TPU coating after thermal annealing at 150˚C for 5 min. The SEM image indicates that the surface becomes very smooth along with complete coverage of the substrate surface [100].

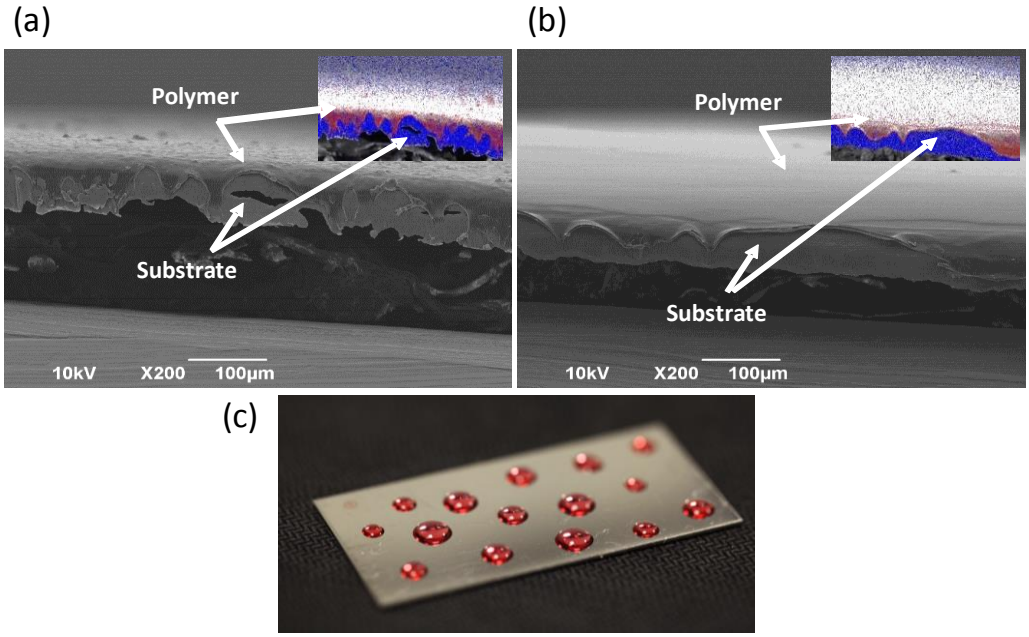

Figure 11. Cross section SEM image of TPU primer (a) before and (b) after thermal annealing. (the insets in (a) and (b) is related to the EDX analysis). (c) the photograph of colored water droplets onto TPU layer [75].

To study the effects of thermal annealing on chemical structure and crystallinity of the polymer, FTIR and XRD analysis were done before and after thermal annealing and the results are shown in Figure 12. FTIR data showed some small differences in peak intensities, before and after thermal annealing.

The intensities of N-H stretching mode (3324 cm^{-1}) and ester C=O stretching mode (1730 cm^{-1}), attributed to urethane linkages [101], increased after thermal annealing, which could be related to some potential rearrangements of the polymer structure, rather than formation of new chemical bonds [102]. However, XRD analysis show no significant differences by performing thermal annealing, as the crystallinity was the same for both samples before and after thermal annealing.

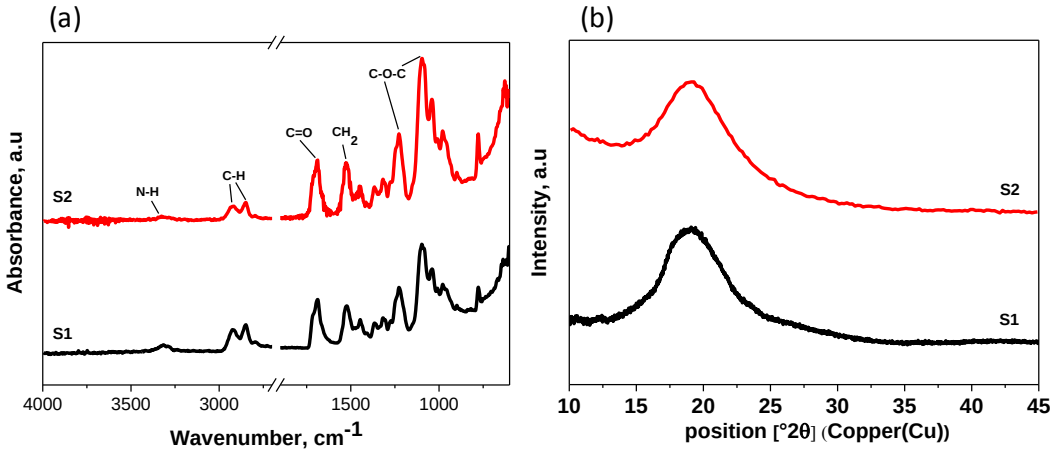

Figure 12. FTIR spectra for TPU primer before and after thermal annealing. (b) XRD pattern for TPU polymer before and after thermal annealing.

To have a comprehensive study about silica dispersions, all the dispersions were spray coated onto the Al substrate coated with pre-annealed TPU primer, in order to measure the wetting properties and also studying the morphology of the surface (See Figure 13). The wetting analysis showed superhydrophobic behaviour for nanoparticle films prepared from silica dispersions in acetone, isopropanol and chloroform with very low CAH, whereas the film fabricated from cyclopentanone dispersion was slightly less hydrophobic. SEM images show that all the films except from that one which produced from chloroform dispersion has many surface cracks, which is not good for TPU surface coverage. According to the wetting analysis, the nanoparticle film obtained from chloroform dispersion was the most water repellent ones, so for these reasons we have selected the silica dispersion in chloroform for furthur study and also to improve the durability.

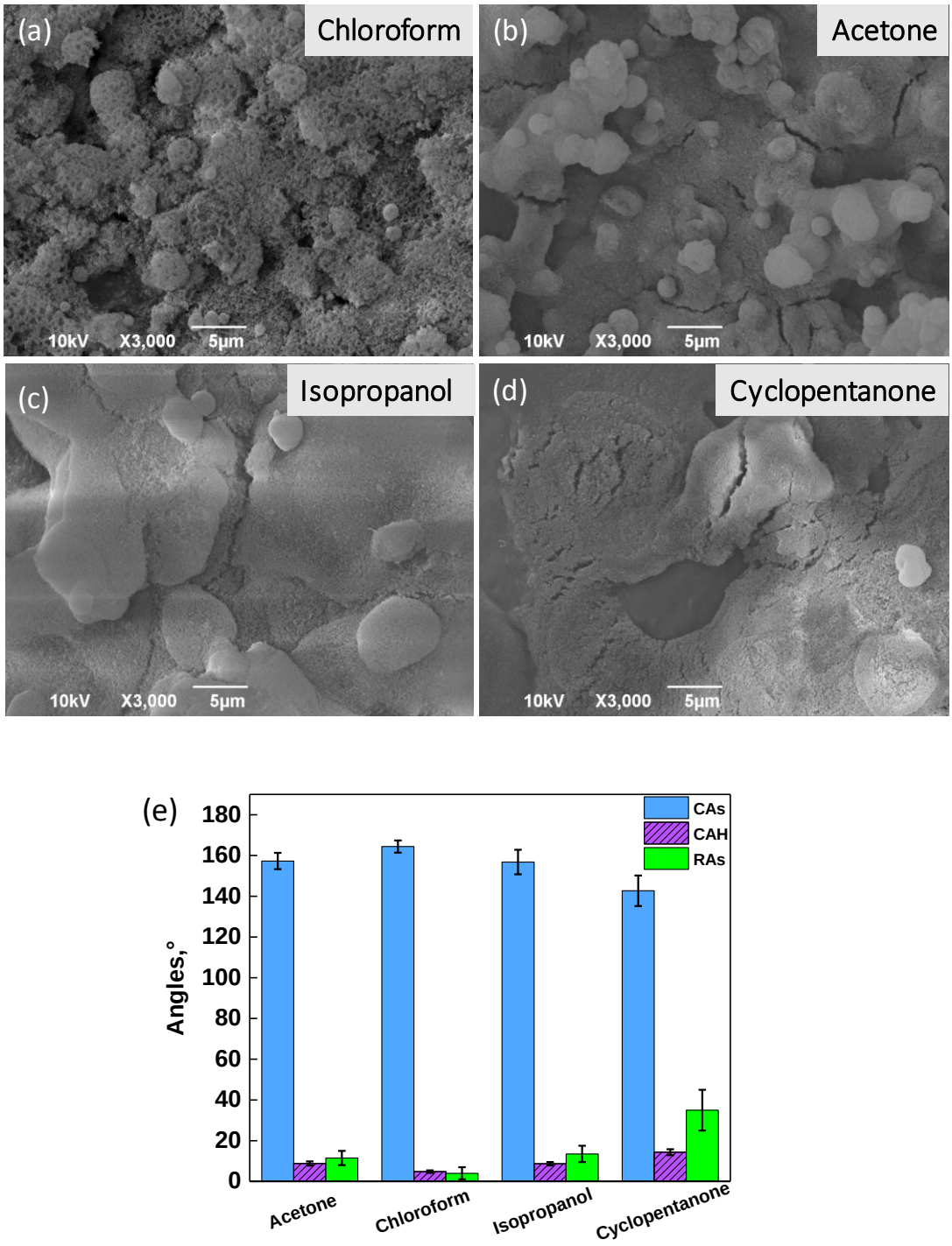

Figure 13. SEM images of the silica NPs film obtained from (a) chloroform, (b) acetone, (c) isopropanol and (d) cyclopentanone dispersions. (e) Comparison of static CAs, RAs and CAH of these coatings.

2.3.2. Impact of annealing temperature and silica NPs concentration

As the final goal of this work is to fabricate a wear abrasion-resistant nanoparticle film, the nanoparticles need to be embeddedinto the TPU primer layer. Annealing the nanoprticle films was performed in order to allow the fusion of part of the nanoparticles into the polymer matrix. This treatment has been implemented for other polymer coatings as well [103,104]. A systematic study

was conducted to understand the effects of silica NPs solution concentration and annealing temperature on the final properties of the coating such as hydrophobicity and surface morphology. Three different concentration of silica NPs dispersion in chloroform were selected to spray coat onto TPU primer, namely as 0.5, 1 and 2 wt%. Surface morphology of each coating were investigated by using SEM and the images are shown in Figure 14, a-c. After spray deposition of silica NPs onto TPU primer, the coatings were thermally annealed on hotplate with different temperatures and wetting properties were analyzed (See Figure 14, d). The coating obtained from 2 wt% silica NPs dispersion (sample S3) made full polymer surface coverage upon a single spray pass, however other samples need multiple spray passes to ensure full coverage over TPU primer layer, which is related to the lower concentration compared to 2 wt%.

This observations can be confirmed by analyzing the wetting properties of these coatings. It can be seen that the superhydrophobicity threshold can be acquired by spraying 1 wt% dispersion followed by annealing at 100˚C or 150˚C. While, annealing at 200˚C, even for the coating obtained from 2 wt% solution, could not provide the superhydrophobic property, but rather produced wetting states known as sticky hydrophobicity [105–108].

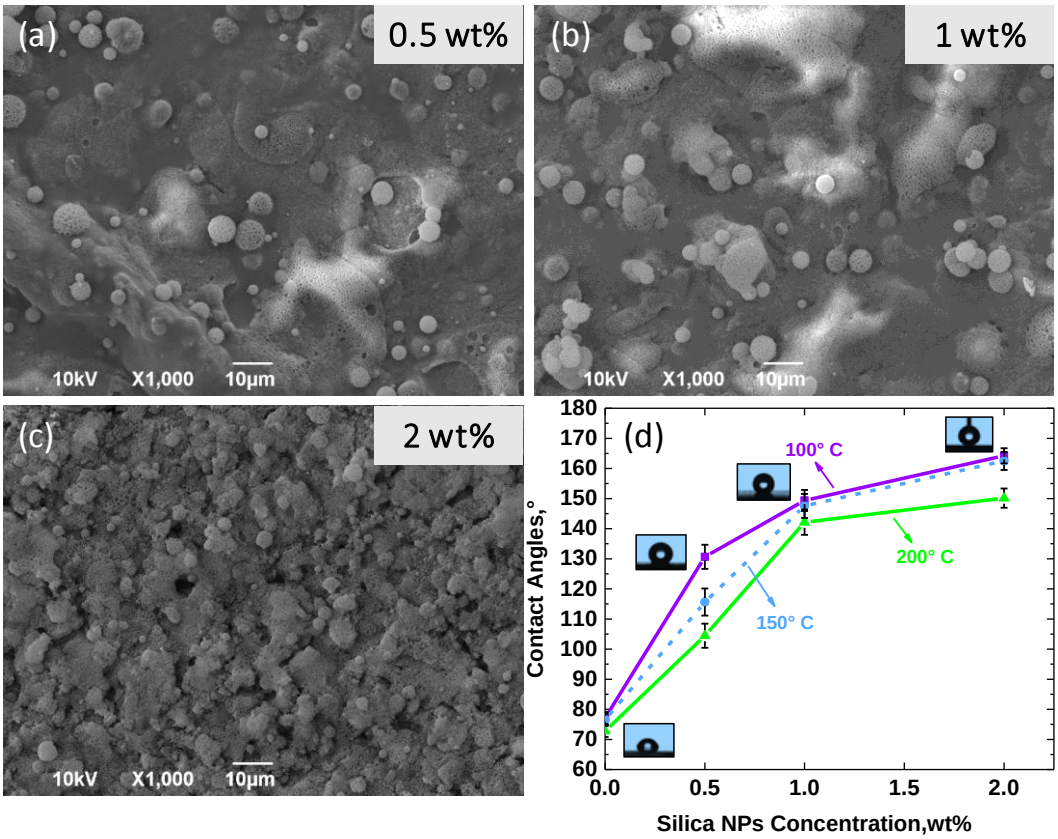

Figure 14. SEM images of the nanoparticle films obtained from (a) 0.5 wt%, (b) 1 wt% and (c) 2 wt% silica NPs dispersion in chloroform. (d) Static CAs of these coatings upon thermal annealing at 100˚C, 150˚C and 200˚C.

This phenomena could be attributed to the partially degradation of HMDS moieties on silica NPs surface rather than degradation of TPU primer layer, according to the DSC and TGA analysis of TPU (See Figure 15). Moreover, migration of low molecular weight TPU chains into the nanoparticle film at 200˚C, would be another reason for losing superhydrophobicity in this temperature [101]. Analyzing the data from DSC indicates that melting point of TPU pellets was around 92˚C, however TGA analysis shows no significant weight loss before 280˚C. So the optimal conditions for the fabrication of self-cleaning superhydrophobic coating was obtained by spray deposition of 2 wt% dispersion and thermal annealing at 150˚C for 10 min.

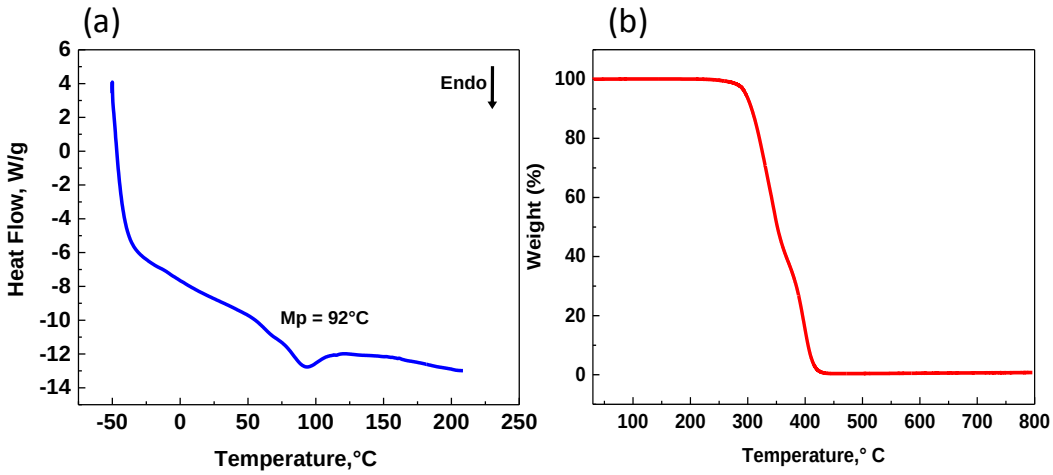

Figure 15. (a) DSC pattern for TPU pellets. (b) TGA analysis for TPU pellets.

2.3.4. Effect of GnPs interface

Since thermal anneling treatment was limited by simultaneous degradation of HMDS functional groups of silica NPs and migration of melted TPU with lower molecular weight into the nanoparticle film, we were thinking use of a thermal interlayer material between TPU primer layer and nanoparticle film, could be considered as the next step. In order to investigate this purpose, a very thin layer of GnPs was spray coated onto the TPU primer, followed by spraying silica NPs film. Due to the hydrophobic nature of GnPs, this material can compensate the hydrophilicity of TPU underlying layer, moreover it can also acta s a physical barrier to prevent migration of TPU chains into the nanoparticle film surface at higher temperature [35,109]. Furthurmore, due to the excellent thermal conductivity of GnPs, this material could display a very efficient heat transfer behaviour

during thermal annealing process, allowing more polymer chains movements followed by impregnation of silica NPs into the polymer matrix along with graphene flakes [110]. This concept is clearly displayed in Figure 16, especially in EDX images, where Si, C and Al signals are shown in cross section state. By thermal annealing of the nanaoparticles film deposited on TPU primer layer (sample S4) at 150˚C, only slightly impregnation or embedding of silica NPs into TPU layer can be observed, Figure 16, b. By applying the graphene interlayer over TPU primer, after thermal annealing, more quantities of silica NPs were embedded into polymer matrix over the GnPs flakes. The amount of the graphene which used as interface is negligible and it is around 1 wt% of the TPU polymer.

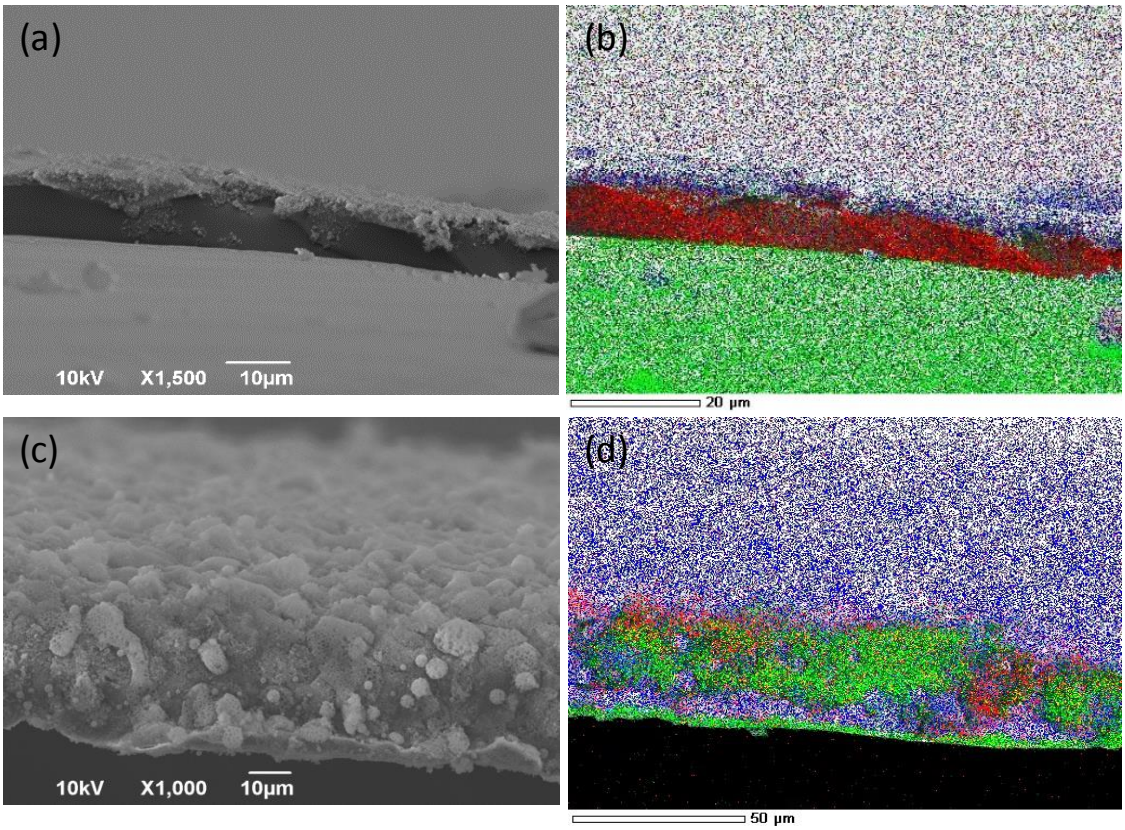

Figure 16. Cross section SEM images of (a) S4 and (c) S6 samples. Cross section EDX images of (b) S4 and (d) S6 samples. In EDX images, the atoms are indicated as Al in green, C in red and Si in blue [75].

The effects of graphene interface on the surface topography of the coatings was also investigated by atomic force microscopy (AFM) measurements and the results are shown in Figure 17. Sample S2 was selected as a control sample and average surface roughness values for the coatings S2 (TPU primer), S4 (without graphene interlayer) and S6 (with graphene) were calculated from several AFM measurements. These analysis were conducted using a built-in grain statistical algorithm known as watershed algorithm. It is usually employed for local minima/maxima determination and image

segmentation in image processing. The AFM topography images are divided into different zones identified with a certain average roughness. The overall average roughness of the image is obtained by averaging the roughness values from different areas [93]. Sample S2 shows a very smooth and uniform surface, without any significant features on it, with average roughness value around 1.43 ± 1 nm. S4 sample shows an average surface roughness value around 445 ± 120 nm, which is acquired by micro structured agglomerates of silica NPs. However, for the S6 sample, this value decreased to 390 ± 55 nm, which could be attributed to the fact that in the presence of GnPs interlayer, much more silica NPs are impregnated into TPU primer layer, which causes the smoothing of the micro-scale features.

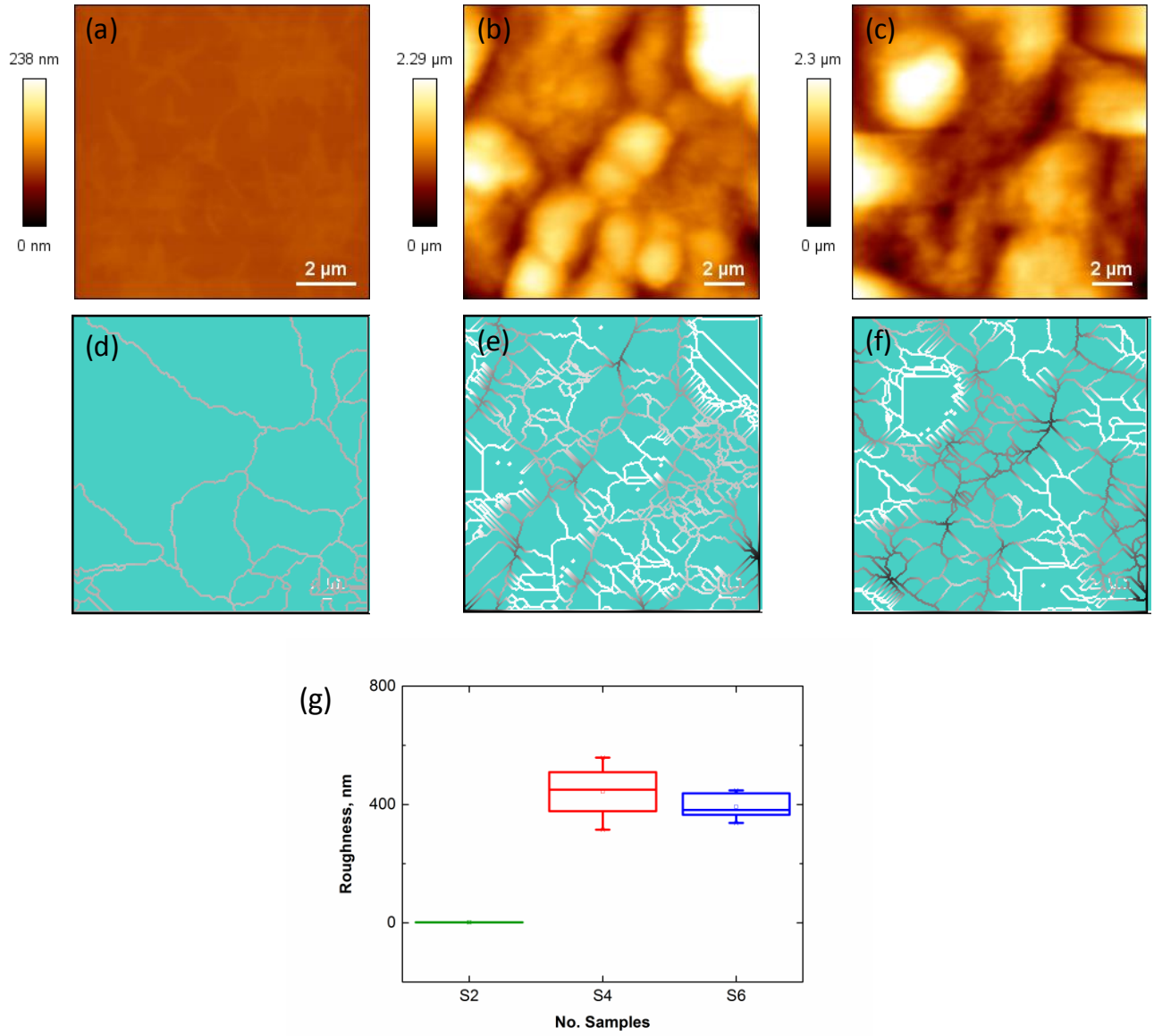

Figure 17. AFM topography of (a) S2, (b) S4 and (c) S6. Watershed grain analysis of (d) S2, (e) S4 and (f) S6. (images divided to different zones, according to the average roughness values. (g) Comparison of average roughness values for S2, S4 and S6.

2.3.5. Wetting analysis

The wetting properties of the selected samples were analyzed by measuring the static water CAs and RAs and the results are shown in Figure 18. TPU primer layer shows a hydrophilic behaviour with CAs around 70˚ and the water droplets couldn't display any rolling effect, which means the surface shows stick-slip behaviour when the surface was tilted to 90˚ and the water droplets couldn't roll-way on the surface. This property has been observed for both TPU primer samples, before and after thermal annealing. Hence, RAs indicated as 90˚ for S1 and S2 samples [111].

The rest of the samples, S3 to S6, superhydrophobic property was observed, with RAs less or close to 10˚. By comparison the samples S3 with S4 and S5 with S6, it can be seen that after thermall annealing the CAs decreased and RAs increased slightly, which could be related to the aforementioned smoothing effect during thermal annealing. Comparing the sample S5 with S6, shows this behaviour due to the presence of inetrfacial graphene layer that makes better heat transfer.

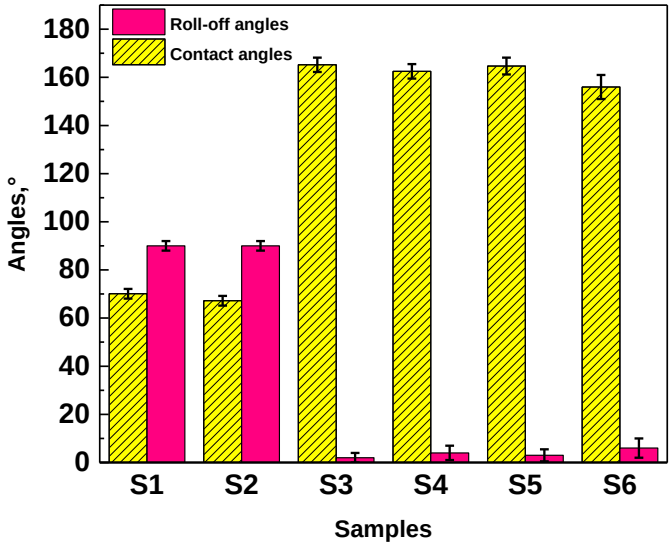

Figure 18. Static water CAs and RAs of all the samples.

It's worth noting that although the coatings were applied on the hard substrate like Al substrates, but the nanoparticle films can be applied on any types of substrates such as fabrics, as long as the fabric does not degrade during the thermal annealing process (See Figure 19).

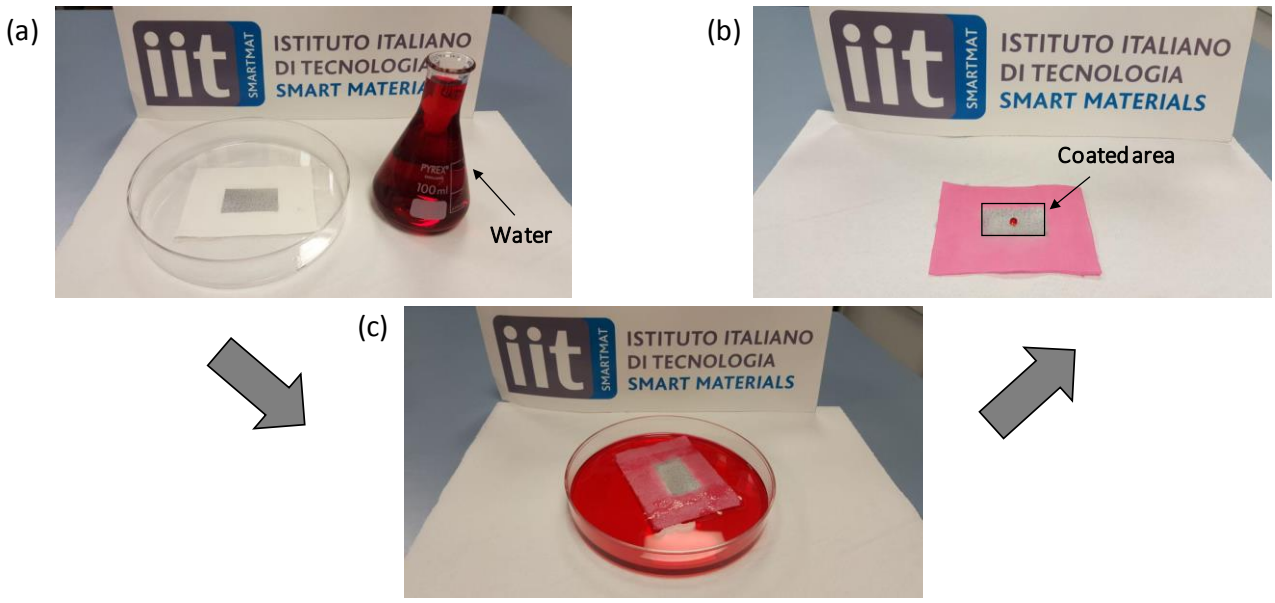

Figure 19. A schematic of applying the superhydrophobic coating on soft substrate like textile.

2.3.6. Abrasion test results

The last experiment was done to examine the abrasion resistancy of the coatings and the results are displayed in Figure 20. The wetting properties (static water CAs and RAs) of the samples were measured after each abrasion cycle and the experiments were terminated as the droplets show the stick-slip behaviour on the surface with increasing of RAs more than 10˚.

Samples S1 and S2 were chosen as the control samples to see the abrasion resistancy of TPU primer layer. As it can be seen in Figure 20, a TPU shows a very good abrasion resistancy even after 30 abrasion cycles, however due to the hydrophilicity of TPU, the RAs for these two samples are not shown, as the surface displayed stick-slip behaviour. Sample S3, the nanoparticles film without graphene and without thermal annealing, indicates also reasonably good abrasion resistance up to 15 abrasion cycles under 15 kPa. However, after this cycle the nanoparticles film starts to wear and the rest of the film lost its superhydrophobicity and water RAs increased more than 10˚. For the other samples, S4, S5 and S6 better abrasion resistance were recorded, especially for the sample S6, the water RAs remained less than 10˚, even after 30 abrasion cycles and this sample displayed the best abrasion resistancy among others, as it can be seen in Figure 20, d. For the samples S4 and S5, the RAs starts to exceed more than 10˚ after 25 abrasion cycles and the coatings lost their self-cleaning superhydrophobicity property and failed [90,110]. These results can confirm the effects of graphene interfacial layer, which caused the better inclusion of silica NPs into the polymer matrix and improve the abrasion resistance. These effect is more obvious under electron microscope Figure 20, b-f. SEM image of S4 sample, Figure 20, b shows that some parts of the coating removed after some abrasion cycles, as this can be seen in EDX analysis of this sample in Figure 20, c, where the Al substrate is

out in some parts, so this sample loses its superhydrophobicity. However, for the sample S6, due to the presence of graphene interlayer and better embedding of silica NPs into TPU primer, only wear marks are apparent on the surface after 30 abrasion cycles. This observation can be seen in EDX image of this sample in Figure 20, f, which the distribution of silica NPs can be seen everywhere in the coating and the surface are still intact and maintain a degree of roughness [110].

The thermal conductivity of polymers in general is low and for TPU is around 0.2 W/mK. This value is low also for silica NPs and is about 1.3 W/mK [111]. However, this parameter is really high for pure graphene and is around 4000 W/mK, although, the GnPs which used in this work are multi-layered and thermal conductivity is a lower around 1000 W/mK [112]. As it was mentioned, due to the low thermal conductivity of TPU primer and silica NPs film, there is not an efficient heat transfer between these two layer. So using a maerial like GnPs with high thermal conductivity between these two layers could improve the heat conduction in the final system, which caused more embedding of silica NPs into polymer matrix. Furthermore, a recent work showed that graphene tends to have strong affinity towards adhesion and also to silica NPs [113,114].

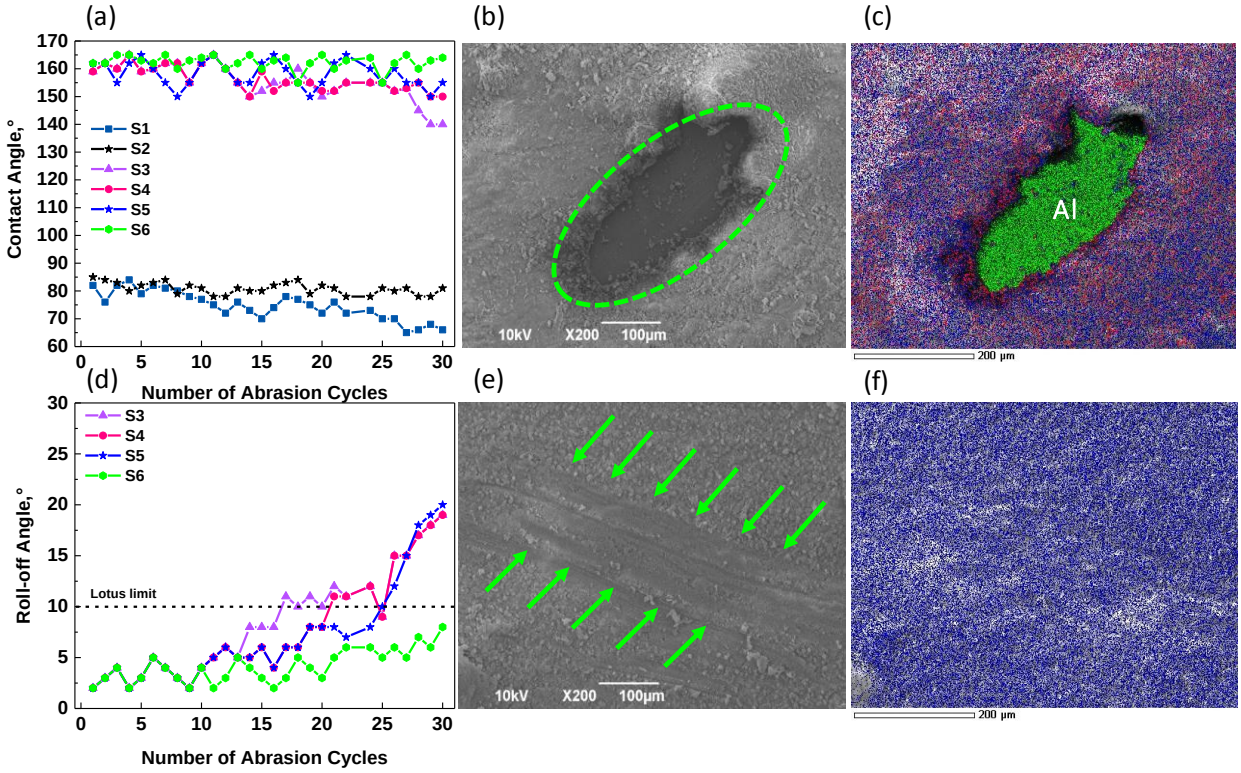

Figure 20. Abrasion effects of different coatings upon 30 abrasion cycles on (a) static water CAs and (d) RAs. SEM images of (b) S4 and (e) S6 after 30 abrasion cycles. EDX analysis images of (c) S4 and (f) S6 after 30 abrasion cycles.

Table 2 shows the results from recent literature works about mechanical stability of liquid-repellent nanoparticle films. Comparing the results in this table, indicates the presence of different types of tests to examine the durability of the superhydrophobic coatings, such as tape peel, liquid shear, pencil hardness, AFM tip scratch and manual sandpaper application. The table also displays that a huge number of these studies report the weight, pressure and the number of cycles applied up to the point that the films lost their superhydrophobicity property. The results of this work shows a rather significant wear abrasion resistance compared to the other works, according to the simple fabrication procedure and the industrially availability of the used materials. It's worth noting that a meaningful abrasion distance could be considered as a distance experienced by each point on the abraded superhydrophobic surface, which is the product of the number of abrasion strokes and the length of abradant head (not the sroke length) [115]. According to the abrading attachment mounted on the tip of the strock shaft is 1.27 cm in diameter, which is related to the length of the abradant. The numbers of the strock was 30, so the distance which is exprienced by each point in the abraded surface is around 38.1 cm [115]. Most of these results in this table are based on the multiplication of strock distance with the number of abrasion cycles, which is calculated in our work around 300 cm, which is higher respected to the other works.

Table 2. Comparison of mechanical durability of various water-repellent nanoparticle films [75].

Nanoparticle Film	Substrate	Nanoparticle Surface Functionalization	Durability Test	Applied Weight/ Pressure / Force	Number of abrasion/ Distance	Ref
ZnO	Epoxy resin	ODP*	AFM scratch	10 µN	1	[116]
SiO_2 ; ZnO; ITO	Glass/ PC/ PMMA	Silane- ODP*	AFM scratch	10 µN	1	[43]
SiO_2	Glass	Fluoropolymer	Shear	100 g	n/a	[52]
SiO_2	Glass	Perfluorosilane	Sand paper	50 g	10	[117]
SiO_2	Steel	Organoslinae	Sand paper	50 g	20	[118]
SiO_2	Epoxy-coated glass	DDS*	Tape peel	100 g	7	[119]
SiO_2	Wood	VTES*	Sand paper	3 kPa	105 cm	[120]
SiO_2	PU/PMMA IPN-coated substrates (various)	Perfluorosilane	Taber abrader	250 g	300	[121]

TiO_2 ; SiO_2	Pigment-coated paper	n/a	Taber abrader	250 g	10	[122]
TiO_2	Adhesive-coated substrates (various)	Perfluorosilane	Sand paper	100 g	40 (10 cm)	[123]
$CaCO_3$	Adhesive-coated substrates (various)	Perfluorosilane	Sand paper	100 g	30	[124]
SiO_2	PC	n/a	Pencil hardness Scratch	10^7 µN	n/a	[125]
SiO_2	PET	Methyl phenyl silicone resin/ Perfluorosilane	AFM/ tribometer scratch	10 µN	1	[126]
SiO_2	TPU-coated Aluminium	Organosilane	Taber abrader	20 kPa	30 (≈ 300 cm)	Current work

2.4. Conclusions

Despite the existence of several reports about the fabrication of superhydrophobic nanoparticle films, the abrasion resistance of these films are still challenging issues for large scale production. One of the most important problem is the adherence of these films to the underneath substrates, while a post treatment like thermal annealing or using a primer layer under the nanopartilce films can help to improve the adherence. In this work, a simple, cheap and scalable method is used to design and produce a non-wetting nanopartilce film based on silica NPs over the metal substrate, followed by a thermal annealing process. This approach was achieved by inclusion of silica NPs into a thermoplastic polyurethane primer layer by means of thermal annealing onto the metal surface. However, the embedding of nanoparticle films into the soft underneath primer layer was reported recently, this work does not need any extra chemical processing to embedd the nanoparticles into the primer layer. Moreover, the most stable silica NPs dispersion was obtained by dispersing the nanoparticles in different organic solvents and evaluating the transparency and stability before spraying. The crack-free silica NPs film was obtained from dispersion in chloroform, without requirement of any extra surfactant, which is essential to prepare the nanoparticle colloidal suspensions. Moreover, by spraying a thin interlayer of GnPs between the primer and nanoparticle film, we were able to improve the wear-abrasion resistancy significantly. This coating can be applied onto the different substrates to make a superhydrophobic nanoparticle film. Spray deposition method, cheap and commercially avaiable materials also can help to ensure the scale-up opprotunities.

Chapter 3

Superhydrophobic Coatings from Beeswax-in-water Emulsions with Latent Heat Storage Capability

3.1. Introduction

Natural or synthetic waxes have been proved very promissing in the fabrication of nonwetting surfaces, as they can be blended with other edible fatty acids and use in certain innovative techniques [32,127,128]. However, the main issues about using only wax materials is their thermal instability, leaching and poor mechanical property of this kinds of materials, due to the low melting point of waxes. For example, spray-coated films based on carnauba wax-alcohol emulsion creats hierarchical rough structures and shows superhydrophobicity effect. However, the wax starts to be melt under moderate heat exposure around 60˚C and the surface sructure become smoother under re-assembling of the wax particles, so the surface lose its superhydrophobicity. According to these drawbacks of wax materials, embedding of waxes into a suitable polymeric matrices could be a potential idea to eliminate or decrease this kinds of limitations [129]. The main hinders of impregnation of wax and fatty acids into the polymer matrices is the loss of hydrophobicity of wax, due to the migration of wax into the bulk of the polymer rather than assembling in the top surface to create hierarchical surface texture that causes the lotus effect [130]. Despite of these limitations, different waxes were embedded into the various polymer matrices to study the latent heat storage properties of these materials and they confirmed as effective agents for these capabilities [131–133]. In this section, we would like to obtain superhydrophobicity and latent heat storage capability from a functional coating. Here, a natural wax (beeswax) forms a half of the polymeric matrix instead of using as an additive. Beeswax is broadly utilized in different industries such as food, cosmetics, drug delivery and coatings [134–136]. To ensure the sustainability of the coatings fabrication process, we used water as the solvent in the whole project. To obtain a stable dispersion of beeswax in water or in other words to solubilize the beeswax inside water, we applied an oil-in-water emulsion system [137].

In many applications such as ink or paint formulations and drug delivery systems, wax emulsions in water are used which they are produced by using multiple surfactants or emulsifiers and stabilizers [138–142]. These additives are used to decrease the interfacial tension in the oil-water interfaces and to avoid the agglomeration and phase-separation [143,144]. Due to the phase change property of beeswax, it can absorb and release high amount of energy as heat in a small temperature gap, which makes it ideala s a latent heat storage material [145].

Here in this work, we used a commercial perfluorinated acrylic copolymer dispersion in water as it called “Capstone ST-100” or PFAC, to mix with hot beeswax/water solutions to fabricate a highly stable oil-in-water emulsion. In this formulation, PFAC acts as a nonionic fluorosurfactant, which is absorbed in the oil-water interfaces and eliminates the needs of additional dispersants for fabrication

of oil-in-water emulsion. Furthermore, the copolymer is encapsulating the beeswax by formaing a really thin shell around it, which can protect it from leaching. According to the Environmental Protection Agency (EPA) 2010/2015 perfluorooctanoic acid (PFOA) stwardship program, this waterborne acrylic copolymer dispersion does not breakdown into PFOAs in the environment and does not contain any C-8 fluorochemistry [146,147]. The copolymer not only acts as an encapsulation agent for beeswax and emulsion stabilizer, but also as an adhesion enhancer to improve the adhesion of the final coating to the substrate. Furthermore, hydrophilic modified silica NPs can easily be disperesed in these stable emulsion systems, to create the self-cleaning surfaces.

3.2. Experimental section

3.2.1. Materials

Chunks of beeswax was purchsed from Sigma-Aldrich and used as received. A commercial waterborne PFAC dispersion, PFAC was purchased from DuPont, USA. This dispersion contains 20 wt% cationic fluoroacrylic copolymer dispersed in water. Hydrophilic fumed silica NPs, Aerosil R-300 was kindly donated by Evonik Industries, Germany. Ultrapure Mili-Q water was used as solvent in the whole process.

3.2.2. Preparation of the coatings

Spray deposition method from water-based emulsions were used to fabricate all the coatings in this section. Firstly, beeswax was melted in boiling water and temporarily dispersed in water using probe sonic processing (Sonics, Vibra cell, USA) for 1 min to make a 1 wt% oil-in-water emulsion. This pre-emulsion was not stable enough and it starts to be phase-separated into a solid and oily was portion and water after a few minutes. To avoid the phase-separation, the commercial waterborne PFAC was added into the wax emulsion. To fabricate a 50:50 or 1:1 oil-in-water emulsion system, the commercial polymer solution was diluted with water to 1 wt% concentration before mixing with wax dispersion. Then the mixture around 300 ml was homogenized using a commercial tabletop laboratory homogenizer (Panda Plus 2000, GEA Niro Soavi, Italy). The homogenization step was performed at pressure about 275 bar with a flow rate of 9 L min^{-1}. The wax-polymer mixture was homogenized by passing through the homogenizer four times. To make nanocomposites, different amounts of silica NPs were dispersed in the oil-in-water emulsion system, followed by repetition of homogenization process (See Figure 21).

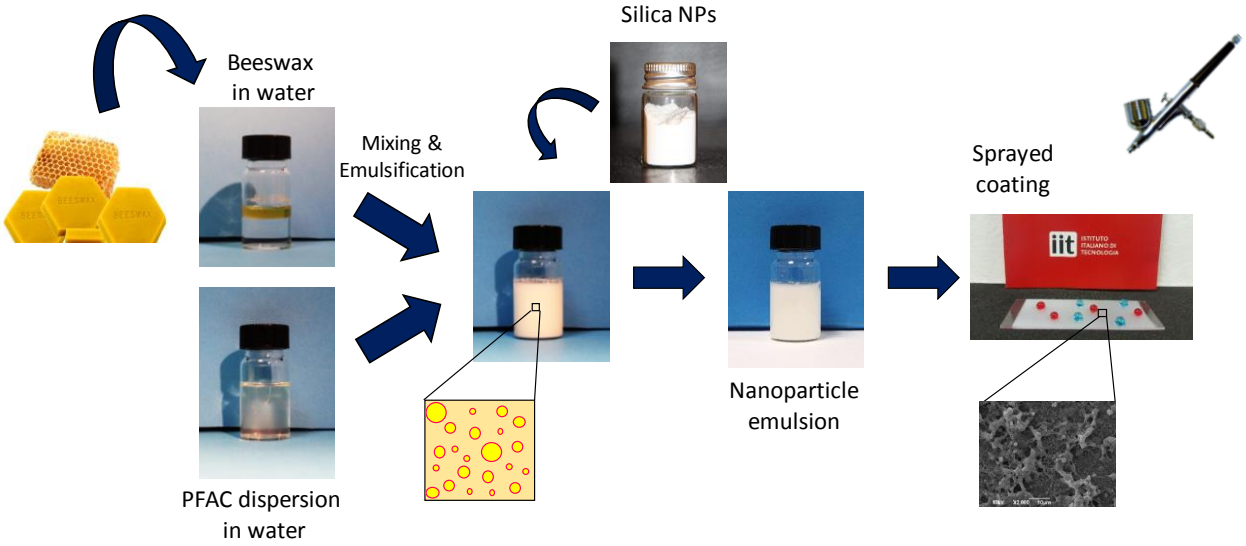

Figure 21. Schematic illustration of oil-in-water emulsion system fabrication and the following superhydrophobic coatings.

To fabricate the final coatings based on the emulsions that were kept for more than a week, first the stored emulsions were ultrasonic processed for 2 hours in ultrasonic bath at 59 Hz (Savatec, Strumenti scientifici, LCD Series, Italy) before spraying, to ensure the redispersion of the components in water. Different emulsions were spray coated onto glass or metal substrates using an internal airbrush spray system (model VL-SET, Paasche, USA), with 200 kPa pressure. The substrtaes were placed onto a hot plate that maintained at 100˚C, due to the quite high boiling point of water and to facilitate the water evaporation rate. The distance between the nozzle and substrate was kept around 15 cm. Table 3 displays different types of the samples that were prepared in this study with their composition to understand the optimum conditions of the coatings fabrication. It's worth noting that for nanocomposites 0.3 wt% silica NPs means that B3 sample has 0.3% nanoparticles by weight respect to total weight of the polymer and wax in the emulsion. On a dry basis, it's translated into 30 wt% nanoparticles in the coating and the resti s 70 wt% polymer/wax blend or 35 wt% polymer and 35 wt% wax.

Table 3. Different sample's composition (all the emulsions were prepared in 50 ml Mili-Q water).

Sample Code	Beeswax (wt%)	PFAC (wt%)	Silica NPs (wt%)
B1	1	-	-

B2	-	1	-
B3	1	1	-
B4	1	1	0.3
B5	1	2	-
B6	1	3	-
B7	2	1	-
B8	3	1	-

3.2.3. Emulsion characterization

First of all, the average particle size of the emulsions was measured through Dynamic light scattering (DLS) method using a Malvern Zetasizer Nano ZS working at 632.8 nm and at 25˚C, with a He/Ne laser. Before the measurements, the emulsions were diluted with deionized water to prevent the particles agglomeration and multiple scattering effects. Then the dilute emulsions were maintained in quartz cuvettes with 10 mm path length. Size distribution pattern as a function of number (%) was obtained and average particle size (z-average, nm) were calculated for each types of emulsions. To prove the repeatability of the results three different samples were analyzed per each emulsions.

The morphology of the emulsified particles was analyzed through transmission electron microscopy (TEM) using a Jeol Jem-1011 microscope under an accelerating voltage of 100 kV. The emulsions were drop-casted onto carbon-coated copper TEM grid and dried under light vaccume before imaging.

3.2.4. Wetting analysis

The wetting properties (static water CAs and RAs) of different samples were measured using a contact angle goniometer (DataPhysics OCAH 200, Germany) at room temperature. By dispensing of 5 µL water droplets onto the surface, the side view images of the samples were captured. To measure the RAs, the water droplets were dispensed onto the coatings followed by continuous tilting of the stage with 1.42 s^{-1}. As soon as the droplets started to roll away on the surface, this angle was recorded as RA of the coating. To confirm the reproducibility of the observations, five different samples were analyzed per each samples, which were produced under same conditions.

3.2.5. Morphological study

The morphology of the fabricated samples was analyzed using a JSM-6490LA microscope (Jeol, Japan) with 10kV accelerating voltage. To prepare the samples for SEM imaging, the emulsions were spray coated onto conductive Al foils and in oredr to reduce the charging effects the coatings were sputter-coated with a 10 nm gold layer. To perform the cross section SEM imaging, the samples were

cryogenically fractured in liquid nitrogen and sputter-coated with a 10 nm gold layer on the fractures surface.

Furthermore, the surface topography of the samples were analyzed using a Park system AFM instrument (XE-100) in non-contact mode. Areas of 10×10 μm^2 were scanned using single-beam silicon cantilever tips (PPP-NCHR-10) with less than 10 nm nominal tip diameter and 42 mNm^{-1} elastic force constant for high sensitivity. The measurements were performed in air in a vibration-insulated environment and an acoustic enclosure. The relative set point was set at 500 nN. The surface roughness was investigated through a built-in grain analysis statistical algorithm known as watershed algorithm. AFM topography images were divided into various regions with a certain average roughness values. Finally, the average roughness of the surface was measured by averaging the roughness values of different areas [93].

3.2.6. Chemical characterization

Fourier transform infrared measurement was used to analyze the chemical structure of the materials using a single-reflection ATR accessory (MIRacle ATR, Pike Technologies) coupled with a FTIR spectrometer (Equinox 70 FTIR Bruker). The measurements were performed in the range from 3800 to 600 cm^{-1} with a resolution of 4 cm^{-1}, accumulating 128 scans.

Furthermore, these measurements were done at different temperatures by using a VeeMAX III ATR device with a heating conversion plate (Pike). After stabilizing the temperature, the samples were located onto the hot crystal and the measurements were done with a resolution of 4 cm^{-1} by doing 128 scans. The full width at half-maximum and wavenumbers of the peaks were determined by using a commercial software Spectra Manager v.2.

The samples were also analyzed through XPS measurements using a SPECS XPS spectrometer equipped with a non-monochromatic Al Kα anode as X-ray source (hν = 1486.6 eV) operated at 12 kV and 7 mA. Then the spectra were analyzed using CasaXPS software. The C 1s component at 285 eV was utilized for charge correction.

3.2.7. Thermal analysis

Thermal characterization of the samples were studied using a Diamond DSC-Perkin Elmer instrument from -50 to 160˚C. The experiments were done under dry nitrogen flow (20 mL min^{-1}) at a heating rate of 20˚C min^{-1}. Approximately 18 mg of each samples were placed into an Al pan and the heating-cooling-heating cycle was recorded. The melting point and enthalpy of fusion of the pure beeswax and coated samples were identified through built-in software asisted numerical integration.

3.2.8. X-ray analysis

Crystalline structure of the materials was obtained using X-ray diffraction analysis with a PANalytical Empyrean X-ray diffractometer. The measurements were done using a CuKα anode (λ = 1.5406˚A) operated at 45 kV and 40 mA from 5˚ to 50˚ 2θ.

3.2.9. latent heat storage properties

The latent heat storage capabilities of different samples were fabricated according to the table 3 were monitored by using an infrared camera (IR-camera) FLIR A655sc model (See Figure 22). These experiments were performed by placing the different coatings onto a hot plate with a certain temperature around 100˚C and then rapidly transferring them on a metal and cold surface with room temperature, which is located in the vicinity of the hot plate. Afterwards, the cooling profiles of each samples including control ones (bare substrate, pure beeswax and pure copolymer coatings) was recorded using IR-camera. Although the surface temperature of each coatings was uniform, but the IR-camera allowed calculation of average temperatures of selected areas over the surfaces. So, the area-averaged temperatures on each coatings surfaces were recorded instead of recording the local temperatures over the samples. At the end, to confirm the latent heat storage properties of the coatings, the cooling profiles of different samples were compared, especially in the regions near to the melting temeparture of beeswax.

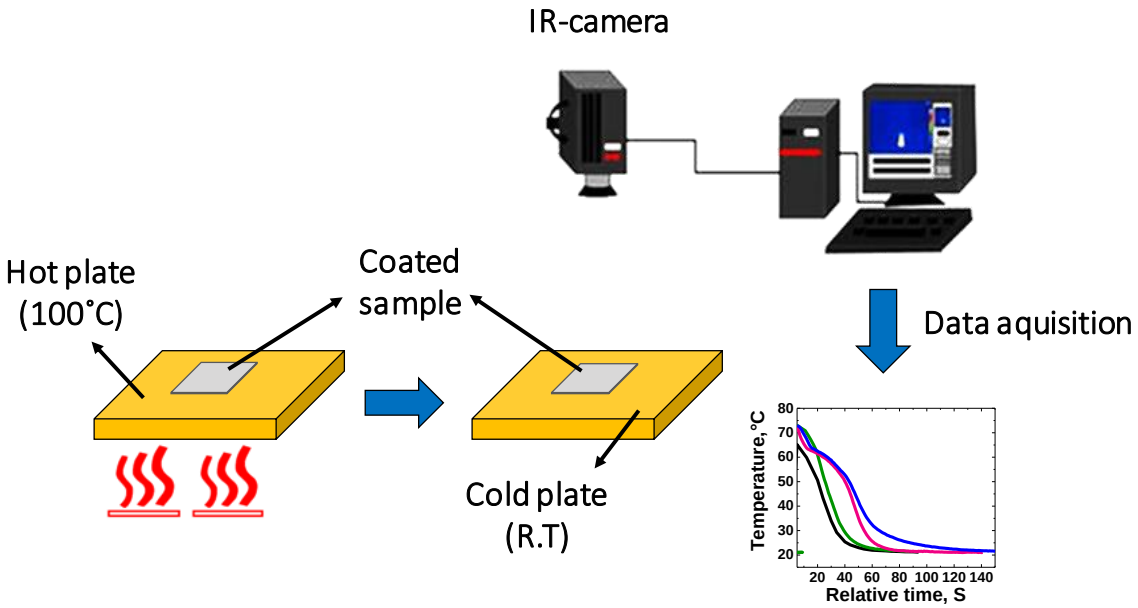

Figure 22. Schematic illustration of infrared camera experimental set-up to obtain latent heat storage capabilities.

3.3. Results and discussion

3.3.1. Emulsion characterization

Studying the literature shows that the number of academic publications about using wax emulsions to fabricate coatings is generally lower than the number of patent publications in this area [148,149]. This fact could be related to the broad range of applications for wax emulsion such as paints and coatings, cosmetics and automative industries. Most of these formulations depend on the wax-in-water emulsion systems, by using different surfactants or stabilizers. In this study, unstable beeswax emulsions are homogenized with waterborne PFAC to make a stable wax-in-water emulsion system. By rapid addition of copolymer dispersion into hot beeswax in water dispersion, we could obtain a really high stable emulsion system during the time, without any phase-separation even after couple of weeks. As it was mentioned in the introduction part, PFAC, which has C6 chemistry does not break down into perfluorooctanoic acid that is toxic for the nature, so this copolymer dispersion is considered as a non-toxic material that does not contain any toxic by-products. Furthermore, they can also act as non-ionic fluorosurfactants, not only to make a stable beeswax emulsion system in water, but also to cover the beeswax particles by making a thin shell around them. Different trials were done to obtain the most stable emulsion system, by making emulsions namely as 3:1, 2:1 and 1:1 wax: copolymer concentration ratio. All the abovementioned emulsions were spray-coated onto the substrates to see the appearance of the coatings and also the emulsions were kept for more than one week, to see the phase-separation of the components. After observations, the emulsions contain 1:1 ratio was selected for futher studies, sue to uniform appearance of the fabricated coating and the highest stability of the emulsion, which can be considered as zero phase-separation after one week.

As the first characterization step, the morphology of the emulsified wax particles in copolymer shell was analyzed under Transmission electron microscopy (TEM) and the results are shown in Figure 23, a. As it can be seen in this Figure, the particles show a core-shell like structure which beeswax was encapsulated with copolymer shell, which is neccessary to fabricate a stable wax-in-water emulsion system.

Average size distribution of different samples, such as beeswax dispersion (before phase-separation), pure copolymer dispersion in water and the blend emulsion contain 1:1 wax: copolymer ratio was investigated through Dynamic light scattering analysis (DLS) and the obtained graphs are displayed in Figure 23, b. The pure beeswax dispersion system, immediately after homogenization process and dilution with distilled water, was tested and it shows a Gaussian distribution centered around 350 nm with a broad distribution function in the range of 100 nm and a micrometer. According to these results, the pure beeswax emulsion before destabilization was considered as a microemulsion system with high amounts of agglomeration particles. On the other hand, the diluted copolymer dispersion in water displays a double distribution pattern comprises of a narrow distribution peak at around 100 nm,

which is related to the polymeric micelles and a broader distribution around 1.5 µm. Despite of this kinds of distribution pattern, the copolymer dispersion was very stable for a period up to three months without any agglometaion and phase-separation. The blend emulsion with 1:1 wax: copolymer ratio shows a distribution function at around 250 nm up to 750 nm, which can be regarded as a stable emulsion system. Comparison between the results of the emulsion system and the pure beeswax dispersion in water, indicates almost 50% redution in the size distribution, which is attributed to the encapsulation of beeswax in fluoroacrylic copolymer shell, which can increase the shelf life of the emulsion to more than 10 days. However, after maintaining the emulsion for couple of weeks, some agglomeration and pahse-separation can be observed, which can be removed before spray coating with simple mechanical mixing or gentle bath ultrasonication process.

Due to the stable emulsion morphology, various quantities of hydrophilic modified silica NPs can be dispersed into the emulsion to create superhydrophobic nanocoatings, which is the final goal in this work. Moreover, by encapsulation the beeswax inside the copolymer shell, it's possible to avoid the leaching behaviour of easily liquefying beeswax, to obtain a coating with reversible latent heat storage property.

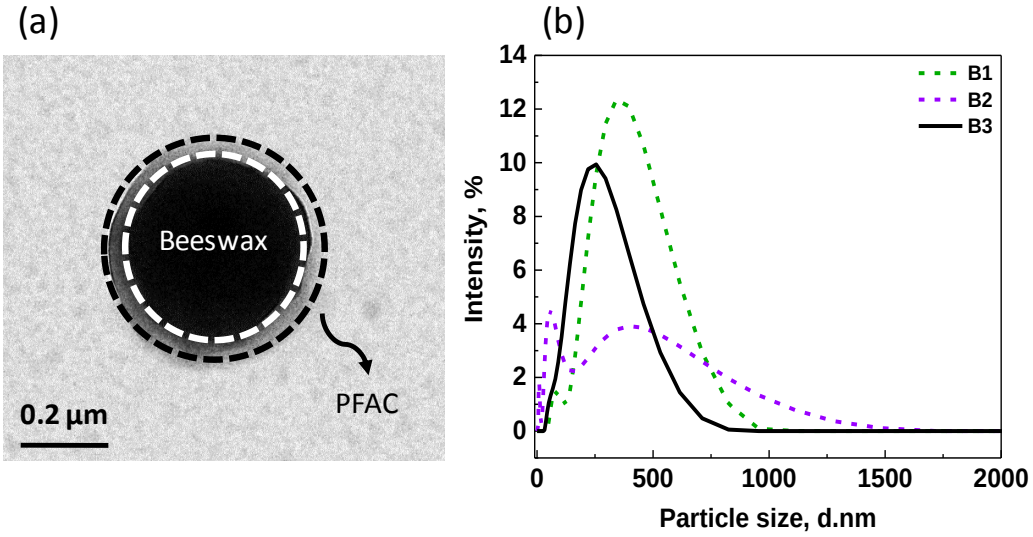

Figure 23. (a) TEM image of emulsified core-shell like structure in the emulsion system. (b) Size distribution of pure beeswax (B1), pure copolymer dispersion (B2) and the blend emulsion system in water (B3).

The most possible chemical structure of PFAC is shown in Figure 24. To follow the C6 chemistry and environemntal regulations, the side chain number, *n*, in this structure should be 6 or less. These types of acrylics are not very long chain or high molecular weight polymers, they can act as surfactant-like macromolecules due to the perfluorinated side chain structure and also the copolymer nature in

the main backbone. So they can be considered as perfluorinated surfactants [150]. They can work as dispersing agents for oily or hydrophobic dispersions in waterborne formulations such as paints, inks and even drug-delivery systems [151].

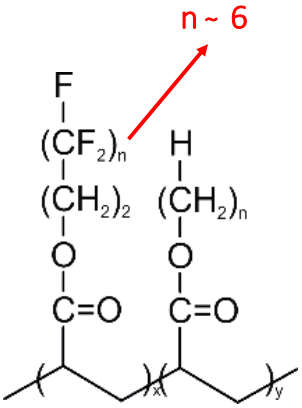

Figure 24. The most possible chemical strucure of PFAC.

3.3.2. Chemical characterization of the materials

To do these measurements, pure beeswax, Pure copolymer and the blend emulsion in water were spray coated onto the silicon wafer substrates and the coatings were chemically analyzed using an attenuated total reflection (ATR)-Fourier transform infrared (FTIR) spectroscopy and the results are shown in Figure 25. The main peaks for pure beeswax were ascribed to ester (C=O and C-O-C stretching modes at 1736 and 1171 cm^{-1}, respectively) groups, scissoring and rocking bending doublets at 1468 and 725 cm^{-1}, respectively) and methylene (assymetric and symmetric CH_2 stretching modes at 2915 and 2849 cm^{-1}, respectively in crystalline form [152]. The chemical structure of PFAC is composed of perfluoromethylene (assymetric and symmetric CF_2 strteching modes at 1233 and 1142 cm^{-1}, respectively) and ester (C=O and C-O-C stretching modes at 1730 and 1188 cm^{-1}, respectively) functional groups [147]. After blending of these two components in emulsion system (B3 sample), no significant chemical shifts or appearance of new chemical bonds respect to the pure materials was observed. It means that both components do not chemically interact with each other and they just physically blend together. However, surprisingly, the methylene groups chemical bands associated to assymetric and symmetric CH_2 stretching, scissoring and rocking bending modes for pure besswax and blend emulsion are shifted in adifferent way towards temperature. Here, we focused on asymmetric and symmetric CH_2 stretching modes for pure beeswax (B1) and emulsion system (B3) samples (See Figure 25, b). The wavenumbers and full width at half of the maximum of the peak (FWHM) for B1 and B3 samples are compared in Figure 25, c. It can be seen that in general there is an increase in wavenumbers in the range of 34 to 66˚C, which is attributed to the melting

temperature of beeswax or solid-liquid phase change behaviour of wax materials [153]. Generally, the wavenumbers and FWHM for both asymmetric and symmetric CH_2 stretching modes for the emulsion system has higher values compared to the pure beeswax. This phenomena could be attributed to the higher number of gauche conformers in the emulsion system rather than beeswax that caused by higher alkyl aliphatic chain disorders with increasing temperature in the emulsion system, which induced in the presence of fluorinated copolymer in the blend emulsion [149].

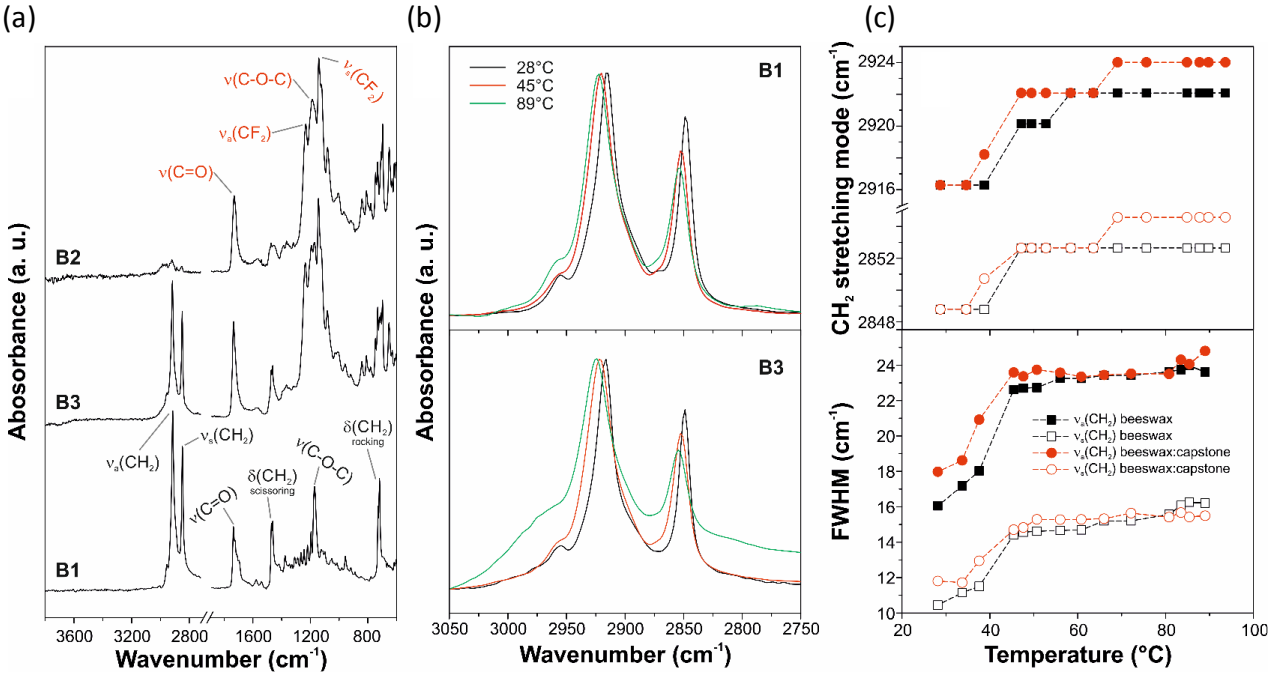

Figure 25. (a) ATR-FTIR spectra of B1 (pure beeswax), B2 (pure PFAC), and B3 (blend emulsion with the same amounts of both components) samples in the 3800-600 cm^{-1} region. The main assignments are included for beeswax (black), and PFAC (red). (b) CH_2 stretching mode infrared spectral region for B1 and B3 samples at 28 (black), 45 (red), and 89°C (green). (c) Variation of the wavenumber (top) and FWHM (bottom) of the asymmetric (filled symbols) and symmetric (empty symbols) methylene stretching modes of B1 (black) and B3 (red) with the temperature [36].

The chemical structures of the blend emulsion (B3) and nanocomposite one (B4) were analyzed through X-ray photoelectron spectroscopy (XPS) and the obtained graphs are shown in Figure 26. The high-resolution C 1s spectra of both samples indicates a fluorinated surface by presenting two peaks at 294.0 ± 0.1 eV and 292.4 ± 0.1 eV, associated to CF_2 and CF_3, respectively. These observations confirmed the encapsulation of beeswax in fluoroacrylic copolymer shell in the emulsion system.

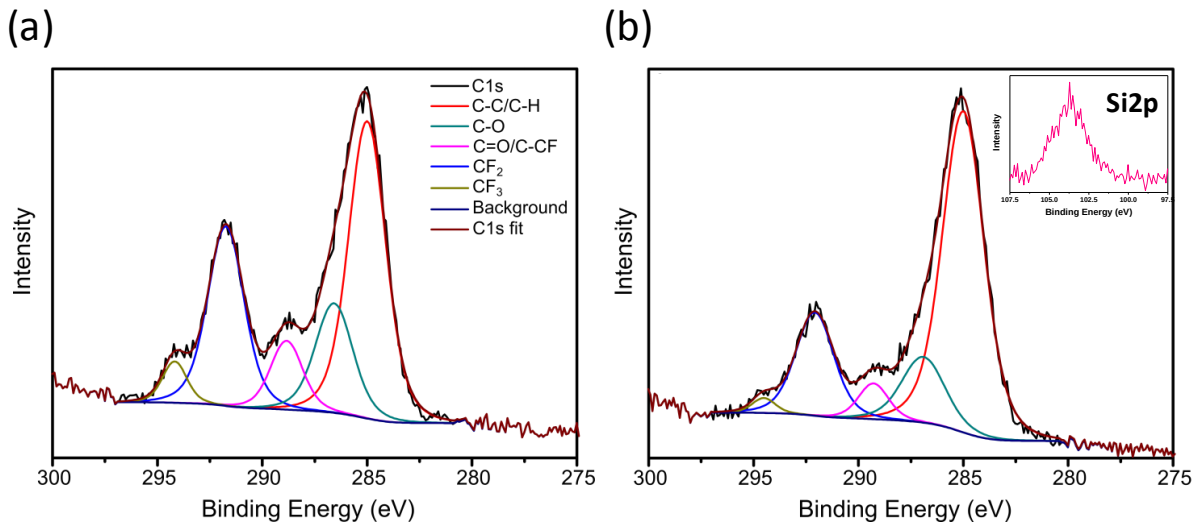

Figure 26. XPS high-resolution C 1s spectra for samples (a) B3 and (b) B4 [36].

The fluorine content in the surface of the B3 and B4 samples, which derived from the quantifications of the corresponding high-resolution spectra, was around 16.7% and 14.3% for B3 and B4, respectively (See Table 4). Lower quantities of fluorine in sample B4 compensated by presenting of silica NPs in the outer surface of the emulsified particles in emulsion media, which is essential for water-repellency of the final coating. Appearing a new peak at around 103.7 eV, which is ascribed to Si 2p band [154], was induced to detection of 3.8% silicon in sample B4.

Table 4. Elemental composition of the surface coatings of B3 and B4 with atomic percentage.

Sample code	C (%)	F (%)	O (%)	Si (%)
B3	78	16.7	5.3	0
B4	74.5	14.3	7.4	3.8

3.3.3. Wetting analysis

The wetting properties (contains static water CAs and RAs) of different samples were investigated by goniometer and the results are displayed in Figure 27, a. The static CAs of the coatings from pure beeswax (B1), pure copolymer (B2) and the blend emulsion with 1:1 ratio (B3) was reached up to 110˚, which is in the range of hydrophobicity [155]. All of these coatings showed droplet mobility only in the form of sliding droplets, not rolling away on the surface at tilting angles of 90˚. This behaviour was in contrast with very hydrophobic materials like silicones, which they do not show

any droplet mobility even at tiltimh angles more than 90˚. The sliding angle concept should not be confused with free droplet roll away motion [156].

To optimize the concentration of silica NPs to acquire self-cleaning superhydrophobic coatings, different amount of silica NPs were dispersed into the emulsion matrix and the wetting properties of the spray coated samples from these solutions were measured. Five different samples were obtained by dispersing 0.1, 0.2, 0.3, 0.4 and 0.5 wt% silica NPs in the 1:1 emulsion system. As it was mentioned in the experimental section, this means that the silica NPs concentration in the dry coatings has ranging from 10 to 50 wt% respect to the polymer/ wax weight. Wetting results of these five samples are presented in Figure 27, b. This graph indicates that superhydrophobic threshold (CAs more than 150˚) can be acheived by using 0.3 wt% silica NPs or more. However, by using lower amounts of silica NPs, the static contact angles are still below this range. Moreover, the RAs of these coatings were measured below 10˚, which is neccessary for self-cleaning property. Finally, the nanocomposite contains 30 wt% silica NPs was selected as B4 sample for further studies, due to the good wetting properties along with lowest amount of silica NPs that used in this formulation to reach to this level. The RA of B4 smaple was recorded as 5.5˚ after dispensing of 5µL water droplets onto the surface.

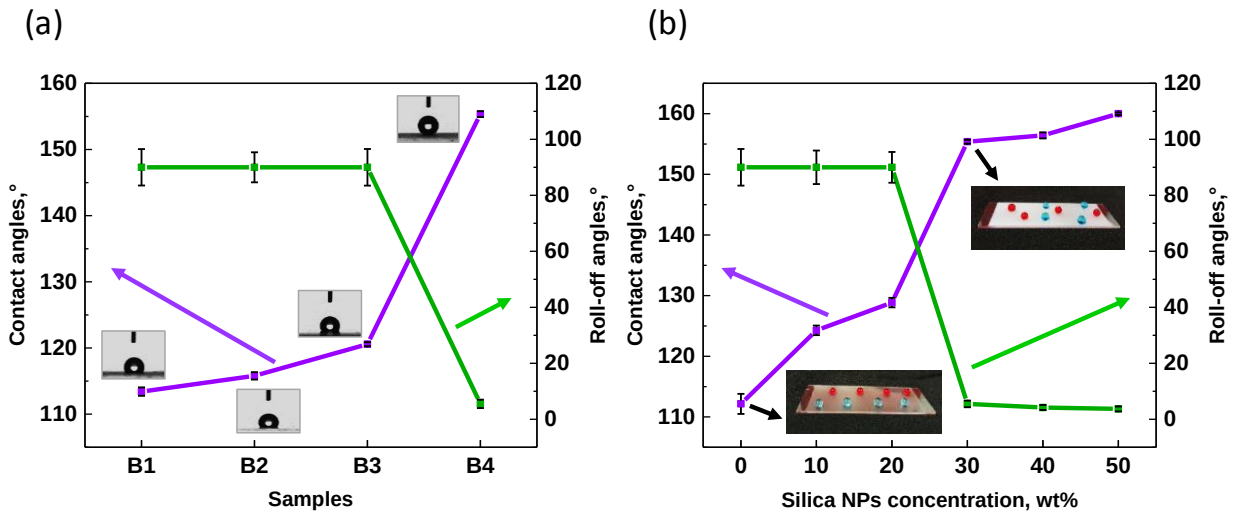

Figure 27. (a) The wetting properties of different samples. (b) Optimization of the silica NPs concentration by measuring the static CAs and RAs.

3.3.4. Morphological study

The surface and cross section morphology of the samples B3 and B4 were analyzed under Scanning electron microscope (SEM) and the obtained images are shown in Figure 28. The emulsion sample displays a really smooth and flat surface morphology containing some craters on the surface as it can be seen in cross section image of this sample (See Figure 28, c). This morphology could be related to the arrangement of the micrometer-sized emulsified wax droplets that embedded into the polymer

matrix and they solidified as sphere particles inside the emulsion media. However, after dispersing silica NPs into the emulsion system, the surface morphology changed compeletely, as it's obvious in Figure 28, b. This morphology is similiar to the submicrometer vascular structure of the rose petal or similiar flowers, which is created by silica NPs in the surface [157]. This type of surface morphology is quite different from superhydrophobic microstructure of fluorinated acrylic copolymer-silica NPs coatings worked earlier by our group [79]. In cross section image of the sample B4, a random rough structures can be seen which is drstically different from the emulsion system.

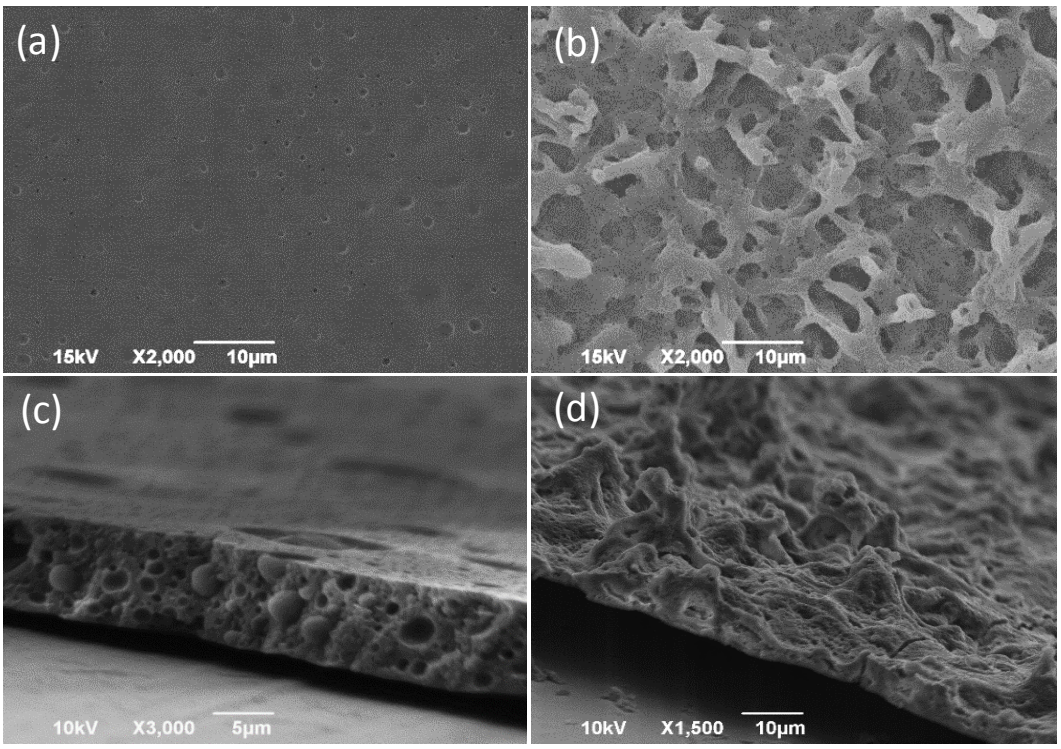

Figure 28. Surface SEM images of (a) B3 and (b) B4. Cross section SEM images of (c) B3 and (d) B4 samples [36].

Furthermore, the surface roughness and the effect of silica NPs onto the emulsion system was investigated by atomic force microscopy (AFM) and the results are shown in Figure 29. The average surface roughness values of the smaples B3 and B4 were determined after several AFM measurements. As it was discussed previously, watershed grain algorithm was used to analyzed the average surface roughness of these samples [94]. The average surface roughness was measured as 120 ± 40 nm and 420 ± 50 nm for the B3 and B4 samples, respectively. The topography of the B3 sample shows a really flat surface, which is in agreement with the SEM analysis images. The higher value for the B4 sample indicates the increment in average roughness value of this sample, which is

due to the creation of flower petal-like rough structures on the surface that is ascribed to the dispersion of silica NPs into the emulsion system.

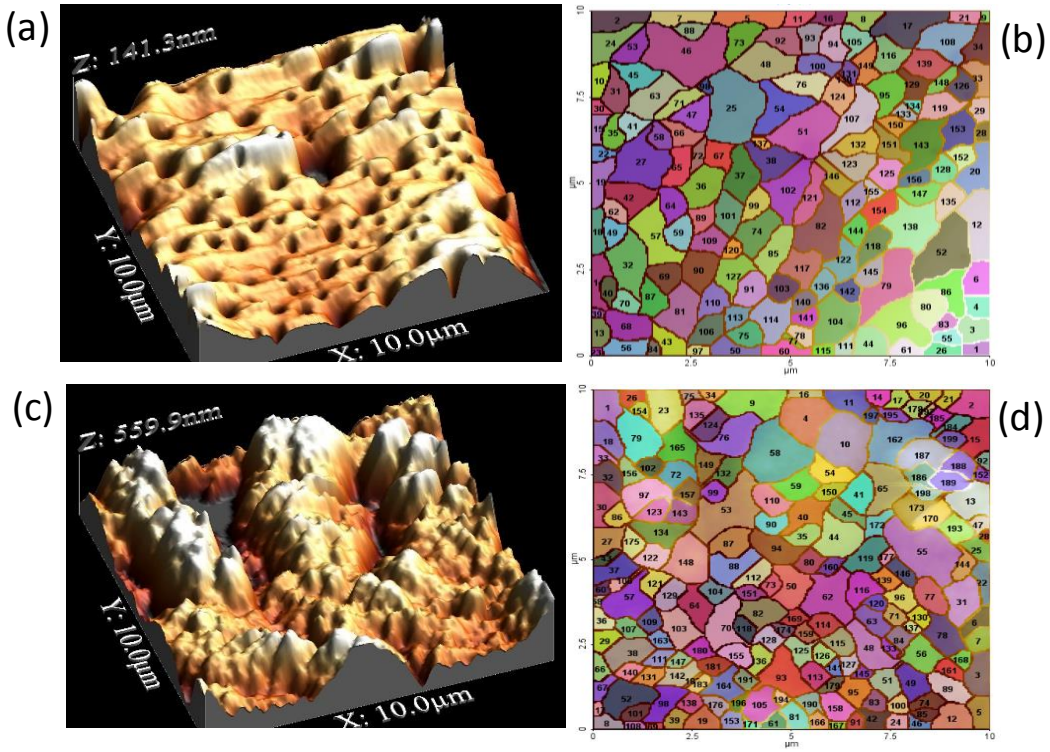

Figure 29. AFM topography: 3D images of (a) B3 and (c) B4 samples. Watershed grain analysis of (b) B3 and (d) B4 coatings (Zones with different colors related to the arears with different surface roughness values) [36].

3.3.5. Latent heat storage capabilities

The phase-change property or latent heat storage capability of the coatings were studied by using an infrared camera (IR) camera imaging. Before doing these measurements, thermal properties of the coatings were analyzed by using Diffrential scanning calorimetry (DSC) and the obtained graphs are shown in Figure 30. The obtained results contained the melting temperatures and calculated enthalpy of fusion of different samples are summarized in Table 5.

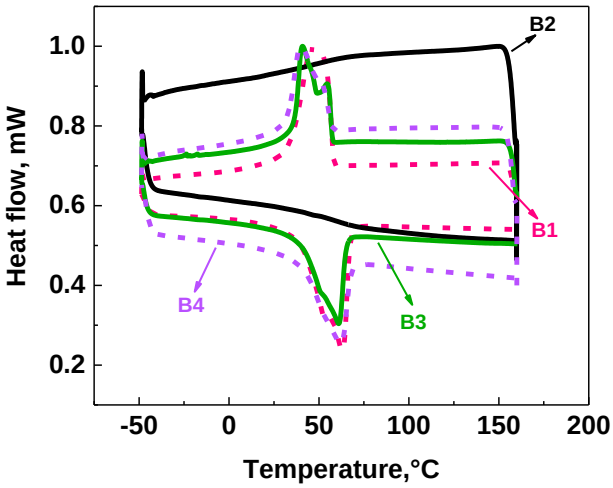

Figure 30. DSC thermograms of different samples, pure beeswax, pure copolymer, B3 and B4 samples.

The melting temperature of the beeswax was measured around 62.4˚C, which is in greement with the other studies [158,159]. However, the melting temperature of the emulsified wax droplet into the copolymer matrix was measured around 60.8˚C. This depletion could be related to the deformation or partial amorphization of crystalline stucture of beeswax. To understand this effect, the original crsytalline structure of beeswax was studied by X-ray diffraction (XRD) analysis and the ontained patterns are shown in Figure 31. The XRD pattern for the beeswax shows the reflections centered at 19.1, 21.3, 23.6, 29.8 and 40.3˚, which could be related to the orthorhombic structure of beeswax [160,161]. After emulsification of beeswax in water through the formation of copolymer shell around the beeswax particles, some rearrangements happened in the crystalline structure of beeswax, which can be seen by decreasing the intensity of the peak at 19.1˚ and disappearing the peak at 40.3˚. These changes in the crystalline structure of beeswax can have impacts on thermal properties of the coatings, which can be seen as decreasing of melting temperature of the B3 and B4 samples compared to the pure beeswax. The enthalpy of fusion of pure beeswax was calculated from the area under the melting peak in DSC thermogram and was measured around 155.3 J g^{-1}. This value is really close to the number for waxes collected from cavity resting honeybees like Apis cerana, Apis mellifera and etc [162]. However, this value is higher than the enthalpy of fusion of inductrial semicrystalline polymers like polyesters [163], while it happend at much lower temperatures, which is ideal for environmental phase-change material applications.

This parameter was measured around 84 J g^{-1} for B3 and B4 samples, which is decreased around 46% respected to the pure beeswax, due to the presence of copolymer in the emulsion system, which does not have the phase-change property by itself. Acrylic copolymer by creating a polymer shell around beeswax particles can disrupt the onset and end temperatures related to the melting step of beeswax,

which caused to decrease the enthalpy of fusion. However, there are some other natural beeswaxes with lower heat of fusion, such as the ones made by common Melipona bee species [162]. The advantage of encapsulating of beeswax particles into the polymer shell is that it can be protected from the environment by avoiding the leaching behaviour, even at higher temperatures than melting point of wax. So, there is a tradeoff between high enthalpy of fusion with poor structural stability in pure beeswax and good structural stability with lower heat of fusion in the coatings obtained from the emulsion system.

It's worth noting that the coatings from beeswax can be maintained at 60 and 100˚C for up to one year in controlled chambers without any degradation of beeswax, except the degradation in the presence of heavy alcohols that can be evaporate depends on the origin of beeswax [164]. The use of acrylic copolymer has an extra advantage, by inhancing the substrate adhesion in the final coatings, whitout any delamination after 3 months under ambient conditions.

Table 5. Thermal properties; melting temperatures and enthalpy of fusion of different samples, pure beeswax, B3 and B4 samples.

Property	Beeswax	B3	B4
Melting Temp.	62.4	60.8	61.7
Enthalpy of fusion	155.30	84.1	84.2

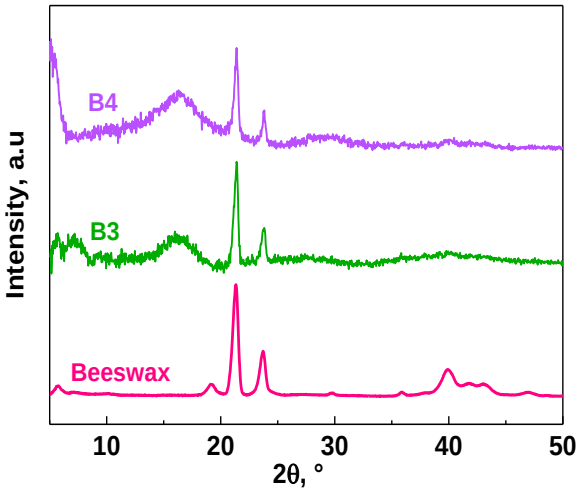

Figure 31. XRD patterns of pure beeswax, B3 and B4 samples.

At the final step, the heat storage capability of the coatings were analyzed by using an IR-camera through obtaining the temporal cooling profiles of different coatings, by spray coating on the stainless steel substrate and the results are shown in Figure 32. The cooling profiles were recorded by IR-camera after rapid transferring the coatings from hotplate at 100˚C to a surface at room temperature. The curve with the name of substrat donates to the bare stainless steel substrate without any coating on it and the copolymer ones is related to the pure copolymer coating, which they were measured as control samples. According to the graph in Figure 32, a the rapid cooling or quenching behaviour in cooling profiles means that the coating does not show any latent heat storage property, however the slow, stepwise pofile indicates the latent heat storage capabilities, which can store heat for a while [165]. For the bare substrate and pure copolymer coating, a rapid and quenching behaviour is observed, which occures in the first 50 s of the experiment and after 300 s both samples shows temperature lower than 40˚C. However for the samples B1, B3 and B4 the cooling profiles are quite different, where the temperature for these samples after 100 s are about 15˚C higher than the temperature of the bare substrate and the pure copolymer coating. Indeed, the coatings with higher portions of beeswax like the samples B7 and B8, shows the step-wise behaviour (two quasithermal arrest zones) [166], in their cooling profiles, which means that they can remain warmer respect to the other samples and the first quasithermal arrest zone appeared in the first 150 s. All other samples that contain beeswax in their formulations such as the superhydrophobic coating ones, show single step cooling profiles between 100 and 300 s. The step size and the cooling trends depends on the relative propertion of beeswax to acrylic copolymer. These areas with very slow cooling profiles are regarded as quasithermal arrest zones and the slope could be around zero, due to the low cooling rate in this area, which makes ideal for heat storage [166].

In the samples with higher amounts of fluorinated copolymer compared to beeswax, like the samples B5 and B6, the thermal arrest zone will be smaller and it took place earlier than the other samples that has higher quantities of beeswax.

Figure 32, b shows the cooling rate of some selected samples as a function of time ($^{\circ}Cs^{-1}$). The cooling rates were obtained from the slope of the cooling curves in Figure 32, a. These calculations were done to make an easier interpretation of the cooling profiles, in the sence that high cooling rates with sudden falls or jumps display poor or no latent heat storage properties. In the other words, there is a very large difference in the column intensity in Figure 32, b for the bare substrate and pure copolymer coating, which is due to the absence of latent heat storage effect. However, for the other samples, B3, B4 and B8, these trend is more uniform during the time, which means that due to the phase-change property of beeswax, these samples show reduced cooling rates respect to the bare substrtae and the pure copolymer coating. It can be seen that for these three samples, even after 200 s, the coatings

show a residual heat release, while for the bare substrate and the pure copolymer coating, after 200 s they reached to room teperature and the cooling process stopped.

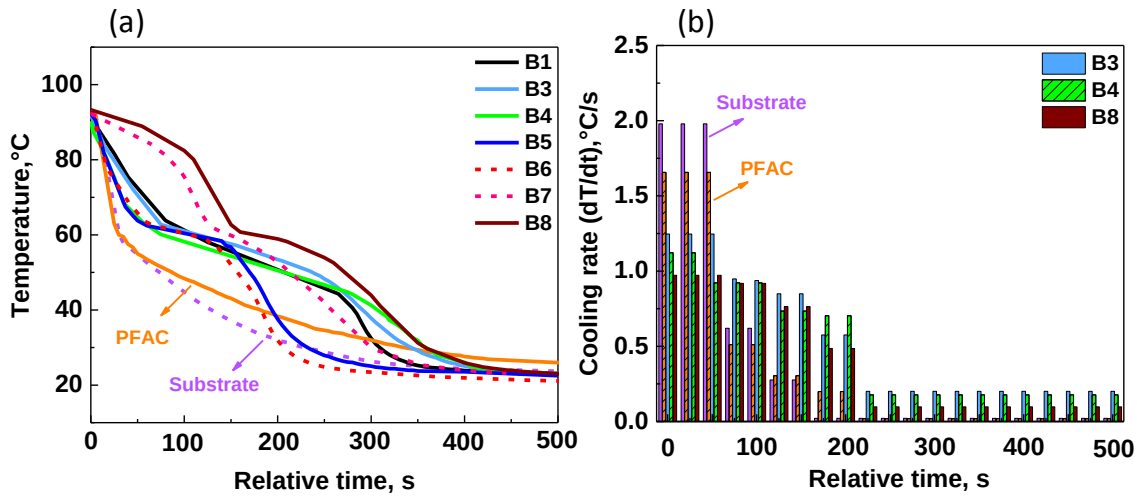

Figure 32. (a) Cooling profiles of different samples as a function of time. (b) Cooling rates of some selected samples as a function of time [36].

This phenomena can be better understand by looking at some selected IR- camera images from different samples, which are indicated in Figure 33. According to these images and the temperature bar, the sample that has higher amount of beeswax, B8 sample, has higher temperature after 5 min respect to the bare substrate and B2 sample that does not contain any phase-change material. It's also obvious that the bare substrate and the pure copolymer sample reached to the room temperature after 5 min, which means the quenching bahaviour in their cooling profiles.

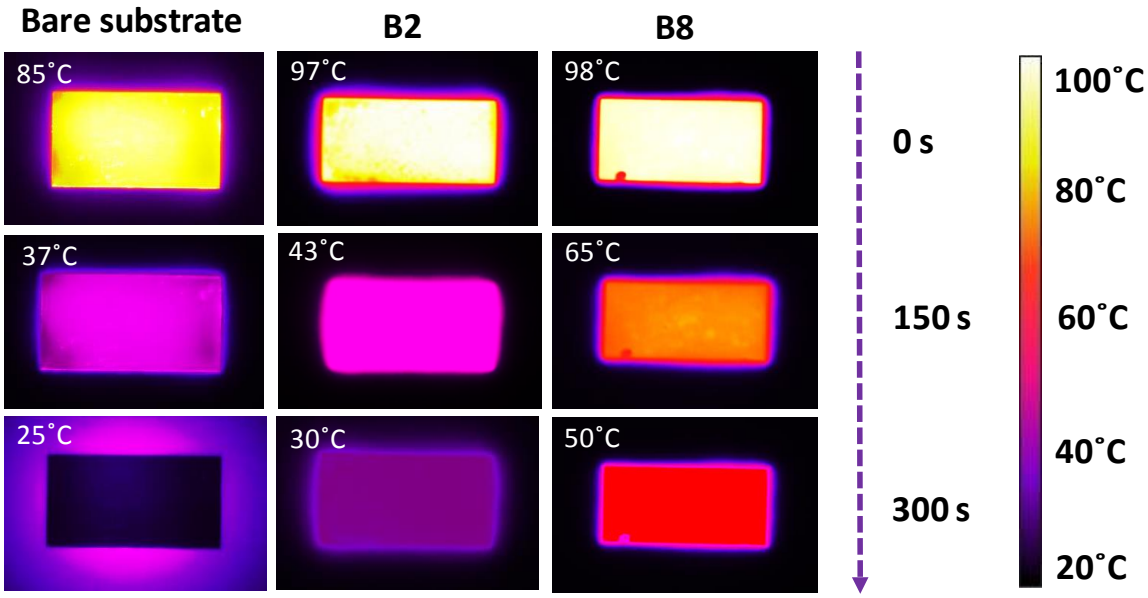

Figure 33. IR-camera images of the bare substrate, pure copolymer and B8 samples [36].

3.4. Conclusions

In this work, we fabricated an all water-based, superhydrophobic coatings with latent heat storage properties based on beeswax-in-water emulsion system for the first time. This coating can be used in many various applications, where thermal management is needed. Beeswax were emulsified in water by means of an environmentally-friendly water dispersed perfluoriacrylic copolymer, which acts as an interna emulsifier/ surfactant. The emulsions were obtained by use of a desktop sized homogenizer and were stable for a couple of weeks. These emulsions can be fabricated by tuning the wax: polymer ratio, whithout changing the stability of the emulsion. Then the emulsions can be sprayed onto the different substrates such as glass or metals. To obtain the non-wetting property, silica NPs were dispersed into the emulsion system. The coatings that were rich in beeswax, including the final superhydrophobic coating, showed latent heat storage capabilities. This presence of this property is due to the core-shell like structure, which made by encapsulation of beeswax into the acrylic copolymer shell that can solve the main problem of phase-change property of beeswax. So, the coatings can be heated more than 62˚C (melting temperature of beeswax) and can be act as a latent heat storage materials during their cooling profiles. These coatings can be used in various applications such as electronics to structural building energy management systems and thermal energy savings. Moreover, due to the water-based system by using eco-friendly materials in this work, the production of these coatings can be easily scaled-up.

Chapter 4

Superhydrophobic Coatings with Reduced Bacterial Adhesion based on a Bioresin

4.1. Introduction

In today's world, there is a growing interst towards bio-based materials, which can be replaced with the conventional compounds in different aspects of the life [167,168]. Due to the environmental concern that is intensifing continusely, the use of these kinds of materials has attracted a great attention. Furfural is a biomass derivatives, which can be converted into polyfurfuryl alcohol (PFA) through hydrogenetaion into furfuryl alcohol (FA), followed by cationic condensation and polymerization [169,170]. Owing to high compatibilty of PFA with many organic and inorganic materials, it can be used in a broad application such as corrosion-resistant coatings [171,172], wood adhesives [173], etc. PFA is a thermally crosslinked resin [174], which can be used as a robust binder for fabrication of polymer nanocomposites for different applications including separation membranes [175], lithium batteries [176], nanostuctured carbon materials [174], etc.

Recently, the developement of bio-based water-repellent surfaces has attracting too much attention from both academy and industry sides, due to their biocompatibility, fascinating characteristics and potential coverage on different substrates such as metals, ceramics and polymers.

However the liquids such as oils would dispense on almost all the natural and synthetic surfaces, due to the lower surface tension values (31.00-39.00 mN m^{-1}) [177,178] and the surface would be contaminated with these types of liquids. Hence, the importance of the oleophobicity along with superhydrophobicity dragged the research attentions towards liquid-repellent surfaces, which can be used in various fields such as self-cleaning [129,179], non-fouling [35,180], corossion-resistant coatings [95,181], anti-fingerprint [182] etc.

Herein, we present a simple and environmentally-friendly technique to fabricate a biocompatible superhydrophobic coating, based on PFA and a commercial waterborne PFAC dispersion in acetone. It's worth noting that the waterborne acrylic copolymer dispersion follows the Environmental Protection Agency (EPA) 2010/2015 perfluorooctanoic acid (PFOA) stewardship program, which confirm that PFAC does not contain any C-8 fluorochemistry and does not breakdown into PFOAs in the environment [147]. Due to the high compatibilty of PFA with other organic materials, there is a good miscibility between these two polymers, which is important to have a uniform coating. Moreover, hydrophobic fumed silica NPs can easily be dispersed into the stable blend solution, to make the surface roughness in the final coating. Furthermore, we demonstrate that the nanocomposite has a good biocompatibility property, which can affect on the final application of the nanocpmposite.

4.2. Experimental section

4.2.1. Materials

Polyfurfuryl alcohol (PFA) was purchased from Polysciences Inc. and used as received. A commercial water-dispersed PFAC was purchased from DuPont, USA, which is consisted of ≈20 wt% cationic fluoroacrylic copolymer dispersed in water. The hydrophobic fumed silica NPs, Aerosil® R-812, with an average particle size around 7-40 nm were kindly donated by Evonik Industries, Germany. Trifluoroacetic acid (TFA), acetone and isopropanol were purchased from Sigma-Aldrich and used as received. Commercial aluminium foils (2 cm × 2 cm, thickness: 1 mm) were used as substrates.

4.2.2. Preparation of the samples

All coatings were prepared via spray deposition method onto Al-foil substrate. First of all, the commercial PFAC was extracted from water and dissolved in acetone. The procedure was started by dropwise adding TFA into the water dispersed copolymer solution and precipitation of the polymer, followed by washing the precipitate with water and isopropanol and let it dry. Then the polymer precipitate was dissolved into acetone with certain concentration.

For preparation of the final solution, PFA was dissolved in acetone and vortexed for 2 min. the extracted PFAC in acetone was added into the PFA solution and mixed for half an hour, to create a 50:50 or (1:1) blend. To fabricate the nanocomposite solution, certain quantity of silica NPs was added into the blend solution and dispersed in it furthur by probe sonic processing (Sonics, Vibra cell, USA) for 1 min to make nanocomposite solution. In order to make the solutions more stable during the time and ready to spray deposition, they were ultrasonic processed for 2 h in ultrasonic bath at 59 Hz (Savatec, Strumenti scientifici, LCD Series, Italy) (Figure 34). The lists of the samples were prepared and analyzed are listed in the Table 6.

Table 6. Sample's formulations (all the samples were prepared in 30 ml acetone).

Sample Code	PFA (wt%)	PFAC (wt%)	Silica NPs (wt%)
S1	10	-	-
S2	-	10	-
S3	5	5	-
S4	5	5	0.3

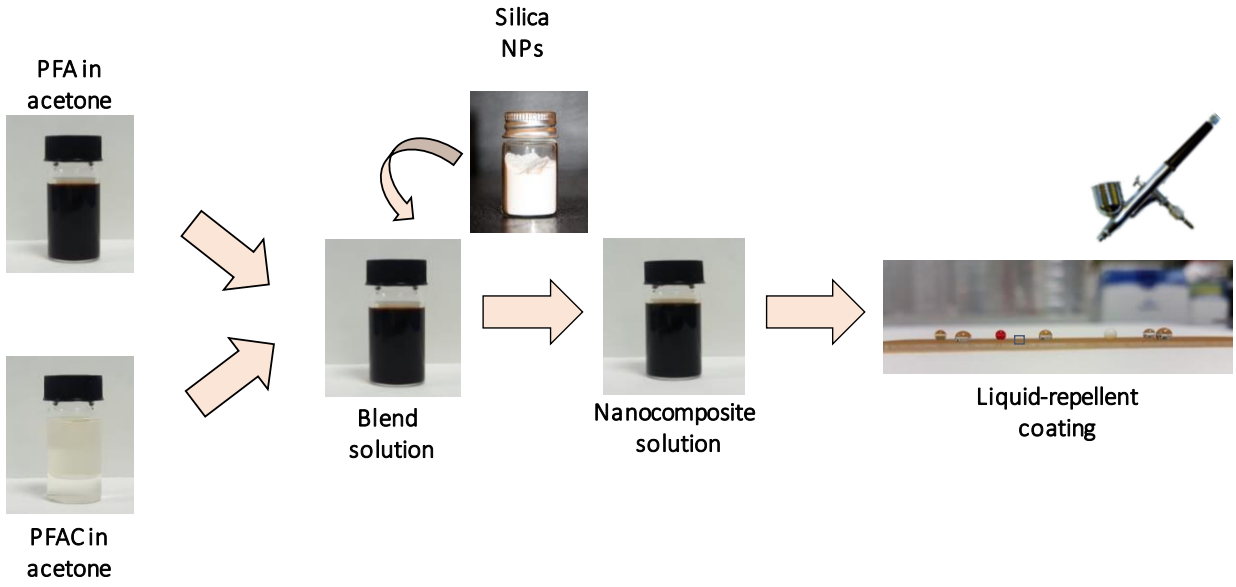

Figure 34. Schematic illustration of sample preparation technique.

4.2.3. Wetting analysis

Wettability of the surface, static CAs and RAs were measured by using a contact angle goniometer (Dataphysics OCAH 200, Germany) at room temperature, by dispensing different liquid droplets, such as water, olive oil, soybean oil, milk, coca cola, silicon oil and hexadecane. 8 µL various liquid droplets were dispensed on the surface and the CAs were calculated from the side view. To measure the RAs, 6 µL liquids droplets were dispensed onto the coating's surface and the stage was continuous tilted with 1.26° s^{-1} angular velocity. As soon as all the droplets started to roll away from the surface, the tilting angles were recorded as RAs. To confirm the reproducibility of the results, five different measurements were performed on different samples, which were prepared under same conditions.

4.2.4. Chemical characterization

To study the chemical structure of the final nanocomposite, Infrared spectra were performed by using a single-reflection ATR accessory (MIRacle ATR, Pike Technologies) coupled to FTIR spectrometer (Equinox 70 FTIR, Bruker). All spectra were recorded in the range from 4000 to 600 cm^{-1} with 4 cm^{-1} resolution, accumulating 128 scans. To prove the reproducibility of the spectra, the measurements were done on three different samples of each coating, which were fabricated under identical conditions.

XPS analysis were performed to study the chemical composition on the surface of the coatings, by using a SPECS XPS spectrometer equipped with a non-monochromatic Al Kα anode as X-ray source (hν = 1486.6 eV) done at 12 kV and 7 mA. The spectra were analyzed using CasaXPS software and the C 1s component at 285 eV was used for charge correction.

4.2.5. Morphological characterization

Scanning electron microscope (SEM; JSM-6490LA) (JEOL, Japan) was used to study the microstructure morphology of the fabricated coatings with 10 kV acceleration voltage. Firstly, the spray-coated samples onto the conductive Al-foils were sputter-coated with 10 nm gold layer, to reduce charging effects.

To identify the elemental distribution of the coatings, Energy dispersive X-ray (EDX) analysis were done at 10 mm working distance with 10 kV acceleration voltage and 15 sweep counts per each samples.

Optical Zeta-20 optical profilometer was utilized to study the 3D measurements of surface morphology of the coating's surface and to obtain the related topography. The images were acquired in non-contact mode. Areas of 664×499 µm were scanned by using 20× magnification optical microscope. The measurements were done in air in ambient temperature with 0.451 µm stepsize and number of step of 92. The roughness characteristics of the surface were calculated by Zeta analysis in the whole measured area.

4.2.6. Biocompatibility study

HeLa cells (ATCCs, UK) were cultured in Dulbecco's modified Eagle medium (DMEM, ThermoFisher) 10% fetal bovine serum inactivated, and 1% penicillin streptomycin in an incubator at 37°C and 5% CO_2. For the indirect biocompatibility tests, a 50:50 blend and a 30 wt% nanocomposite films were first sterilized under UV for 30 minutes, rinsed with sterile water. The sterile films were submerged in DMEM culture medium for 48 hours; HeLa cells were seeded in the conditioned DMEM at a density of 2×10^4 cells ml^{-1} and let to grow in an incubator until they were confluent. For control, HeLa cells were also cultured in normal DMEM at the same density. Cells were fixed in 4% formaldehyde solution in PBS for 10 minutes at room temperature. For imaging, the fixed cells were first permeabilized in 0.5% Triton X-100 (v/v) solution in PBS for 15 minutes and then blocked in 3% Bovine Serum Albumine (BSA)solution in PBS (w/v); after each incubation steps cells were thoroghly rinsed with PBS three times. Cells' nuclei were stained with Hoechst (ThermoFisher Scientific, USA), 1 µg ml^{-1} for 20 minutes; Alexa-Fluor 488-phalloidin (Invitrogen) was used to label the cytoskeleton following the manufacturer's protocol (6.6 µM methanolic solution of phalloidin were diluted 1:1000 in PBS containing 1% BSA to reduce unspecific background and a 200 µL drop was placed on each coverslips for 30 minutes. After rinsing in PBS, the coverslips were mounted on glass slides using ProLong mounting medium. The cells were imaged using a Nikon Inverted Microscope TiE equipped with a Nikon Confocal Laser System (Nikon Optical Co., Ltd, Japan) at an excitation wavelength λ_{ex} = 405 nm, and λ_{ex} = 488 nm at a 20× magnification.

A proliferation assay in the previously conditioned DMEM films for 48 hours was performed with an xCELLigence device (ACEA Biosciences) equipped with E-plate 16 with a view window for

optical inspection. The device allows the real-time monitoring of cell viability, based on electrical impedance read out. For each condition (i.e., DMEM conditioned with 50:50 blend, DMEM conditioned with 30 wt% nanocomposite film, and normal DMEM) 4 different wells were used. Each of the 4 well was filled with 150 µL of conditioned DMEM. After background measurement, 50 µL (1500 cells/µL) of HeLa cell suspension in DMEM was added to the wells. The proliferation assay was run for 120 hours in the incubator. Sampling of the cell proliferation was done every 15 minutes by reading out the impedance of the electrodes, and converting it to a dimensionless parameter, named Cell Index (C.I.) proportional to the electrode area covered by the cells [183]. The C.I. matrix was then processed by IgorPro (Wavemetrics).

4.2.7. Bacterial adhesion analysis

The bacterial adhesion property of S1, S2, S3, S4 materials and uncoated glass (control) was evaluated by using *Escherichia coli* (*E. coli*) and *Staphylococcus aureus* (*S. aureus*). Before the adhesion test the analysed samples were sterilized under UV at 254 nm for 30 minutes. A single colony of *E. coli or S.aureus* was inoculated in LB broth (50 ml) and incubated at 37 ºC overnight with shaking at 200 rpm. An aliquot of *E. coli or S. aureus* o.n. culture, approximately 10^9 CFU/mL, was diluted 1:10 and 10 µl of the bacterial suspension was gently placed, under sterile conditions, onto the materials (S1, S2, S3, S4) and control. To permit bacterial adhesion on the material surface the samples were left to dry for one hour at room temperature and then placed into 0.3% crystal violet (CV) solution for 15 min to allow bacteria staining. To remove non/weakly adherent bacteria the stained samples were energetically rinsed in distilled water twice. Then, the samples were placed in 2 mL of pure ethanol, and vortexed for 5 min to solubilize CV. Particulate debris was removed by centrifugation at 14,500 rpm for 2 min, and the absorbance of the solution was measured using a UV−vis spectrometer at 590 nm. S1, S2, S3, S4 materials without bacteria were processed as described before and their absorbance, used as blank, was subtracted from the corresponding value of treated samples.

4.3. Results and discussion

4.3.1. The optimum composition of the blend and nanocomposite

To obtain the most stable blend and the following nanocomposite with good wetting properties, a systematic study was performed in order to understand the relationship between the polymers proportions, silica NPs concentration and final wetting properties. Initially, the best blend's composition was selected by fabrication of five different blends of PFA/ fluoroacrylic copolymer, namely as 90:10, 80:20, 70:30, 60:40 and 50:50 (PFA: fluoroacrylic copolymer ratio), followed by spray coating the solution on glass substrates. Measuring the wetting properties along with the

consideration of the proportion of bio-based polymer to fluoroacrylic copolymer, leads to select the PFA: PFAC blend with 50:50 ratio, which has the highest CAs with the less CAH among the blends (See Figure 35, a).

After the investigation of the blend's composition, different amounts of silica NPs were added into the 50:50 blend solution, to obtain the most superhydrophobic coating with the less-used silica NPs. Various nanocomposites with different concentrations of silica NPs ranging from 10 to 50 wt% respected to the weight of polymer were fabricated and the wetting properties were studied, Figure 35, b. Nanocomposite coating with 30wt% silica NPs, ensured the superhydrophobicity property along with showing the self-cleaning property by presenting the RAs around 4.3˚, so this nanocomposite was selected for furthur studies.

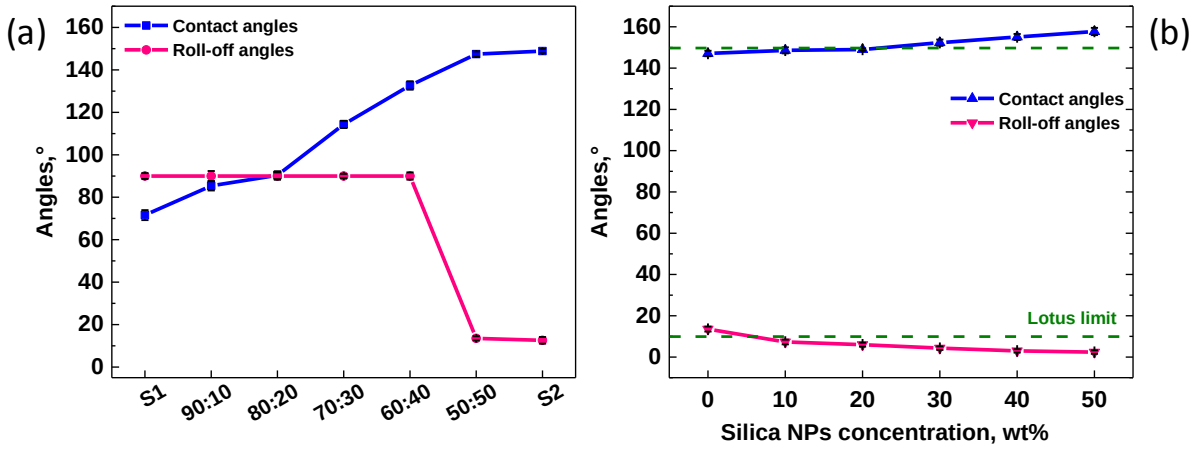

Figure 35. Comparison of static water CAs and related RAs (a) for different blend's composition, (b) for various nanocomposite coatings.

4.3.2. Chemical analysis

The chemical characterization of the samples S1, S2, S3 and S4 was carried out by ATR-FTIR spectroscopy and the results are shown in Figure 36. First, the materials were deposited onto the silicon wafer substrates and formed coatings were analysed. Main peaks of PFA were ascribed to OH stretching mode at 3406 cm^{-1}, CH stretching mode in aromatic rings at 3120 cm^{-1}, asymmetric and symmetric CH_2 stretching modes at 2922 cm^{-1} and 2870 cm^{-1}, respectively, C=O stretching mode attributed to the open furan ring at 1712 cm^{-1}, C=C stretching mode at 1602 cm^{-1}, ring vibrations at 1560 cm^{-1} and 1504 cm^{-1}, C−O−C stretching mode at 1149 cm^{-1}, C−OH stretching mode at 1011 cm^{-1}, and a specific absorption from 2,5-substitution of furan rings at 732 cm^{-1} [184,185]. On the other hand, for fluoroacrylic copolymer (S2 sample) the assigment was as follows: C=O stretching modes (asymmetric and symmetric) at 1732 cm^{-1} and 1668 cm^{-1} and C−O−C stretching modes attributed to

the ester functional group at 1186 cm^{-1}, respectively, perfluoromethylene (asymmetric and symmetric CF_2 stretching modes at 1234 cm^{-1} and 1139 cm^{-1}, respectively) functional groups [36,147].

The spectrum of the S3 sample prove that the main absorptions are related to PFA resin, while the absorption peaks of CF_2 stretching modes are also presented, which are ascribed to the fluoroacrylic copolymer. Due to the absence of frequency shifts in the blend's spectrum compared to the neat materials, it can be concluded that fluoroacrylic copolymer is chemically inert towards PFA and these two polymers create physical polymer blends, which is uniform in physical properties. However, the potentional numbers of H-bonding in the blend was diminished respected to the S1 sample, which is attributed to some modifications in the structure. The corresponding 30 wt% nanocomposite also exhibit the same absorption peaks associated to PFA and fluoroacrylic copolymer, while the Si–O–Si stretching mode attributes to silica NPs shows a broad peak around 1064 cm^{-1}, which covered all the peaks under this area (See Figure 36).

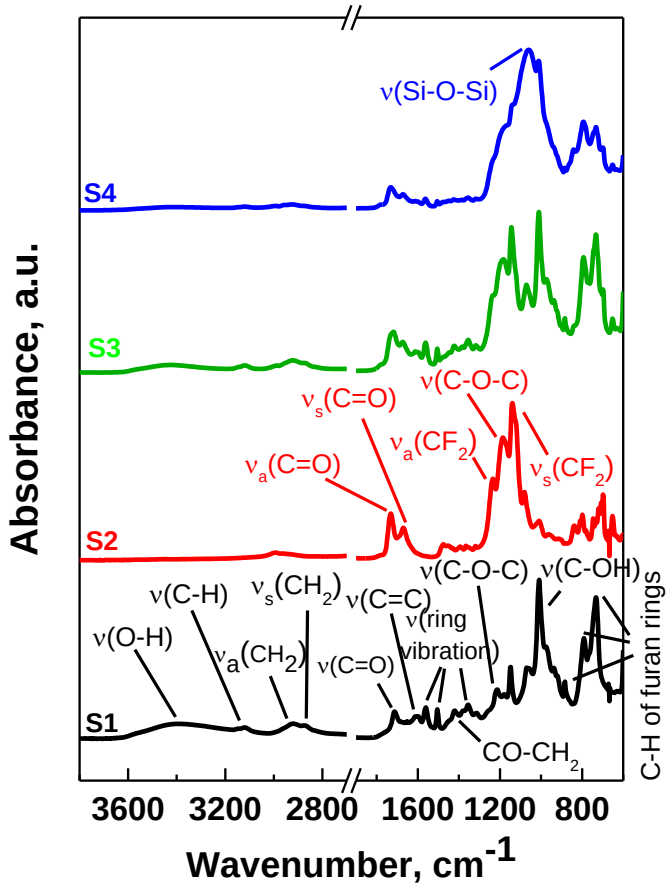

Figure 36. ATR-FTIR spectra of S1, S2, S3 and S4 samples.

In addition, the coatings were chemically characterized through XPS analysis to identify the surface composition of S3 and S4 samples and the obtained results are shown in Figure 37.

The high resolution C1s spectra was studied and the acquired spectra are shown in Figure 37, a and b. The C1s XPS spectra for these coatings indicates the chemical bonding of carbon with other elements on the surface such as C–F, C=O, C–O–C, C–C and C–H, which is confirmed the fluorinated surface for both samples with corresponding binding energy CF_2 (290.5 ± 0.1 eV) and CF_3 (292.6 ± 0.1 eV).

The obtained results from the main survey showed that for both S3 and S4 samples, the peaks at around 285 ± 0.2 eV, 532 ± 0.6 eV and 687 ± 0.6 eV are related to C 1s, O 1s and F 1s, respectively, which have the same position for both samples. However, due to the presence of silica NPs in the nanocomposite sample, a new peak at around 103.4 ± 0.2 eV is generated, which is ascribed to Si 2p. The lower F/C ratio along with higher O/C ratio could be attributed to the surface composition's modifications, which is a proof of the presence of SiO_2 NPs in the surface, that can contribute for superhydrophobicity effect.

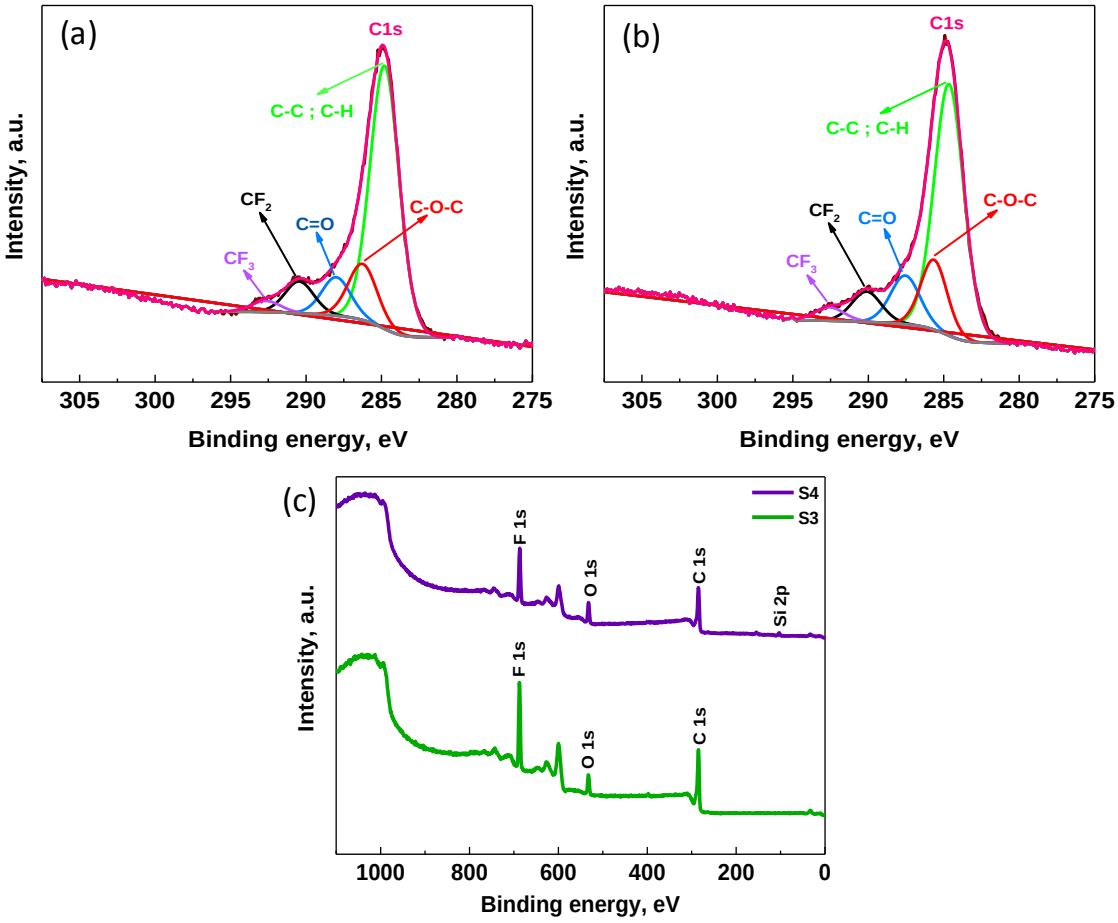

Figure 37. High resolution XPS spectra of C1s peak of (a) S3 and (b) S4 samples (Deconvoluted peaks are included). (c) Wide range XPs spectra of the S3 and S4 samples.

The wide spectra exhibits the relative atomic percentage of carbon, fluorine, oxygen and silica (for nanocomposite), which are summarized in Table 7.

Table 7. Elemental composition of S3 and S4 samples surface with atomic percentages.

Elements	S3	S4
C 1s	68.66	65.29
O 1s	7.61	10.40
F 1s	23.73	20.14
Si 2p	0	4.17

4.3.3. Morphological characterization

Scanning electron microscope images of the surface of spray coated neat PFA (S1 samples), pure PFAC (S2 sample), S3 and S4 coatings are shown in Figure 38. EDX images of an aluminium foil surface spray coated with the above solutions with showing Al (in green), C atoms (in red), F atoms in (in blue) and Si atoms (in purple) are indicated as inset in Figure 38. The image for S1 displays a very smooth surface morphology that a large area of aluminium substrate is out, due to the aggregation of PFA material after the evaporation of acetone. The SEM and the corresponding EDX image of S2 indicates that although a huge area of the substrate cannot cover by the polymer, but there are some rough strucrures on the surface, which prove the right selection of PFAC to be blended with PFA. The morphology of S3 sample of these two polymers shows a fully coverage of the substrate, which confirms the good film- formation property of the blend and also a good miscibility of the polymers with each other, as there is no separated area of F atoms in the image (which is attributed to PFAC portion). By introducing silica NPs into the blend (sample S4), the morphology display some changes in the hierarchical structures on the surface, as they turned to be more rough, which is neccessary for the final application of the coating. These changes could be ascribed to the presence of silica NPs in the upper surface of the coating, which is better visible in the EDX image that is covered by puple color of Si atoms. Due to the presence of Si atoms in the whole areas of the surface, it can be concluded that the silica NPs has a good dispersion in the blend matrix.

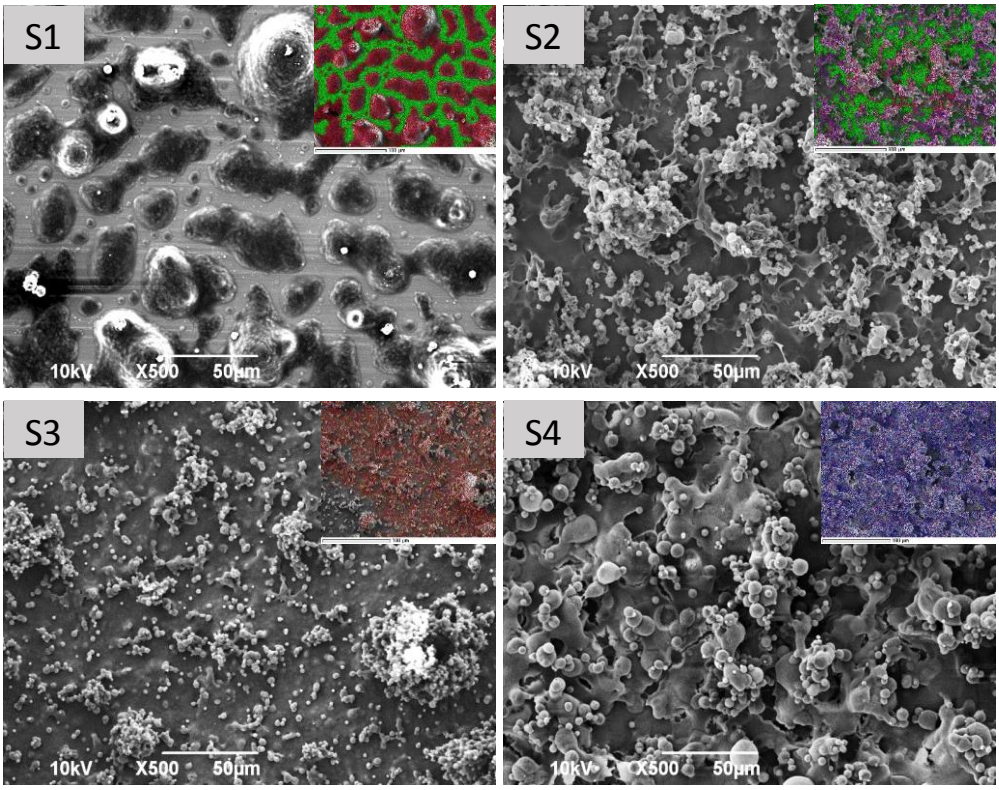

Figure 38. The SEM images of the surface of S1, S2, S3 and S4 samples.

To confirm the good miscibility of the polymers in acetone, an extra strudy was performed by drop casting of the blend solution on the aluminium substarte and observe it under SEM and EDX, and the images are shown in Figure 39. First, it's clear that the surface morphology of the spray coated and drop casted ones are compeletely different, due to the deposition method, which affects on the solvent evaporation rate. But along these differences, it can be seen that the dispersion of the F atoms in C atoms matrix is uniform, which is ascribed to the good miscibility of PFAC with PFA resin.

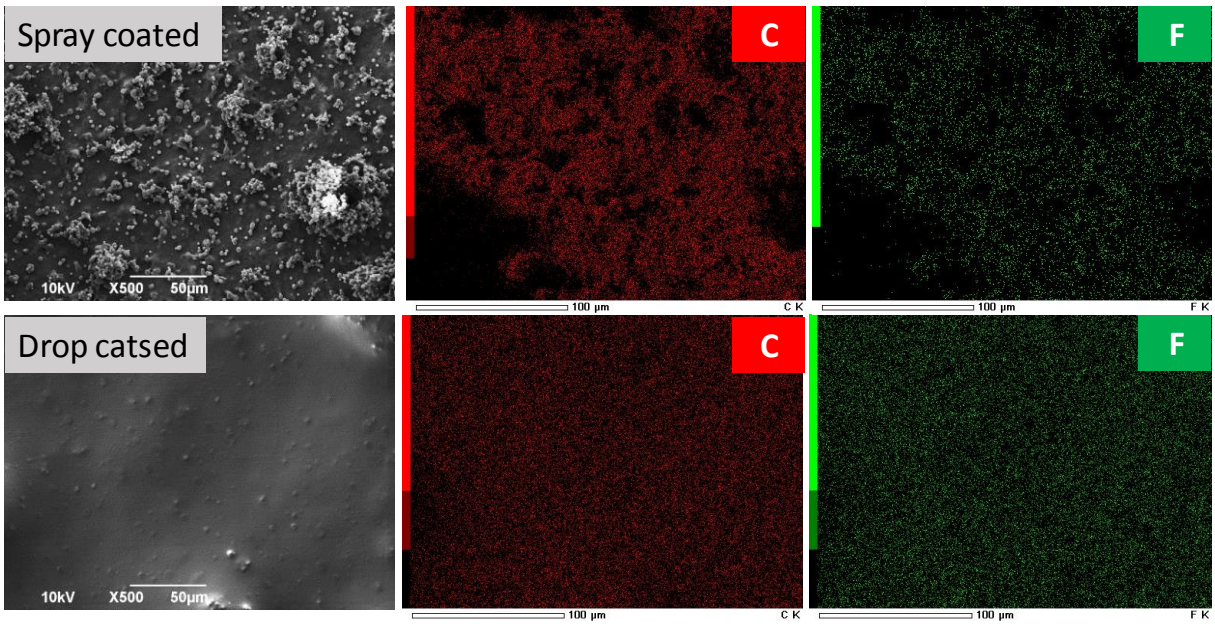

Figure 39. The SEM images of the blend spray coated (on top) versus drop casted ones (on bottom).

4.3.4. Wetting analysis

Different studies were done by analyzing the wetting properties of S3 and S4 coatings. Initially, the static CAs and the RAs of these samples were calculated by deposition of different kinds of liquids with various surface tensions and the results are shown in Figure 40, a and b. In the first glance, it can be seen that by introducing silica NPs into the blend matrix, the static CAs increased and the RAs decreased, compared to the S3, which is due to the creation of hierarchical micro and nano rough structures on the surface of the nanocomposite coating. Due to the perfluorinated structure of the acrylic copolymer along with the presence of hexamethyldisilazane or HMDS groups in silica NPs, the sufficient roughed surface with low surface energy is created, which causes a highly oleophobic-superhydrophobic coating [186]. The obtained results indicate a highly liquid- repellency for the 30 wt% nanocomposite coating with a superhydrophobicity (contatct angles > 150˚ with RAs <10˚) with a good oleophobicity (CAs > 130˚ with RAs < 15˚).

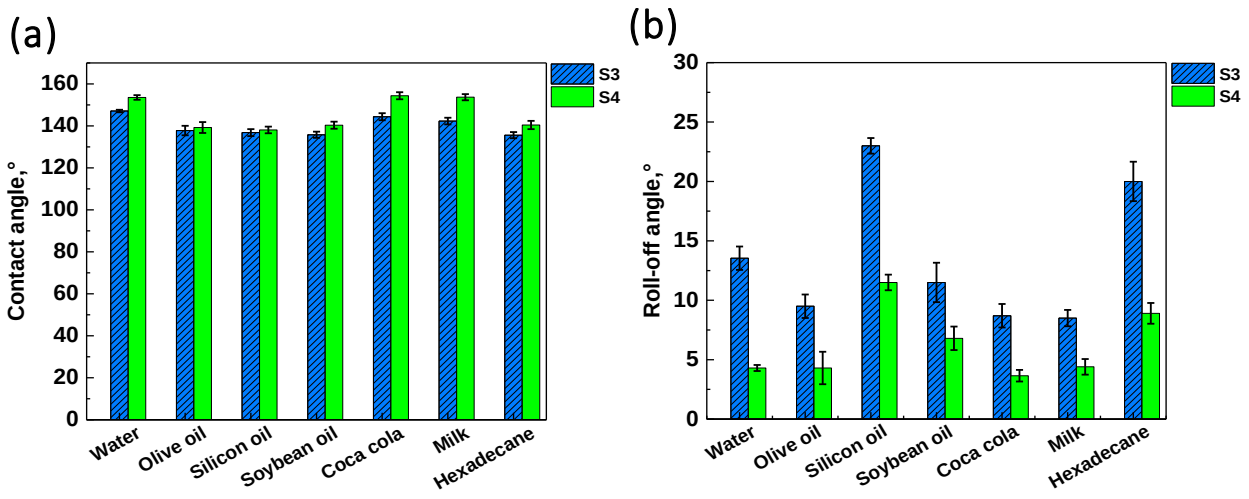

Figure 40. (a) Static CAs and (b) RAs of S3 and S4 samples by depositing different liquid droplets.

Another studies were performed in order to see the stability of the wetting properties of 30 wt% nanocomposite under various conditions. One of these studies was to understand the dependence of water RAs of S3 and S4 samples on the water droplet volume (See Figure 41). For this measurement, water droplets with different volumes ranging from 5 to 30 µL were deposited onto the surface and the RAs of the coatings were measured by tilting the surface stage. It is remarkable to see that even the PFA: PFAC blend, S3 coating has droplet mobility for 5 µL droplets and as the droplet volume increases, the difference in sliding or roll-off angles between S3 and S4 decrease and after 20 µL the

sliding angle limit goes below 5° for both coatings that is considered to be the criterion for self-cleaning superhydrophobicity.

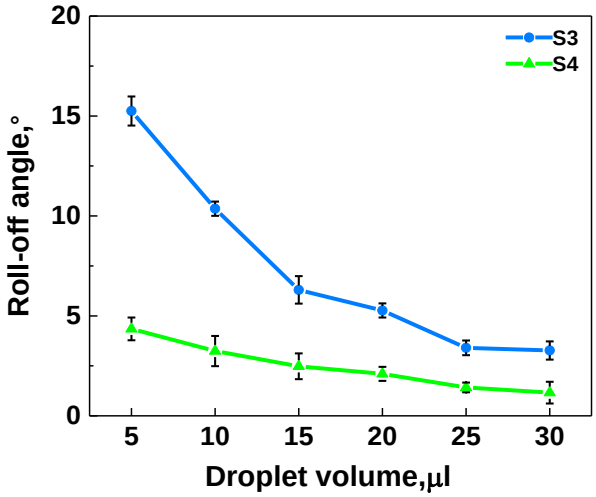

Figure 41. Dependence of RAs upon water droplet volume.

Another experiment was performed to investigate the stability of S3 and S4 coatings unto the higher temperatures, by thermal annealing of the coatings on the hotplate with different temperatures. However before these analysis, thermal behaviour of different samples were studied by using thermogravimetric analysis (TGA) and the mass loss curves and their derivatives are displayed in Figure 42. It can be seen that thermal stability of the blend improves by incorporation of PFAC into PFA resin, which is due to some modification in the structure followed by depletion of hydrogen bonds in the blend compared to the pure PFA, (as was explained in FTIR section). The first thermal degradation temperature of the blend in the presence of silica NPs (S4 sample) shifts to the higher temperatures and helped to sustain the weight loss around 45% even at 800˚C, confirming the good thermal stability of the final material. According to the curves, no significant weight loss observed for S3 and S4 samples before 200˚C. So the samples could be thermally annealed untill 200˚C without any thermal degradation, hence, the experimental temperatures were selected as 100˚, 150˚ and 200˚C on the hotplate for 1 hour.

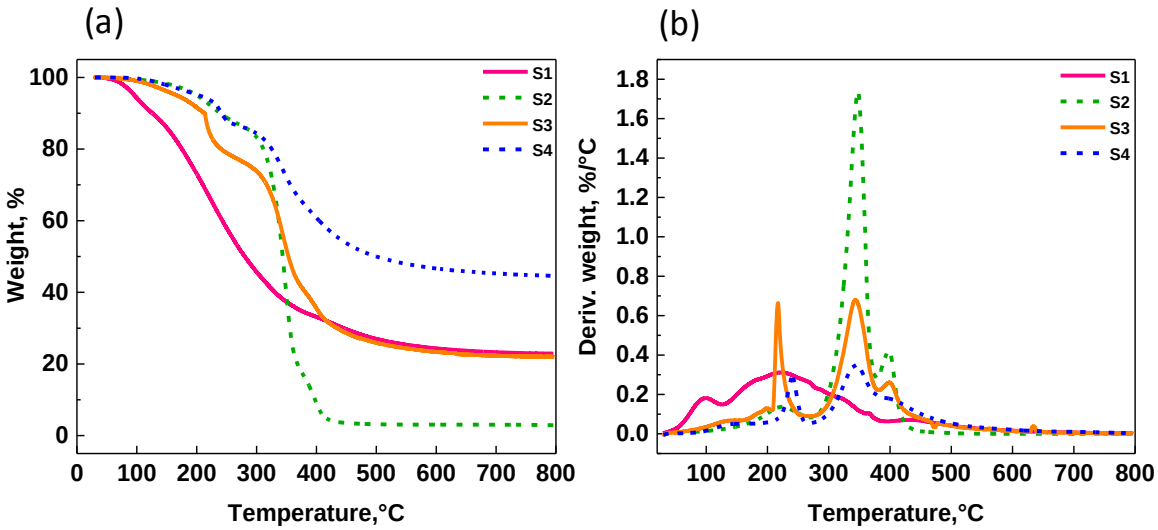

Figure 42. (a) Mass loss curves, (b) Derivatives of the thermograms of different samples.

After anneling the samples in the mentioned conditions, the wetting properties were measured again and the results are shown in Figure 43. The related graphs show that in general the CAs decreased as temperature increased, which it could be ascribed to the flattening of the surface. This is happening by melting the polymers followed by embedding of the upper layer into the lower ones, so the roughness of the surface diminished and CAs decreased. However, it would be interesting that for 30 wt% nanocomposite sample, for both deposition of water and oil droplets, the decreasing trend is not so considerable and this sample can keep it's hydrophobicity along with oleophobicity even up to 200˚C. While for the blend sample, the decreasing trend starts much earlier and also the slope of the depletion is too high and as far as, the annealed blend sample at 100˚C missed the oleophobicity completely. On the other hands, the water droplets and the oils ones cannot roll away on the blend surface after anneling at 150˚ and 100˚C, respectively. However, for the nanocomposite sample, the droplets can roll away completely, even after thermal anneling at 200˚C.

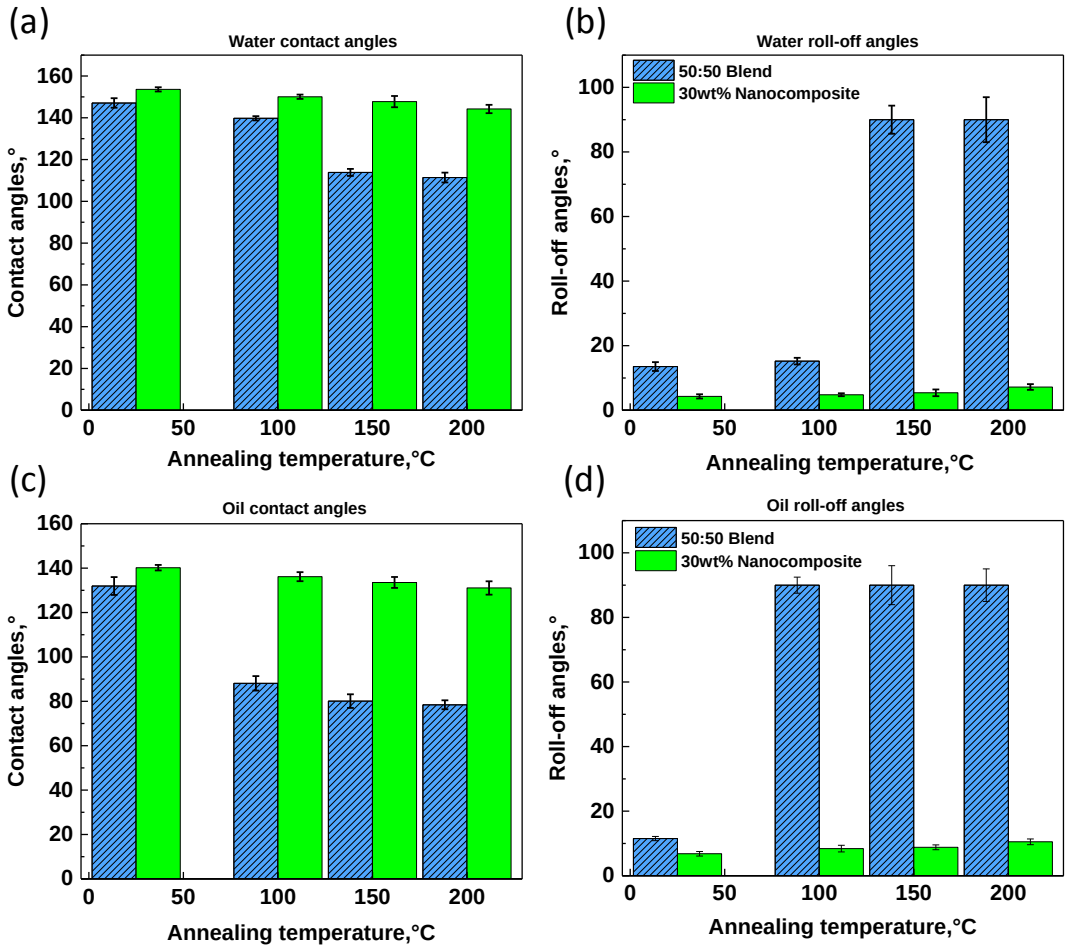

Figure 43. Stability of the wetting properties upon thermal annealing in different temperatures towards (a) and (b) water droplets and (c) and (d) oil droplets.

Observations will be confirmed by doing some SEM imaging of the samples after thermal annealing at different temperaturesc (See Figure 44). It's obvious that S3 sample (column a) starts to change the surface morphology during thermal anneling, but 30 wt% nanocomposite sample (column b) can keep the rough surface even at higher temperatures, which could be another witness for the good thermal stability of the nanocomposite.

So, it can be concluded that 30 wt% nanocomposite has a really good resistance towards high temperature, which opens some doors for the application of the coating in the high temperatures.

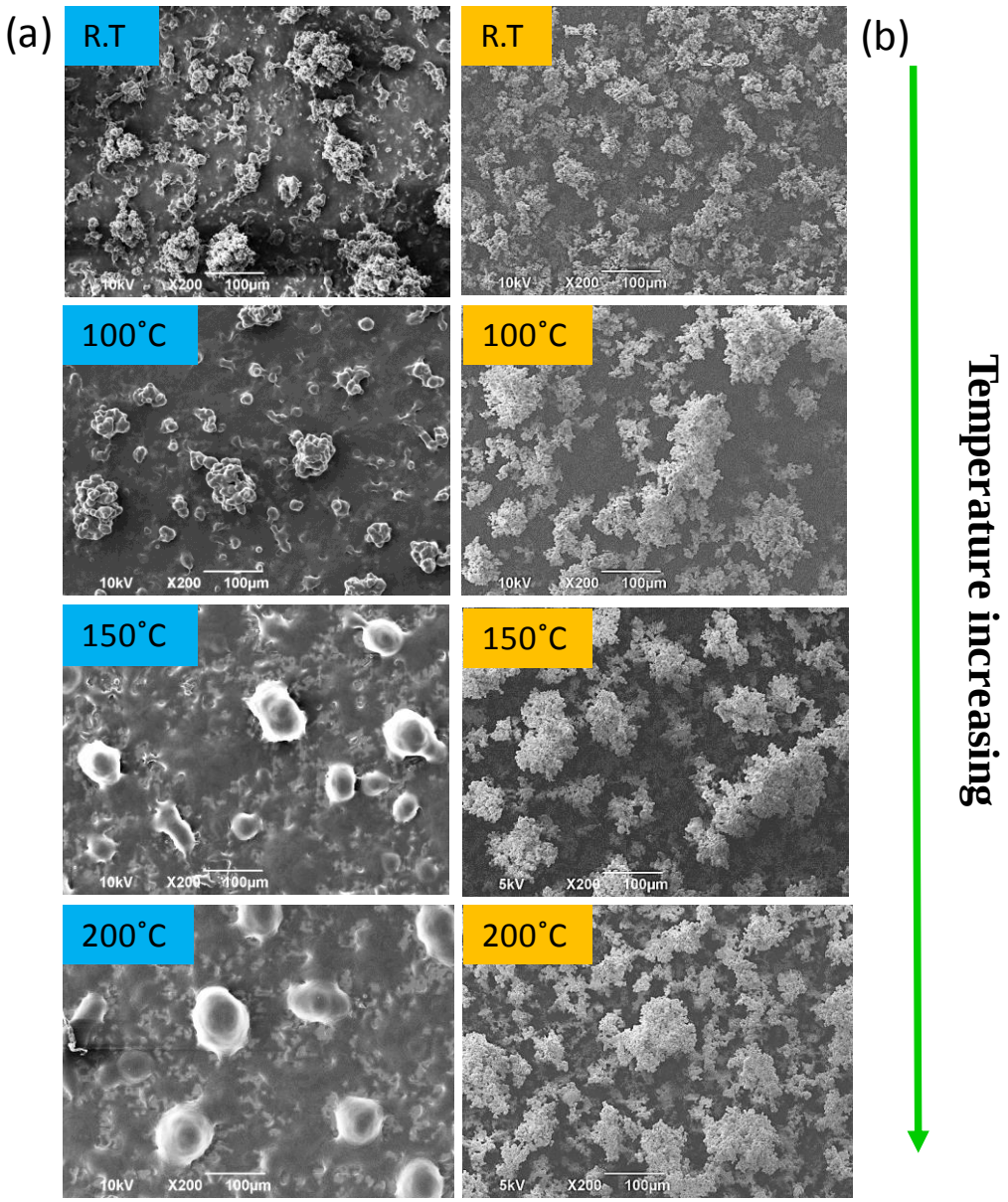

Figure 44. SEM images of S3 (column a) and S4 (column b) after thermal annealing at different temperatures.

Furthur studies on dureability of the coatings was performed by immersing S3 and S4 coatings in deionized water for 1, 2, 3, 4, 5 and 6 days in room temperature, followed by drying at room temperature and measuring the water and oil CAs (See Figure 45). The results for 30 wt% nanocomposite sample indicate that after 3 days immersion in water, the water and oil CAs do not show a big difference from the initial ones, which could be ascribed to the good trapping of silica NPs inside the polymer blends. The wetting properties start to deteriorate after 3 days, but still the water and oil CAs are higher than 90˚, so the nanocomposite sample can keep the liquid repellency property along with rolling away the droplets, even after 6 days. However, for S3 sample, the decreasing trend in the CAs happens earlier and this sample missed it's hydrophobicity and

oleophobicity after 3 days immersion in water and the droplets cannot roll away on the blend surface after this time. These results could be a strong evidence for the high stability of the nanocomposite coating, which confirms the good dispersion and embedding of silica NPs into the polymer matrix.

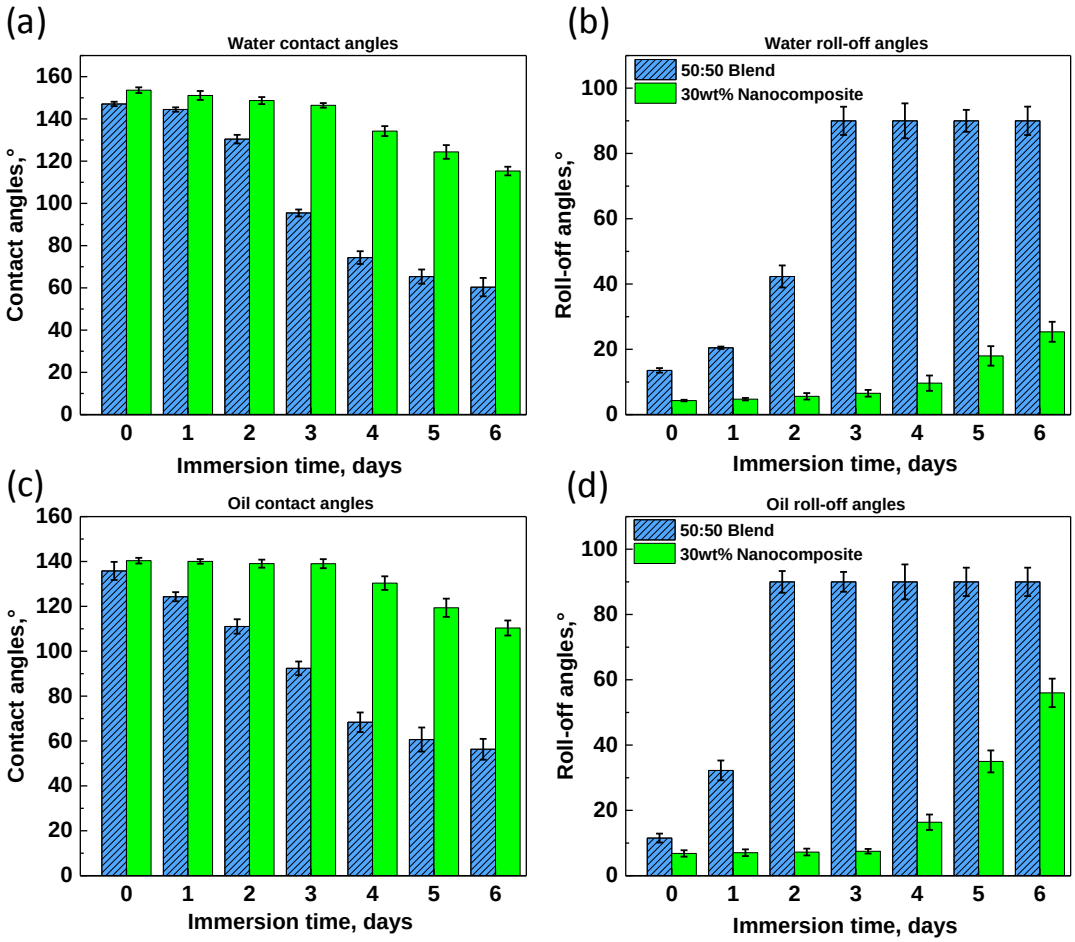

Figure 45. Durability of the wetting properties upon different immersion time in distilled water towards (a) and (b) water droplets and (c) and (d) oil droplets.

4.3.5. Roughness analysis

To study the topographical features of the surface, bare Al-foil and Al-foil coated with 50:50 blend and 30 wt% nanocomposite were selected to analyze by profilometer and the processed data are shown in Figure 46. 3D images (See Figure 46, a, c and e) of the surfaces indicate that bare substrate surface is almost flat (with average roughness value around 1.13 µm) without any characteristic features. However, by applying materials onto the substrate, the topography of the coated surface will completely changed. For S3 and S4 samples, the average roughness value were calculated around 5.02 and 9.87 µm, respectively. Higher values for the nanocomposite sample is due to the creation of some hierarchical structures on the surface in the presence of silica NPs. The surface topography profile of the samples are also displayed in Figure 46, b, d and f, which follow the above mentioned

trend. It can be seen that the peak-to-peak distance is getting smaller after addition of silica NPs into the polymer matrix, which could be related to the good dispersion of silica NPs and fabrication of much roughed surface respected to the blend sample.

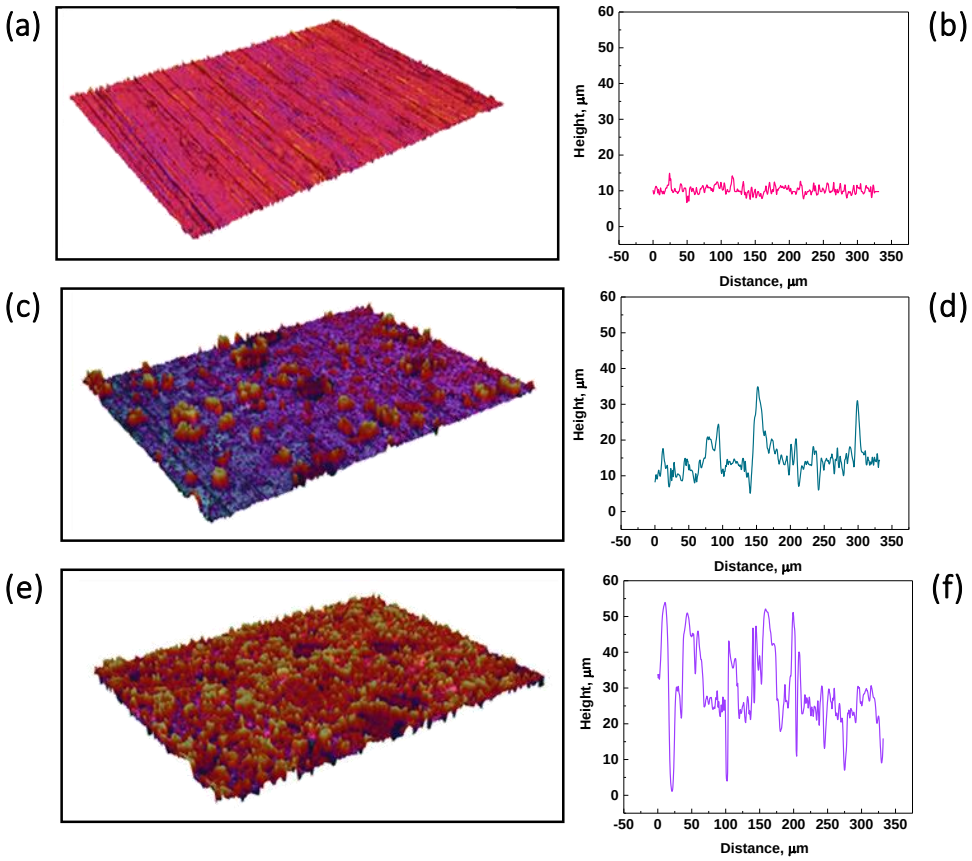

Figure 46. 3D optical images of (a) bare Al-foil, (c) Al-foil coated with 50:50 blend and (e) Al-foil coated with 30 wt% nanocomposite. 2D roughness profiles of (b) Al-foil, (d) Al-foil coated with 50:50 blend and (f) Al-foil coated with 30 wt% nanocomposite.

We also extracted two other surface roughness parameters known as skewness and kurtosis by using several images acquired from coatings S3 and S4. Skewness is sensitive to occasional deep valleys or high peaks. Zero skewness means symmetrical height distribution, while positive and negative skewness describe surfaces with high peaks and filled valleys, and with deep scratches and lack of peaks, respectively. On the other hand, kurtosis describes the probability density sharpness of the roughness profile. For surfaces with low peaks and low valleys, kurtosis becomes less than 3, and for surfaces with high peaks and low valleys it exceeds 3. In the case of S3 coatings, skewness and kurtosis values were estimated to be 2 and 8, respectively and for S4, 0 and 3, respectively [187,188]. This means that based on skewness numbers, S4 surface morphology features symmetrical distribution of micro-scale valleys and peaks, while S3 has many high peaks and filled valleys.

Kurtosis value of S4 is around 3 meaning that the surface roughness of S4 does not feature sharp peaks or valleys whereas S3 has many protruding peaks (See Figure 47).

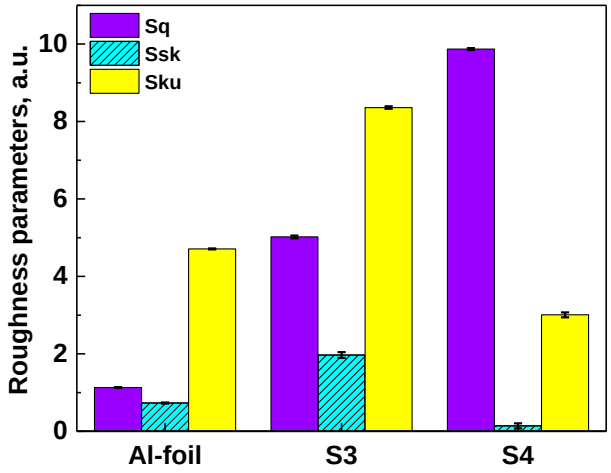

Figure 47. Comparison of different roughness values for the Al-foil, S3 and S4 samples.

4.3.6. Biocompatibility study

We carried out indirect toxicity tests to evaluate the biocompatibility of the produced films, also in view of their possible applications. Due to their hydrophobicity, the films are not suitable as substrates for cell adhesion and proliferation. We tested, however, if harmful substances were released from the films and if they could hinder or influence cell proliferation. We chose a robust and stable human cell line, e.g., HeLa cells, to conduct the tests. First, we conditioned a few mL of culture medium by submerging pieces of S3 and S4 films into DMEM for 48 hours. Subsequently, we used the conditioned DMEM for cell culture and we let cell growth until they were confluent. The results are displayed in Figure 48, a-c. HeLa cells grown, in the presence of conditioned DMEM (b, c) did not show morphological differences compared to HeLa cells grown in non-conditioned DMEM (a). We observed also that they reached confluency at the same time (2 days in culture, in the applied conditions).

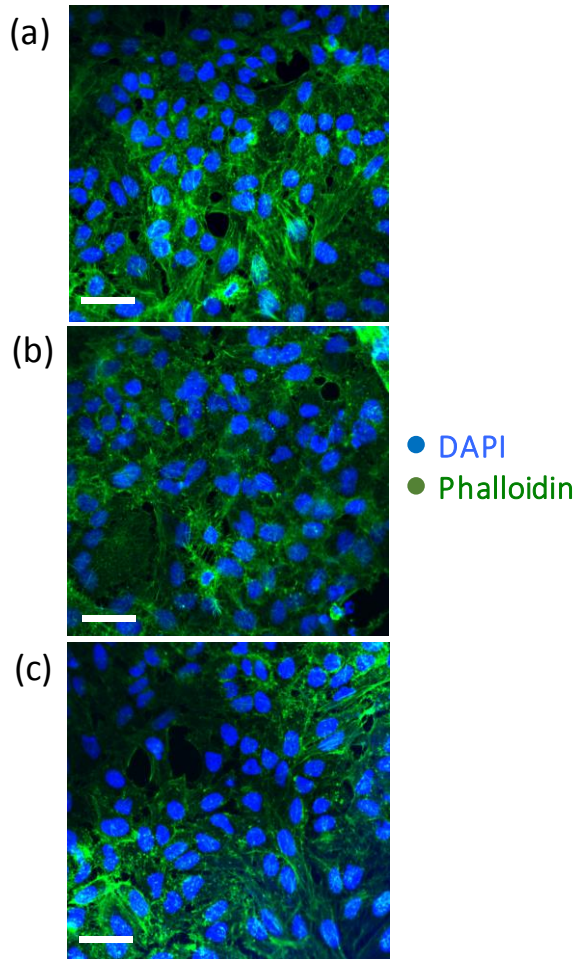

Figure 48. Confocal images of HeLa cells growing in normal DMEM (a) and in DMEM conditioned with S3 and S4 (b and c, respectively). Cells nuclei are labeled with DAPI (blue) and the cytoskeleton is labeled with Alexa-Fluor-488 Phalloidin (green). No harmful effect of the condinioned medium was detected: cells morphology is healthy and cells reach confluency at the same time, in all cases (The scale bars are showing 10 μ m).

To corroborate this finding, we carried out a real-time proliferation assay at a lower cell density and for a longer time (120 hours). In such a proliferation assay, cells are seeded onto gold electrodes; the impedance of the electrodes, read-out in real-time, is translated into a number, called cell index (C.I.), proportional to the area occupied by the cells. As shown in Figure 49, C.I. trends were identical in control (i.e., cells cultured in normal DMEM) and in the two samples cultured in conditioned DMEM, up to the 5th day in culture. We can therefore conclude that no harmful effect of the materials was detected.

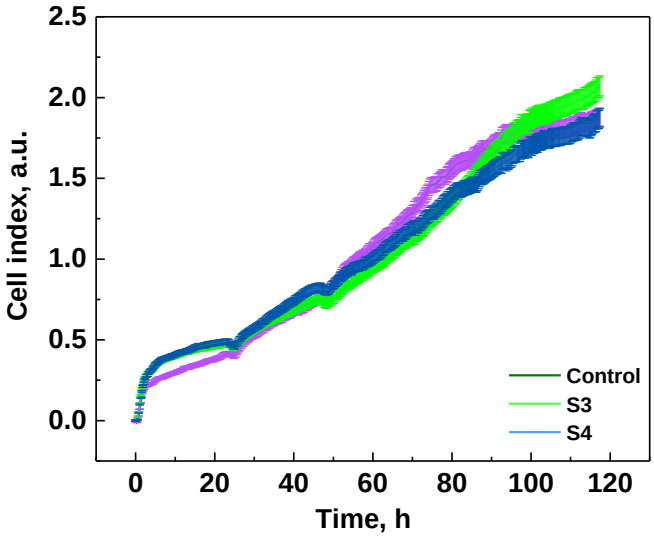

Figure 49. The real-time proliferation curves is displayed. The growth-rate is the same for the three samples: the C.I. trends are completely superimposed, within experimental uncertainty.

4.3.7. Bacterial adhesion study

E. coli and *S. aureus* were used for bacterial attachment assays. To compare bacteria attached to the samples, the same number of bacteria were spotted on the materials and glass and stained with CV. As shown in Figure 50, the glass samples had the main number of *E. coli* and *S. aureus* attached bacteria. The number of adherent bacteria to S1 and mainly to S2 and S3 was reduced compared to glass. Further, the CV staining on the S4 surface was negligible.

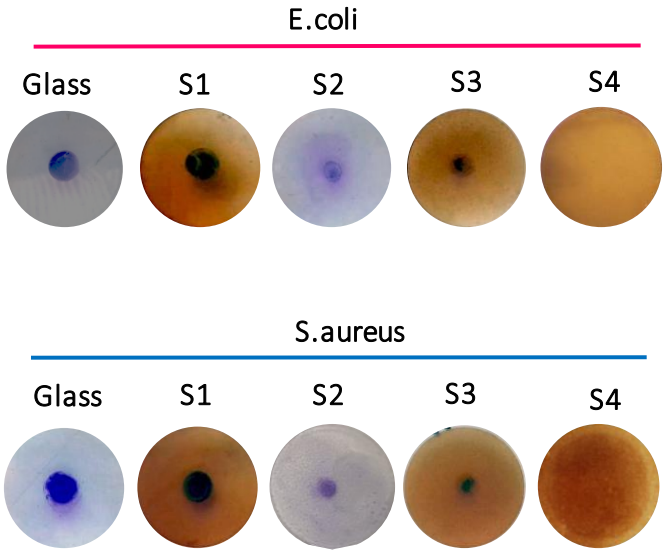

Figure 50. Comparison of E. coli and S. aureus bacterial attachment to S1, S2, S3, S4 and bare glass.

To confirm this data, the CV of each samples was solubilized in ethanol and the absorbance, proportional to the attached bacteria was measured at 590 nm and the results are shown in Figure 51. Both in *E. coli* and *S. aureus* bacterial adhesion, compared to the control, was 20-30 % less in S1, 60-75% lower in S2 and S3 and very slight in S4 indicating that this material showed the best anti-adhesion property with respect to the glass and S1, S2, S3 materials. This ability, probably due to the contact surface property, could prevent bacterial colonization.

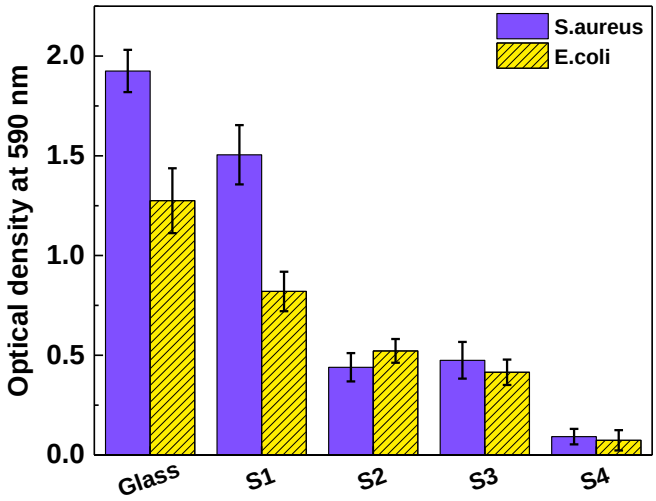

Figure 51. Bacterial absorbance of E. coli and S. aureus attached on S1, S2, S3, S4 and bare glass surface.

4.4. Conclusions

In this work, we fabricated a non-wetting coatings based on a bio-resin known as PFA, followed by blending with a waterborne perfluoroacrylic copolymer dispersion. To improve the liquid-repellency of the coating, silica NPs were dispersed directly into the blend solution. Due to the perfluorinated structure of the copolymer, the final coating shows superhydrophobicity along with high oleophobicity towards different liquids. Moreover, the nanocomposite coating displayed a high stability in the wetting properties respect to the high temeperature and immersion in water, which is due to the good miscibility and combination among the components in the nanocomposite matrix. In order to evaluate the relaese of the toxic materials to the environment, the samples were tested by putting them inside the medium containing cells and it was confirmed that the cells can grow in these medium, so the coating shows biocompatibility characteristics. Furthermore, the bacterials adhesion property were estimated by attaching the bacteria onto the coatings, followed by measuring the optical density of the samples in a certain wavelength. The nanocomposite sample indicates a really low bacterial adhesion.

Chapter 5

Thermally condcutive polymer coating decorated with in-situ synthesized silver nanoparticles and graphene nanoplatelets

5.1. Introduction

Particularly, the lightning strike causes huge damages all over the world, especially in the transportation industry field; it is a repeated challenge that happened annually [189]. In the event of a lightning strike on an aircraft or a vehicle, a substantial amount of thermal (or electrical) energy is delivered in milliseconds and if not given a safe way out, it can vaporize the metal structures or can cause serious damage to other electronic components [190,191]. In contrast, when the surface is protected with lightning strike coatings having ultrahigh *in-plane* thermal conductivity (≥ 1000 W/m K), the energy coming from the clouds can reach these coated materials and quickly spreads parallel to the surface (*x*-axis direction). Therefore, the energy spike is reduced and so is the damage [192]. Previously, woven metallic meshes (Cu, Ag or Al) were used for such applications, however, it adds significant cost, material weight and loss of fuel economy to the transportation industry [192,193]. Therefore, alternative solutions with equal or improved performance, low weight/cost, and high corrosion resistance are always desired to meet the current challenges of the transportation industry.

Although intrinsically insulting polymer films are incapable of dissipating huge amount of thermal energy in the event of lightning strike, these materials are regarded as suitable matrices for protective coatings and thermal management [194,195]. A common trend to enhance the thermal conductivity of the polymer matrices is to incorporate nanofillers with ultra-high thermal conductivities, such as carbon nanostructures [196–198], metallic particles [195,199] and ceramic fillers [200,201]. Among all the metallic materials, silver nanoparticles (Ag NPs) display the highest thermal conductivity (≈ 430 W/mK) and attract huge attention of researchers [202,203]. Although many synthesis routes are available for Ag NPs, the best method to have a highly dispersed Ag NPs inside the polymer matrix is an *in-situ* synthesis of the nanoparticles directly inside the polymer solution [195,204–206]. For this, several inexpensive chemical precursors can be used to synthesis Ag NPs through chemical and physical reduction of silver slats[207–211]. Nevertheless, due to the zero-dimensional morphology and small size of these nanoparticles, they cannot fabricate an effective pathway in the polymer matrix for good heat conduction. To achieve high thermal conductivity (*in-plane* or *out-of-plane*), either large quantities of the Ag NPs are used [203,212], which leads to change in material cost and mechanical properties, or other high aspect ratio fillers are mixed in proper quantities to achieve percolation threshold at low mass loadings [195,213]. Usually, carbon-based nanomaterials including carbon nanofibers (CnFs) [214,215], carbon nanotubes (CNTs) [190,191,216,217] and graphene [218,219] are more famous for this purpose, however, these carbon-based nanomaterials are regarded as an expensive alternative to metallic meshes [193]. On the other hand, graphene nanoplatelets

(GnPs) with the number of layers more than 6, which has a special structure and low cost (1.0-2.0 $/gram) along with intrinsic high thermal conductivity ($k \approx 3000$ W/mK) can be an effective choice [220,221]. Thanks to the unique morphology of the GnPs, this material has a high aspect ratio, which can be effective to fabricate an interconnected network inside the polymer matrix [198,222].

Herein, we demonstrate that the presence of in-situ synthesized Ag NPs and GnPs in hybrid form in the acrylic copolymer matrix can improve the thermal conductivity of the final nanocomposite. Direct in-situ synthesize of Ag NPs into the polymer matrix can promote the efficiency and miscibility of nanoparticles with the polymer matrix. The nanoparticles were formed by chemical reduction of silver trifluoromethanesulfonate in the presence of sodium hydroxide as a reducing agent. This process can be easily adapted to an industrial scale, as it does not include any toxic ingredient. On the other hand, GnPs with high aspect ratio, besides these synthesized Ag NPs can make a fully interconnected network inside the polymer matrix, which is necessary for thermal conductivity. The prepared Ag NPs/GnPs/acrylic adhesive based nanocomposite with high *in-plane* thermal conductivity have potential application in lightning strike protective coatings in ordinary vehicles and aircraft.

5.2. Experimental section

5.2.1. Materials

A commercial acrylic copolymer, AC403 SIGIL ONE, Solyplast, Pattex, with 60 wt% initial solid content was purchased from Henkel. It has good adhesion to many substrates such as wood, glass, painted surfaces, metals, ceramics, cement, and plastics. $AgCF_3SO_3$ (Silver trifluoromethanesulfonate or silver triflate ≥ 99%), sodium hydroxide and isopropanol were purchased from Sigma-Aldrich. Graphene nanoplatelets (GnPs) with a typical thickness of 6–8 nm, lateral size of 5 microns was purchased from Strem Chemicals and used as received.

5.2.2. Preparation of the samples

The acrylic copolymer/ Ag NPs nanocomposites were prepared via *in-situ* synthesis of Ag NPs, starting from adding 0.1 wt% concentrated silver triflate solution in isopropanol, into 16.5 wt% acrylic copolymer solution in isopropanol. The Ag NPs start to form after adding a few drops of sodium hydroxide as a reducing agent to transform Ag^+ to Ag^0. By the time and gently mixing, the production of nanoparticles was completed. To fabricate the final nanocomposites, different quantities of GnPs were also included to the acrylic/Ag NPs nanocomposite, followed by probe sonic processing (SONICS, Vibra cell, USA) for 1 min and 2 h in ultrasonic bath at 59 Hz (SAVATEC, Strumenti scientific, LCD series, Italy) to certify the good dispersion of nanofillers in the polymer matrix. Afterward, the nanocomposite solution can be directly solution-casted in Teflon Petri dishes or even spray-coated on a substrate like Al foil to be characterized (see Figure 52).

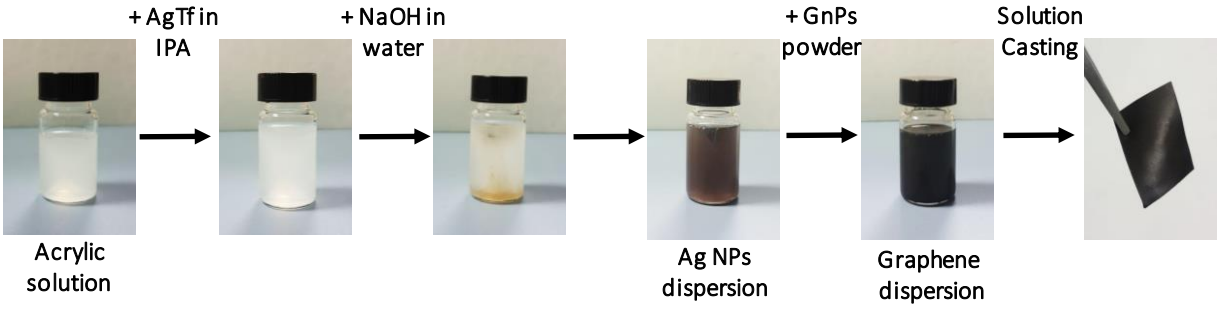

Figure 52. Step-by-step fabrication process of the Ag NPs and GnPs hybrid nanocomposites.

Table 8 shows different types of samples with their formulations, which were prepared during this work to make a comprehensive study.

Table 8. Different composite samples with their identifications (codes) and compositions.

Sample code	Polymer (5 g each)	Ag NPs (wt%)	GnPs (wt%)
S1	Acrylic copolymer	-	-
S2	Acrylic copolymer	0.2	-
S3	Acrylic copolymer	-	5
S4	Acrylic copolymer	-	10
S5	Acrylic copolymer	0.2	5
S6	Acrylic copolymer	0.2	10

5.2.3. UV-visible spectroscopy

UV-vis spectroscopy was used to verify the formation of Ag NPs in the polymer solution. For this, different solution was analyzed with Varian Cary spectrophotometer 6000i at different times of the reaction. The experiments were performed using UV-VIS-NIR light source in the range from 300-800 nm at 25˚C. The presence of Ag NPs in the solution was defined by their characteristic plasmon peak at about 400- 450 nm [223–225].

5.2.4. Transmission electron microscopy (TEM)

The final formation of Ag NPs in the polymer matrix and the average size of these synthesized particles were acquired by Transmission electron microscopy (TEM) using a JEOL JEM-1011 microscope under an accelerating voltage of 100 kV. The solution was deposited onto a carbon-coated copper TEM grid by drop casting and dried under light vacuum before imaging.

5.2.5. Fourier transform infrared spectra (FTIR) measurements

Infrared spectra were collected using an ATR accessory (MIRacle ATR, PIKE Technologies) coupled to a Fourier Transform Infrared (FTIR) spectrometer (Equinox 70 FTIR, Bruker). All spectra were obtained in the range from 3800 to 600 cm^{-1} with a resolution of 4 cm^{-1}, accumulating 128 scans. More than three spectra were collected for each sample to overcome any uncertainty.

5.2.6. High resolution scanning electron microscopy (HRSEM)

The morphology of the fabricated coatings was characterized by HRSEM using a JEOL JSM-7500LA (JEOL, Tokyo, Japan) equipped with a cold field-emission gun (FEG), operating at 10 kV acceleration voltage. The samples for SEM imaging were sputter-coated with a 10 nm carbon layer, in order to reduce charging effects. Energy-dispersive spectroscopy (EDS, Oxford instrument, X-Max, 80 mm2) was utilized to distinguish the presence and distribution of Ag in the nanocomposites. All experiments were done at 10 mm working distance, 8 kV acceleration voltage and 15 sweep count for each sample.

5.2.7. Thermogravimetric analysis (TGA)

Thermogravimetric analysis (TGA) was performed for certain samples with a TGA Q500 (TAInstruments, USA). For this, about 5 mg of different samples in platinum pans were measured in the range of 30 to 800˚C with a heating rate of 10˚C. N_2 environment was utilized during all the measurements at a flux rate of 50 mL/min.

5.2.8. Electrical conductivity

Electrical properties or sheet resistance of the prepared samples were measured by a digital voltmeter (ISO-TECH IDM71). For this, Square samples of 5 × 5 mm^2 sheet area were prepared and fixed by double stick adhesive tape onto glass slides. Silver paste (SPI conductive silver paint, resistivity ≈ 0.01 Ω/□) electrodes of 5.0 × 2.5 mm^2 size were painted on the conductive surfaces 5 mm apart [226,227].

5.2.9. Thermal conductivity

2-dimensional (*in-plane*) heat transfer of different nanocomposites or nanocoatings was evaluated by using an infrared (IR) camera with ± 2 ˚C accuracy (A315 FLIR, UK). In order to measure the thermal conductivity of the materials, the final solution was solution-casted in Teflon Petri dishes and completely air-dried. The films were peeled-off from Petri dishes with 35 µm and were cut into 5 cm × 3 cm rectangular pieces. The backside of the samples was insulated with a thick Teflon plate by adhesive bonding, to avoid the convection loses to the air. The samples were attached to a constant temperature (150˚C) source at one edge, followed by recording the temperature propagation along the *x*-direction. Once the samples reached to the steady state condition, the average temperature of the films is evaluated with standard deviations in different distances from the hotplate, namely as x = 0 cm, 1 cm, 2 cm, 3 cm, 4 cm, and 5 cm. The distribution of temperature or surface heat transfer of a thin material with different thermal conductivities (k = 100 – 2000 W/m.K) was also calculated by a theoretical model as it is discussed in section 3.5. Afterward, theoretical temperature distribution profiles were compared with the experimental ones and hence, the *in-plane* thermal conductivity of the prepared nanocoatings were estimated by this model.

5.3. Results and discussion

5.3.1. Characteristics of in-situ synthesized Ag NPs in the polymer matrix

Ag NPs are simply formed by reduction of Ag^+ in silver salts in the presence of reducing agents, such as sodium citrate, $NaBH_4$, hydroquinone, etc. [228]. Here, Ag NPs were successfully synthesized from AgTf in acrylic solution, by adding a few drops of sodium hydroxide as a reducing agent, which transformed Ag^+ to Ag^0. With the addition of sodium hydroxide and over the time, the color of the solution starts to change from light yellow to brown as shown in Figure 53. To prove the formation of Ag NPs in the polymer matrix, UV-vis absorption spectroscopy was performed during the time. UV-vis spectra displayed an absorption peak at around 400-450 nm, indicates the characteristic Surface Plasmon Resonance (SPR) peak for Ag NPs, which is in agreement with the other studies [224,229]. Once, sodium hydroxide was added to the solution, this peak begins to appear, by the time and gently mixing of the solution, the Plasmon peak intensity becomes stronger as shown in Figure 53. This can be attributed to the larger number of nanoparticles, which formed in the solution during the time.

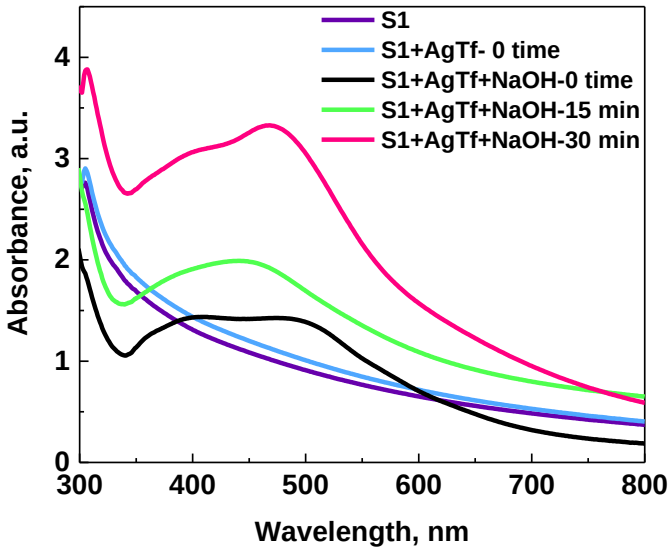

Figure 53. UV-vis spectra of Ag NPs preparation process at different reaction times.

The morphology of the obtained Ag NPs can be analyzed using TEM and HRSEM, where shape, size and distribution could be simply distinguished (See Figure 54). The TEM image of such synthesized nanoparticles in the polymer matrix is displayed in Figure 54, a, which shows an interesting conformation of Ag NPs/polymer nanocomposite and it is possible to visualize the spherical shaped Ag NPs in the polymer matrix with the size ranging from 5 to 30 nm. However, it is seen that these nanoparticles are not well connected, which is important for the final application of the nanocomposite. Figure 54, b and c shows the HRSEM image and EDX analysis of such Ag NPs in the polymer matrix, respectively, to prove the presence of nanoparticles and to show the distribution of nanoparticles inside the polymer matrix. It can be seen in both TEM and HRSEM images that the synthesized nanoparticles are surrounded by the polymer matrix, which confirms good miscibility of the synthesized nanoparticles with the polymer matrix.

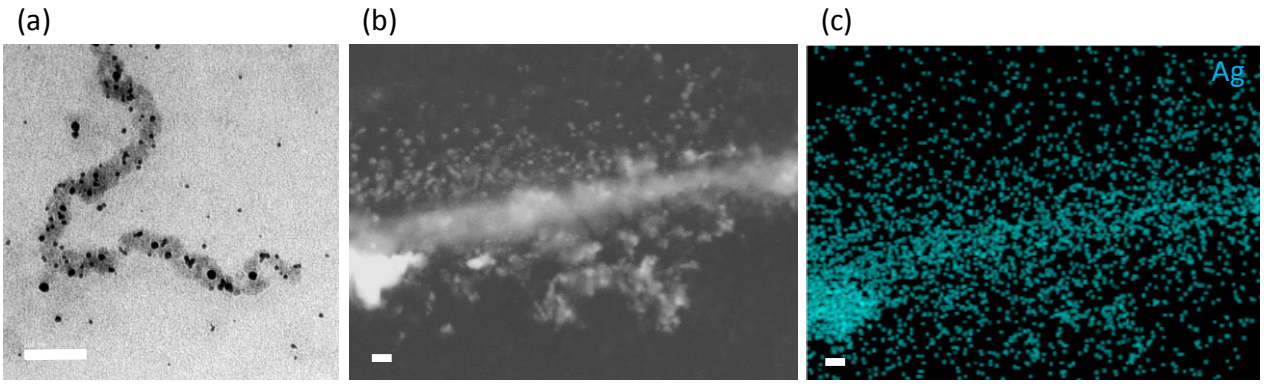

Figure 54. (a) TEM micrograph of the Ag NPs/acrylic copolymer nanocomposite. (b) HRSEM image of the Ag NPs in the polymer matrix. (c) The corresponding EDX map, showing the presence of in-situ synthesized Ag NPs (Scale bars correspond to 100 nm).

5.3.2. Chemical characterization

The prepared nanocomposites were further characterized for their chemical compositions and molecular interactions using FTIR spectroscopy. For this, pristine acrylic copolymer (sample S1), acrylic copolymer with Ag NPs (sample S2) and GnPs (sample S3), and their hybrid nanocomposite (sample S5) were selected for the FTIR analysis. Figure 55 shows FTIR spectra of S1, S2, S3, and S5 samples. Such as the pristine acrylic copolymer film (sample S1) demonstrate a characteristic broad peak at 2800-3100 cm^{-1} associated to the typical intermolecular hydrogen bonding [230,231]. Moreover, as shown in Figure 55, the carboxylic region of the acrylic structure displays an intense peak at 1728 cm^{-1} corresponding to stretching vibration of C=O group. Similarly, some additional peaks at 1451 cm^{-1}, 1161 cm^{-1} and 762 cm^{-1} are associated with CH_2 scissoring, stretching vibration of C-O group and rocking of CH_2, respectively [230,232]. These FTIR signatures of the carboxylic and hydroxyl regions were also present in the other prepared samples. However, after incorporating Ag NPs (sample S2) an additional peak at about 1572 cm^{-1} is observed. This relatively less intense peak may be attributed to the silver-acrylate asymmetric stretching or a complex formation between carboxylic group and Ag NPs. Some other researchers also indicated a similar interaction between the carboxylic group of the polyacrylic acid and *in-site* synthesized Ag NPs [230,231,233]. In contrast, GnPs inclusion did not show any contribution to the FTIR spectra as seen in Figure 55.

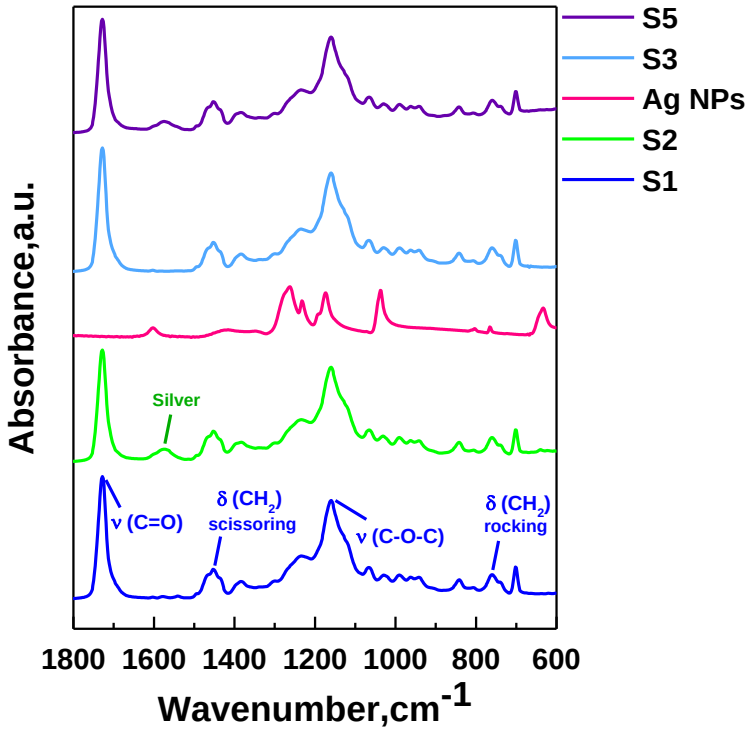

Figure 55. ATR-FTIR spectra of the S1 in blue, S2 in green, Ag NPs in pink, S3 in light blue and S5 in purple in the range of 1800-600 cm^{-1} region, to see the differences better.

To analyze the chemical structure and presence of the GnPs in the samples, samples namely as S1, S2, S3 and S5 were studied with XRD and the obtained diffractograms are shown in Figure 56. In the diffractogram of all the samples, one peak related to the copolymer at around $2\theta = 18^{\circ}$ can be seen, while the area under the peak is different. For pure acrylic copolymer (sample S1), there is another peak centered at $2\theta = 8.5^{\circ}$ and the crystallinity was calculated around 59% according to the two phase model and the following equation (equation 4) [234,235]:

$$\%Crystallinity = \frac{A(cryst)}{A(cryst) + A(am)} \times 100 \qquad \textbf{Equation 4}$$

On the other hand, due to the formation of Ag NPs and introducing the GnPs into the polymer matrix, some rearrangements can occur in the chemical structure of the copolymer, such as disappearing the peak at $2\theta = 8.5^{\circ}$. Distribution of the synthesized Ag NPs in the polymer matrix causes some interruption in the polymer crystals formation and decrease the crystallinity to 51% in sample S2. However, by addition of GnPs into the polymer matrix, the crystallinity increased, considerably to

91% and 86% in S3 and S5 samples, respectively. According to the Bragg's law, the creation of the sharp peak at around 2θ = 26.5˚, can be assigned to the high crystallinity of GnPs (002) and corresponded to the interlayer spacing of 0.34 nm [236–238]. This could be attributed to the high aspect ratio of the nanoplatelets, which can act as nucleating agents for polymer chains and increase the crystallinity [239–241]. Moreover, the small peak at around 2θ = 54˚ in the XRD patterns of S3 and S5 corresponds to the graphitic planes (004) with interlayer spacing around 1.673 nm, which indicates that GnPs are not completely exfoliated in the polymer matrix [242], which is further discussed in the TEM analysis of the final nanocomposite (S5 sample).

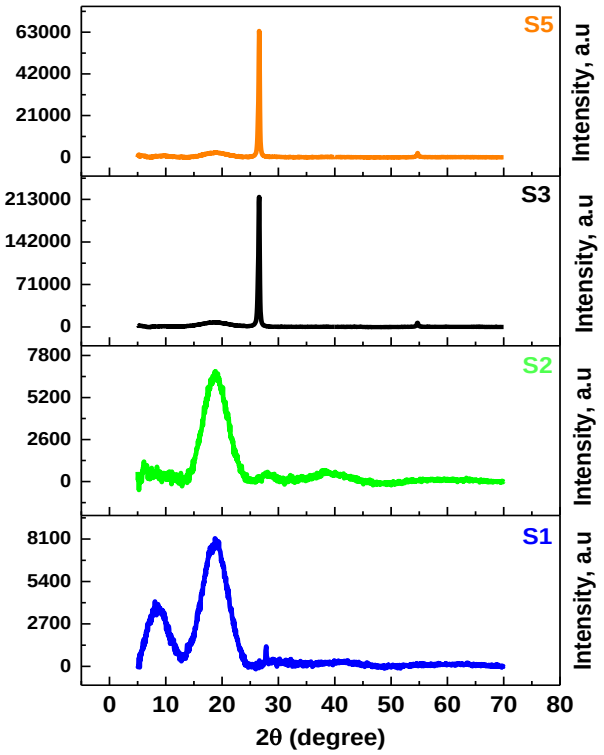

Figure 56. XRD diffractograms of the selected samples namely as S1, S2, S3, and S5.

5.3.3. Morphological characterization

To study the morphology of the samples and the dispersion of both GnPs and the in-situ synthesized Ag NPs in the polymer matrix, which are the main parameters for good efficiency of the composite, HRSEM is done for some selected samples, S1, S2, S3 and S5, and the related images are displayed in Figure 57. The film formation of acrylic copolymer, S1 sample, shows a quite smooth surface, without any characteristic features on it, Figure 56a. After the synthesis of Ag NPs in the polymer matrix, S2 sample, the morphology of the surface changed a little bit due to the presence of some small aggregation of Ag NPs in the surface, but still, the surface was considered smooth. However,

introducing GnPs into the polymer matrix causes some obvious differences respected to the two previous ones (Figure 57, c and d), which could be related to the in-plane and out of plane arrangements of the GnPs on the surface. By comparison of Figure 57, b and d, it can be seen that the dispersion of Ag NPs in the presence of GnPs looks better. Moreover, the size of the Ag aggregates is also smaller in the sample S5 as compared to sample S2. Due to the unique morphology and high aspect ratio of the GnPs, this nanomaterial can help Ag NPs to have a better dispersion in the polymer matrix and both of them can make a fully interconnected network inside the polymer matrix, which is important for the good performance of the nanocomposite in thermal conductivity [243,244].

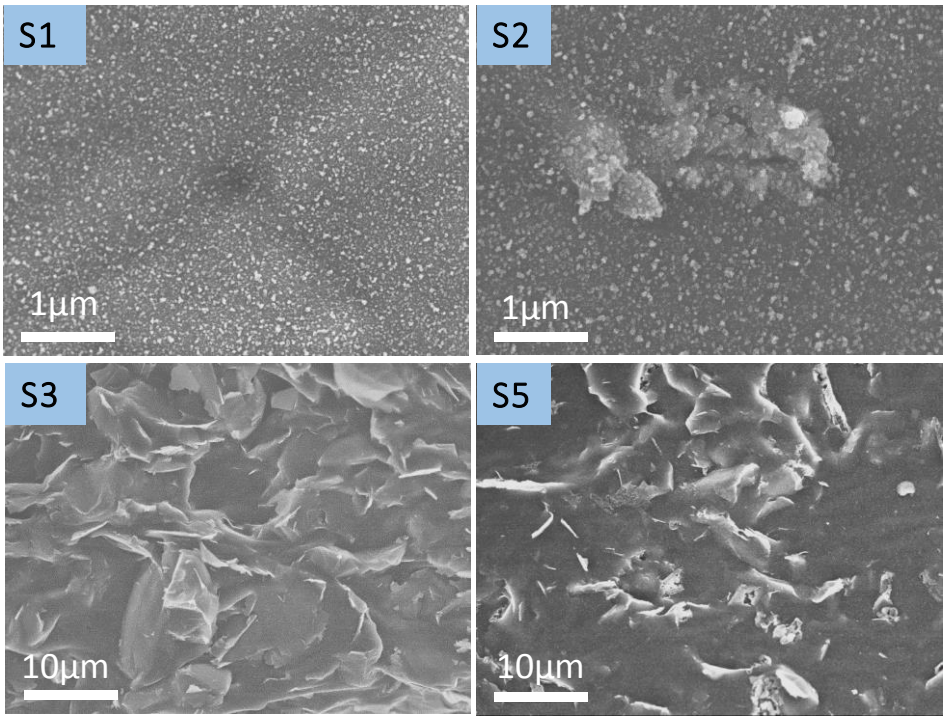

Figure 57. HRSEM images of the surfaces of samples S1, S2, S3 and S5.

For better observation of the nanofiller's distribution in the polymer matrix, TEM analysis of the sample S5 was done, and the result is shown in Figure 58. It can be seen that GnPs are dispersed in the polymer matrix in some small colonies consist of a few numbers of nanoplatelets, which are interconnected and it's the key point for the final application of the nanocomposite. On the other hand, in the presence of GnPs, Ag NPs has this opportunity to avoid the aggregation and disperse better in the polymer matrix and help to make an interconnected network.

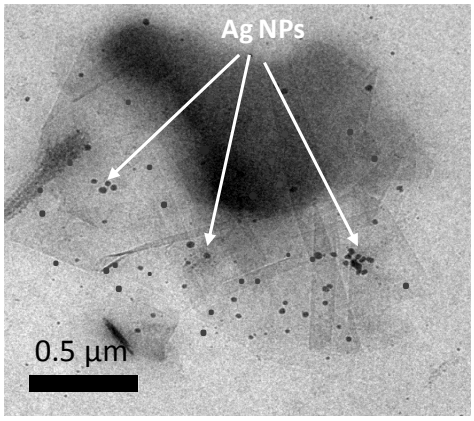

Figure 58. TEM image of the distribution of Ag NPs and GnPs in S5 sample (Scale bar corresponds 0.5µm).

5.3.4. Thermogravimetric analysis

Thermogravimetric analysis was performed to understand the thermal properties of the samples and relative mass loss of the samples versus temperature and the corresponding first derivative curve of it (DTGA) are shown in Figure 59. It is clear that the thermal behavior of the samples contain Ag NPs is different from pure copolymer and the sample only with GnPs (S3 sample). For S1 and S3, the degradation occurs in 3 steps, while for the others happens in 4 phases. This difference could be related to the silver-acrylate interaction and some rearrangements in the chemical structure in samples S2 and S5, which add one more step to the degradation process of these samples.

The onset of the thermal degradation starts at around 280˚C, however by in-site synthesizing of Ag NPs inside the polymer matrix, this process starts a bit earlier at around 243˚C. The faster degradation of the Ag containing composite could be due to some rearrangements in the chemical structure of the copolymer, which can affect the degradation of the composite easier, as it was mentioned in the XRD section that the degree of crystallinity of this sample (S2 sample) decreased respect to the S1 sample. The residue in TGA curves could be a means to understand the Ag content in the samples S2; however, this value is higher for the S5 sample, due to the presence of Ag NPs and GnPs in the hybrid form, which can increase the amount of residue.

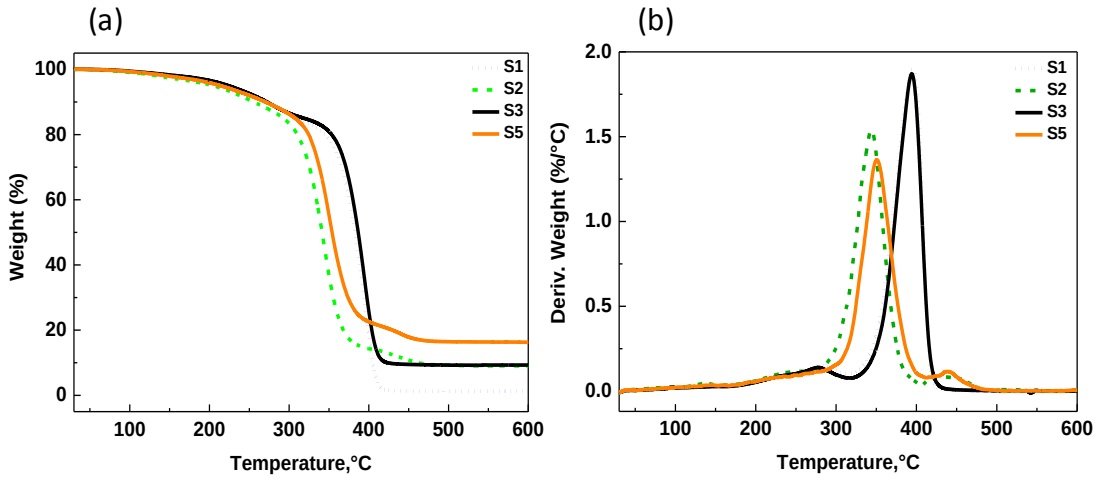

Figure 59. (a) TGA and (b) DTGA curves for the S1, S2, S3, and S5 samples.

5.3.5. Electrical conductivity

Generally, ordinary polymers without conductive nanofillers show insulating properties with electrical resistance in the order of mega Ohms (MΩ) [245,246]. However, polymer matrices filled with metallic or carbon-based nanofillers demonstrate a substantial decrease in the electrical resistance depending on the type and concentration of the filler [238,247,248]. In this study, the as-prepared samples were also characterized for their electrical properties in terms of their electrical sheet resistance. Table 9 shows sheet resistance or surface resistance of the prepared nanocomposites directly measured on a sheet area of 5 mm × 5 mm after applying the silver paste to reduce the contact resistance. Likewise the other neat polymers, unfilled acrylic copolymer film (sample S1) displayed sheet resistance of more than 1 MΩ/square. Or in other words, sample S1 did not show any electrical conductivity. Similarly, the sample S2 with *in-situ* synthesized Ag NPs alone could not reduce the sheet resistance significantly. Although Ag NPs have high electrical conductivity in general, very low concentration of 0.2 wt% of the Ag NPs were unable to generate sufficient interconnected paths to transport electrical current. This has been confirmed in SEM and TEM images where Ag NPs demonstrate cluster formation inside the polymer matrix.

Table 9. Electrical properties of the prepared nanocomposites.

Sample code	Sheet resistance (Ω/square)
S1	≥ 1 M
S2	> 800 k
S3	2.46 k ± 1.58 k
S4	173 ± 39
S5	2.26 k ±1.04 k
S6	38 ± 2.7

Graphene as a magical material shows excellent electrical conductivity (10^6 S/m or 10^{-6} Ω.m resistivity for pure graphene, but more than an order of magnitude higher for graphite) [249,250]. As mentioned before, the polymer matrices filled with high aspect ratio graphene fillers show a substantial reduction in electrical resistance [251,252]. As such, the polymer films filled with only

GnPs demonstrated an electrical sheet resistance of 2.46 kΩ/square and 173 Ω/square at filler's concentration of 5 wt% (sample S3) and 10 wt% (sample S4), respectively. Whereas, the hybrid nanocomposites (samples S5 and S6) with *in-situ* synthesized Ag NPs (at 0.2 wt% loading) demonstrated sheet resistance of 2.26 kΩ/square and 38 Ω/square, respectively. This extremely low sheet resistance of the final hybrid nanocomposite, namely sample S6, with 10 wt% of GnPs and 0.2 wt% of Ag NPs is attributed to the creation of GnPs-Ag bridges within the polymer matrix.

5.3.6. Thermal conductivity

The 2-dimensional or *in-plane* thermal conductivity of different samples were estimated by using infrared-camera imaging, and the obtained results are shown in Figure 60. Note that to perform this experiment; the coatings were made as free standing films of 5 cm × 3 cm with a thickness around 35 μm, in order to decrease the temperature loss from the edges [253]. It is clear that generally at some distances from the hot surface, the temperature starts to decrease for any types of the materials. As seen in Figure 60, the temperature difference ΔT of the sample S1 between the area attached to the hot plate (x = 0 cm) and the farthest point of the sample (x = 5 cm) is about 60˚C, and it confirms the low thermal conductivity of the pure copolymer. However, by introducing the nanofillers especially highly conductive metallic nanoparticles into the polymer matrix, the temperature difference (ΔT) along the x-axis of the samples decreases. For example, sample S2 reaches from 97 ˚C at x = 0 cm to 58 ˚C at x = 5 cm after 4 min of contact time with a ΔT ≈ 39˚C. However, temperature fluctuations along the y-axis are high. As such, sample S2 shows very high-temperature propagation on the corners as compared to the middle region after 4 min, as shown in Figure 60. The *in-situ* synthesized Ag NPs in the polymer matrix has an improving effect on the thermal conductivity of the polymer, which is attributed to the high conductive nature of the silver. The small particle size of the synthesized Ag NPs has an important result in improving the thermal conductivity, due to the high specific surface area of the nanoparticles, which can improve the heat conduction inside the polymer matrix. As heat transfer depends on the surface area of the nanoparticles, the reduction in the size can increase the surface area, resulted in improving thermal conductivity. On the other hand, the Brownian motion of such small nanoparticles in high temperatures can create additional paths for the heat flow in the polymer matrix and amend the thermal conductivity of the composite [254,255]. However, these small nanoparticles are not sufficient for transferring the heat in the polymer matrix, because for heat conduction from one point in the polymer matrix to the other one, the particles should travel a large distance to reach a destination point, due to the small size of them [256]. To reach better results in thermal conductivity we combined GnPs with the synthesized Ag NPs, to see the outcome of hybridization of both nanomaterials on the thermal conductivity. The composites only containing

GnPs namely samples S3 and S4, were analyzed as control samples, to observe the effect of GnPs on the heat conduction. Addition of 5 wt% GnPs into the polymer matrix (sample S3), did not make any noticeable enhancement in the thermal conductivity, which could be related to the low concentration of GnPs that cannot have a good connection with each other in the polymer matrix. Increasing the GnPs quantities to 10 wt% (sample S4) causes higher thermal conductivity, which could be attributed to the high aspect ratio of GnPs and higher concentration that can create some internal connection among the nanoplatelets inside the polymer matrix. However, by hybridizing of two nanomaterials in S5 and S6 samples, the obtained thermal conductivity have a considerable improvement. For example, sample S5 reaches from 100 ˚C at x = 0 cm to 68 ˚C after 4 min of contact time with a $\Delta T \approx 32$˚C. On the other hand, sample S6 stabilizes at 80 ˚C after similar wait time and creates a $\Delta T \approx 20$ ˚C. The reason behind such behavior is the formation of fully interconnected networks in the presence of both nanofillers in the polymer matrix [220,221]. By the creation of such networks in the polymer matrix, the heat can transfer much easier in the x-direction of the samples and as a result, improve the thermal conductivity. Not only the conductive nature of the nanofillers is important for the promotion of thermal conductivity, but also the small size of the synthesized Ag NPs and high aspect ratio of GnPs at the same time can have a superior effect on the thermal conductivity. The thermographic images (Figure 60) of different samples in different times could be a good witness on the improvement of thermal conductivity and heat distribution in the hybrid samples (S5 and S6 samples).

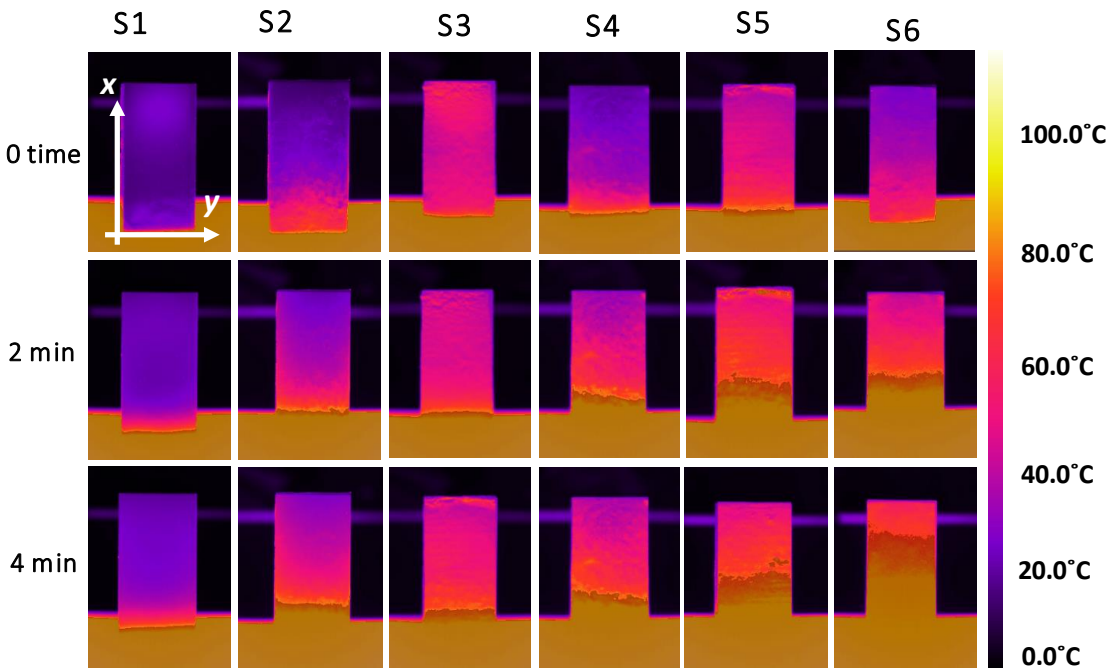

Figure 60. IR-camera observations for different samples at different times and temperature distribution along the x-direction of the samples, when held vertically with the bottom edge in contact with a hot source (150˚C).

To estimate the *in-plane* thermal conductivities *k* of the studied samples a theoretical model was used to simulate their temperature distribution profiles along the *x*-axis, as explained in the following part. The coating layers are held in upright position, which the front side is in contact with air and the back side is insulated with a teflon plate. *L*, *W* and *t* are the lenght, width and thickness of the coatings, respectively. The bottom end of the coating films are attched to the hot plate with a constant temperature, while the surface temperature T_0 was measured by IR-camera imaging in different distances from hot plate. The heat is supposed to be transfered through the *x*-direction of the coatings by conduction (one-dimensional) and transfered to the environment by convection and radiation, which T_a or air temperature is lower than the surface temperature T_0. Since the thickness *t* is much smaller than the length and the width of the coating films, so the convection from the side and the edge areas is considered as negligible values. The cross-sectional area for heat conduction is $A = Wt$ and the primeter for the heat convection is $P = W$. Taking a small elementwith length *dx*, the heat transfer by conduction into the elementi s *Qx* (equation 5).

$$Q_x = -kA\frac{dT}{dx} \qquad \textbf{Equation 5}$$

Where *k* is the thermal conductivity of the coating film. The heat transfer by conduction os the element is Q_{x+dx},

$$Q_{x+dx} = Q_x + \frac{dQ_x}{dx}dx \qquad \textbf{Equation 6}$$

The heat transfer by convection to the air is $Q_{convextion}$,

$$Q_c = \alpha P dx(T - T_a) \qquad \textbf{Equation 7}$$

Where α is the heat transfer coefficient, *T* is the temperature of the coating film at *x*. By considering the steady state, one dimensional heat transfer and using heat balance equations 5-7, we obtained:

$$\frac{d^2T}{dx^2} - \frac{\alpha P}{kA}(T - T_a) = 0 \quad \textbf{Equation 8}$$

The boundary conditions are:

$T = T_0$ at $x = 0$

$\frac{dT}{dx} = 0$ at $x = L$

The solution of equation 8 with subject to the boundary conditions gives the temperature distribution in the coating film along the *x*-direction as:

$$T - T_0 = \frac{(T_0 - T_a)\cosh\left[m(L-x)\right]}{\cosh(mL)} \quad \textbf{Equation 9}$$

Where $m = \sqrt{\frac{\alpha P}{kA}}$. The combined graph with theoretical study is shown in Figure 61 [221,253]. The convective heat transfer coefficient α can be estimated using an empirical correlation available for natural convective heat transfer of air from a hot vertical flat surface that is given by following correlation,

$$N_u = 0.59 Ra^{1/4} \quad \textbf{Equation 10}$$

Where $N_u = \frac{\alpha L}{k_a}$ and $R_a = \frac{g C_{pa} \mu_a \beta_a (T - T_a) W^3}{k_a \nu_a^2}$ are Nusselt number and Rayleigh number, respectively, k_a is the thermal conductivity of air, g is the specific gravity force, C_{pa} is the specific heat capacity of air at constant pressure, μ_a is dynamic viscosity of air, β_a is volume coefficient of air expansion, ν_a is the kinematic viscosity of air. It's worth noting that equation 10 is valid in the range of $2.6 \times 10^4 < R_a < 10^9$.

The characteristics of air at atmospheric pressure and room temperature (about 300 K) are: C_{pa} = 1.0 kJ/kg K, $\mu_a = 1.846 \times 10^{-5}$ kg/m s, $\nu_a = 15.69 \times 10^{-6}$ m^2/s, k_a = 0.026 W/m K, $\beta_a = 3.3 \times 10^{-3}$ K^{-1}. The dimensions of the coating film are L = 0.05 m, W= 0.03 m, $t = 350 \times 10^{-6}$ m. Under these conditions, we find $Ra = 16.55 \times 10^4$, Nu = 20.17, α = 10.49 W/m^2 K. The estimated heat transfer coefficient is in the acceptable range for the equation 10. Then, calculated m is to be 5.47 $k^{-0.5}$ (m is the function of thermal conductivity k). With these calculations, temperature distribution of a surface at different positions along the *x*-direction can be easily calculated for different values of thermal conductivities, as given in following data tables.

For different thermal conductivities, the distribution of temperature along the *x*-axis is calculated as described in the following tables (10-17):

Table 10. Distribution temperature for for k = 100 W/mK along the x-axis.

Position, x (cm)	Temperature (˚C)
0	100
1	69.529
2	52.146
3	42.533
4	37.738
5	36.288

Table 11. Distribution temperature for for k = 300 W/mK along the x-axis.

Position, x (cm)	Temperature (˚C)
0	100
1	82.103
2	69.757
3	61.732
4	57.218
5	55.763

Table 12. Distribution temperature for for k = 500 W/mK along the x-axis.

Position, x (cm)	Temperature (˚C)
0	100
1	87
2	77.623
3	71.297
4	67.647
5	66.454

Table 13. Distribution temperature for for k = 800 W/mK along the x-axis.

Position, x (cm)	Temperature (˚C)
0	100
1	90.755
2	83.876
3	79.14
4	76.367
5	75.454

Table 14. Distribution temperature for for k = 1000 W/mK along the x-axis.

Position, x (cm)	Temperature (˚C)
0	100
1	92.226
2	86.39
3	82.341
4	79.96
5	79.174

Table 15. Distribution temperature for for k = 1200 W/mK along the x-axis.

Position, x (cm)	Temperature (˚C)
0	100
1	93.304
2	88.237
3	84.705
4	82.621
5	81.932

Table 16. Distribution temperature for for k = 1500 W/mK along the x-axis.

Position, x (cm)	Temperature (˚C)
0	100
1	94.428
2	90.2
3	87.239
4	85.486
5	84.905

Table 17. Distribution temperature for for k = 2000 W/mK along the x-axis.

Position, x (cm)	Temperature (˚C)
0	100
1	95.662
2	92.33
3	90.012
4	88.625
5	88.166

The heat transfer profiles, which were estimated according to the equation 9, are displayed in Figure 61, a as solid lines, and different values of thermal conductivity namely as k = 100, 300, 500, 800, 1000, 1200, 1500 and 2000 W/m K were used to calculate m=5.47 $k^{-0.5}$ to get the best fit. For instance, by inserting k = 1200 W/m K in the equation 9 and obtaining the *in-plane* temperature profile, we can see that the S6 sample has a good fitting with this line. So we can conclude that the approximated thermal conductivity of the sample S6 is around 1200 W/m K. On the other hand, the *in-plane* thermal conductivity of the pure acrylic copolymer (sample S1) is estimated to be $k \approx$ 200 W/m K after the fitting with the model. This hyperbolic trend shows the poor thermal conductivity of this material before introducing the nanofillers into it. However, the hybridization of the nanomaterials in the

polymer matrix has a noticeable improvement in the thermal conductivity of the polymer, which is obvious in the fitted graph and also in the infrared images of the samples as explained before.

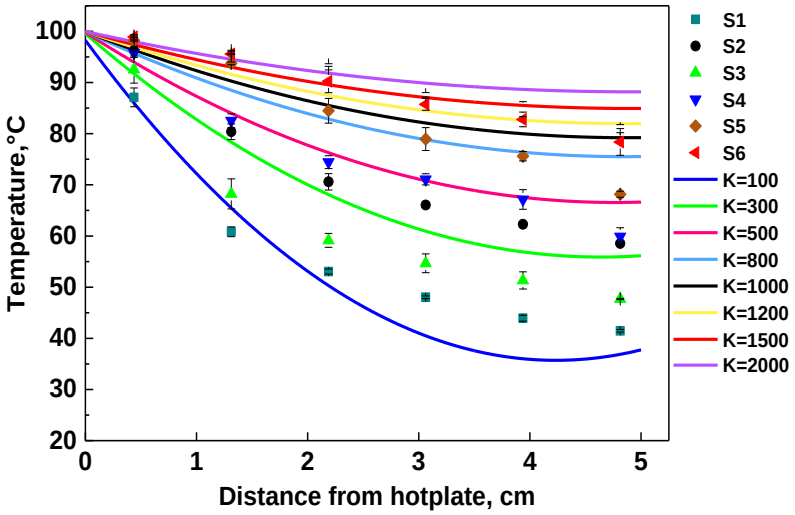

Figure 61. Correlation of the experimental and theoretical temperature measurements along the x-axis.

5.4. Conclusions

We have demonstrated a hybrid nanocomposite/nanocoating, with very high *in-plane* thermal conductivity, based on an in-situ synthesized Ag-NPs and GnPs networks incorporated into an acrylic-based polymer matrix. The fabrication method is simple, low cost and highly scalable for application in lightning strike protective coating in the transportation industry. Thanks to the percolating Ag-NPs/GnPs networks within the polymer matrix, the prepared nanocomposite demonstrated very high *in-plane* thermal conductivity as confirmed by a theoretical model. Moreover, the developed nanocomposite displayed very low electrical sheet resistance such as 38 Ω/square considering that most commercial lightning strike protection materials are highly conductive materials. We estimate that the *in-plane* thermal conductivity of the prepared acrylic copolymer nanocomposites is around ~1200 W/m K at mass contents of 0.2 wt% and 10 wt% corresponding to Ag-NPs and GnPs, respectively. As acrylic-based nanocomposites are very sticky, they can be applied to any surface (wood, metal, ceramics, plastics) for lightning strike protection.

Chapter 6

Prespective and summaries

The main aim of this thesis was to develop the multifunctional polymeric coatings based on sustainable materials and methods for different applications. This study gives information about the surface modification of underneath substrate by deposition a coating onto it, by using eco-friendly and non-toxic materials. In these works we mostly focused on the fabrication of non-wetting and thermally conductive polymeric coatings, however there are a plenty of applications based on polymeric coatings. As it was mentioned in the main text, these coatings can be deposited onto the various range of substrtaes, from metals to textile and porous structures.

Based on the results from chapter 2, it's worth noting that using a primer layer or even a thermal interlayer followed by doing thermal annealing is essential for having a good inclusion among the components, especially for the nanoparticles. This can help to have an abrasion resistant polymeric coating.

According to chapter 3, the presence of a phase-change materials in the combination can be useful to fabricate a polymeric coatings with latent heat storage capabilities for thermal managemnet applications. It should note that encapsulation of these materials is really important to proetct them from leaching, which can be obtained by using a polymer layer around them.

The results of chapter 4, shows that using a bio-based material as a main material in the formula, is really important to decrease the amount of fluorinated matrix in the formulation. Also the non-wetting coatings can decrease the bacterial adhesion property, which can be important in special applications. Furthermore, if the coatings do not relaese any harmful materials, so they can be considered as a biocompatible coating by cell culturing on them.

Based on the results from chapter 5, it can be summarized that in-situ synthesizing of nanoparticles inside the polymer solution can be one of the best method to have a good dispersion of nanomaterials inside the polymer matrix. Also creation of a network connection among the condcutive nanofillers inside the polymer matrix is essential for obtaining a high thermal conductivity in the final polymeric coatings.

Some general conclusions from this doctoral thesis can be summarized as below:

- To acheive the water-repellency property in the surfaces, three different parameters should be controlled as surface chemistry, surface morphology and surface roughness, in order to provide the surfaces with low surface energy that repels water.
- To obtain a robust abrasion resistant coating, there should be a homogenous dispersion of components in the nanocomposite, which can improve the inclusion of materials toward each

other and ameliorate the robustness of the final coating against external forces. There should be the good adhesion force towards the substrate as well.

- The bacterial adhesion can be reduced via fabrication of superhydrophobic coatings, which can be useful in the biomedical applications.
- A high thermal conductivity can be obtained even with the non-condcutive polymer matrix, by making a fully network connection among the condcutive fillers inside the base matrix.

Based on chemical characterization the FTIR analysis can be replaced by photoacoustic spectroscopy, which does not contain the inaccuracies coming from the spectroscope crystal touches the sample surface, which made some errors in FTIR analysis.

According to the final applications of the coatings, many future directions can be inspired from this thesis. One of the most important issues in the fabrication of polymeric coatings that should be noted is to use the sustainable process and materials. The materials can be bio-based ones, the solvents can be green solvents or water-based solutions and the techniques should be simple, cheap and scalable ones.

The other critical challenges is to fabricate a polymeric coating with strong mechanical properties with good adhesion towards the underneath substrate to improve the tribological properties of the surface. This can be acheived by improving the dispersion and interactions among the components, using different layers in the final coatings or even using a rubbery phase inside the formulations.

The coatings can be contained an anti-bacterials agent to behave such as anti-bacterials polymeric coatings for biomedical applications. Also future works will focus on the performance of these kinds of coatings under different hydrodynamic conditions like boundary slip and drag reduction for turbulent flow conditions. The real applications of such coatings ranging from electronics to structural building efficient energy management systems and thermal energy savings can be studied, especially for those with latent heat storage properties.

One applications for non-wetting thermally condcutive coatings is to use them for liquids vapor condensation process, which is important for heat transfer in many industrial processes.

Fabrication of various polymeric coatings based on sustainable materials can be the main future idea, which came from this thesis. These coatings can be included the transparent ones for glass to act as anti-fog, anti-reflectance and self-cleaning coatings, which can be used in cars, buildings and etc., condcutive coatings for thermal interface materials (TIM) and solar cells to improve the efficiency of them. Even coatings on textiles to make wearable electronic devices, which can be used in a wide range of applications ranging from medical care to energy harvesting and storage.

References

[1] W. Choi, A. Tuteja, J.M. Mabry, R.E. Cohen, G.H. McKinley, A modified Cassie–Baxter relationship to explain contact angle hysteresis and anisotropy on non-wetting textured surfaces, J. Colloid Interface Sci. 339 (2009) 208–216. doi:10.1016/J.JCIS.2009.07.027.

[2] J. Gonzales, D. Kurihara, T. Maeda, M. Yamazaki, T. Saruhashi, S. Kimura, H. Sakaue, Novel Superhydrophobic Surface with Solar-Absorptive Material for Improved De-Icing Performance, Mater. . 12 (2019). doi:10.3390/ma12172758.

[3] T. Nishino, M. Meguro, K. Nakamae, M. Matsushita, Y. Ueda, The Lowest Surface Free Energy Based on −CF3 Alignment, Langmuir. 15 (1999) 4321–4323. doi:10.1021/la981727s.

[4] T. Mao, D.C.S. Kuhn, H. Tran, Spread and rebound of liquid droplets upon impact on flat surfaces, AIChE J. 43 (1997) 2169–2179. doi:10.1002/aic.690430903.

[5] D. ~C. Vadillo, A. Soucemarianadin, C. Delattre, D. ~C. ~D. Roux, Dynamic contact angle effects onto the maximum drop impact spreading on solid surfaces, Phys. Fluids. 21 (2009) 122002–122008. doi:10.1063/1.3276259.

[6] G. Whyman, E. Bormashenko, T. Stein, The rigorous derivation of Young, Cassie–Baxter and Wenzel equations and the analysis of the contact angle hysteresis phenomenon, Chem. Phys. Lett. 450 (2008) 355–359. doi:10.1016/J.CPLETT.2007.11.033.

[7] T. Koishi, K. Yasuoka, S. Fujikawa, T. Ebisuzaki, X.C. Zeng, Coexistence and transition between Cassie and Wenzel state on pillared hydrophobic surface, Proc. Natl. Acad. Sci. 106 (2009) 8435 LP-8440. doi:10.1073/pnas.0902027106.

[8] X. Zhu, L. Zhu, H. Chen, L. Yang, W. Zhang, Micro-ball lens structure fabrication based on drop on demand printing the liquid mold, Appl. Surf. Sci. 361 (2016) 80–89. doi:10.1016/J.APSUSC.2015.11.165.

[9] J. De Coninck, F. Dunlop, T. Huillet, Is superhydrophobicity robust with respect to disorder?, Eur. Phys. J. E. 36 (2013) 104. doi:10.1140/epje/i2013-13104-2.

[10] Y. Song, Study of the Femtosecond Laser Processed Surfaces, Imprinting, and Casting for Changing the Wettability of Surfaces, Mech. (and Mater. Eng. -- Diss. Theses, Student Res. (2018). https://digitalcommons.unl.edu/mechengdiss/143 (accessed November 11, 2019).

[11] D.. Packham, Surface energy, surface topography and adhesion, Int. J. Adhes. Adhes. 23 (2003) 437–448. doi:10.1016/S0143-7496(03)00068-X.

[12] R. Asmatulu, W.S. Khan, R.J. Reddy, M. Ceylan, Synthesis and analysis of injection-molded nanocomposites of recycled high-density polyethylene incorporated with graphene nanoflakes, Polym. Compos. 36 (2015) 1565–1573. doi:10.1002/pc.23063.

[13] E.A. Vogler, Structure and reactivity of water at biomaterial surfaces, Adv. Colloid Interface

Sci. 74 (1998) 69–117. doi:10.1016/S0001-8686(97)00040-7.

[14] Q. Cao, L. Li, F. Huang, C. Zuo, Ion-Specific Effects on the Elongation Dynamics of a Nanosized Water Droplet in Applied Electric Fields, Langmuir. 33 (2017) 428–437. doi:10.1021/acs.langmuir.6b04101.

[15] A. Çağlar, M. Yıldırım, U. Cengiz, İ. Kaya, Superhydrophobic-electrochromic PEDOT/PFHP bilayer surfaces, Thin Solid Films. 619 (2016) 187–194. doi:10.1016/J.TSF.2016.10.070.

[16] L. Feng, S. Li, Y. Li, H. Li, L. Zhang, J. Zhai, Y. Song, B. Liu, L. Jiang, D. Zhu, Super-Hydrophobic Surfaces: From Natural to Artificial, Adv. Mater. 14 (2002) 1857–1860. doi:10.1002/adma.200290020.

[17] K. Koch, B. Bhushan, W. Barthlott, Multifunctional surface structures of plants: An inspiration for biomimetics, Prog. Mater. Sci. 54 (2009) 137–178. doi:10.1016/J.PMATSCI.2008.07.003.

[18] C. NEINHUIS, W. BARTHLOTT, Characterization and Distribution of Water-repellent, Self-cleaning Plant Surfaces, Ann. Bot. 79 (1997) 667–677. doi:10.1006/anbo.1997.0400.

[19] T. Wagner, C. Neinhuis, W. Barthlott, Wettability and Contaminability of Insect Wings as a Function of Their Surface Sculptures, Acta Zool. 77 (1996) 213–225. doi:10.1111/j.1463-6395.1996.tb01265.x.

[20] Z. Cerman, B.F. Striffler, W. Barthlott, Dry in the Water: The Superhydrophobic Water Fern Salvinia – a Model for Biomimetic Surfaces BT - Functional Surfaces in Biology: Little Structures with Big Effects Volume 1, in: S.N. Gorb (Ed.), Springer Netherlands, Dordrecht, 2009: pp. 97–111. doi:10.1007/978-1-4020-6697-9_7.

[21] Z. Guo, W. Liu, Biomimic from the superhydrophobic plant leaves in nature: Binary structure and unitary structure, Plant Sci. 172 (2007) 1103–1112. doi:10.1016/J.PLANTSCI.2007.03.005.

[22] W.R. Hansen, K. Autumn, Evidence for self-cleaning in gecko setae, Proc. Natl. Acad. Sci. U. S. A. 102 (2005) 385 LP-389. doi:10.1073/pnas.0408304102.

[23] Y.Y. Yan, N. Gao, W. Barthlott, Mimicking natural superhydrophobic surfaces and grasping the wetting process: A review on recent progress in preparing superhydrophobic surfaces, Adv. Colloid Interface Sci. 169 (2011) 80–105. doi:10.1016/J.CIS.2011.08.005.

[24] H. Yang, F. Liang, Y. Chen, Q. Wang, X. Qu, Z. Yang, Lotus leaf inspired robust superhydrophobic coating from strawberry-like Janus particles, NPG Asia Mater. 7 (2015) e176–e176. doi:10.1038/am.2015.33.

[25] M. Ghasemlou, F. Daver, E.P. Ivanova, B. Adhikari, Bio-inspired sustainable and durable

superhydrophobic materials: from nature to market, J. Mater. Chem. A. 7 (2019) 16643–16670. doi:10.1039/C9TA05185F.

[26] R.-E. Avrămescu, M.V. Ghica, C. Dinu-Pîrvu, R. Prisada, L. Popa, Superhydrophobic Natural and Artificial Surfaces-A Structural Approach, Mater. (Basel, Switzerland). 11 (2018) 866. doi:10.3390/ma11050866.

[27] T.C. Hobæk, K.G. Leinan, H.P. Leinaas, C. Thaulow, Surface Nanoengineering Inspired by Evolution, Bionanoscience. 1 (2011) 63. doi:10.1007/s12668-011-0014-5.

[28] PAPER CHEMISTRY: Approaching super-hydrophobicity from cellulosic materials: A Review , Nord. Pulp Pap. Res. J. . 28 (2013) 216. doi:10.3183/npprj-2013-28-02-p216-238.

[29] M. Wolfs, T. Darmanin, F. Guittard, Superhydrophobic Polymers, Encycl. Polym. Sci. Technol. (2013). doi:doi:10.1002/0471440264.pst594.

[30] Q.-Y. Cheng, X.-P. An, Y.-D. Li, C.-L. Huang, J.-B. Zeng, Sustainable and Biodegradable Superhydrophobic Coating from Epoxidized Soybean Oil and ZnO Nanoparticles on Cellulosic Substrates for Efficient Oil/Water Separation, ACS Sustain. Chem. Eng. 5 (2017) 11440–11450. doi:10.1021/acssuschemeng.7b02549.

[31] I.S. Bayer, D. Fragouli, A. Attanasio, B. Sorce, G. Bertoni, R. Brescia, R. Di Corato, T. Pellegrino, M. Kalyva, S. Sabella, P.P. Pompa, R. Cingolani, A. Athanassiou, Water-Repellent Cellulose Fiber Networks with Multifunctional Properties, ACS Appl. Mater. Interfaces. 3 (2011) 4024–4031. doi:10.1021/am200891f.

[32] W. Wang, K. Lockwood, L.M. Boyd, M.D. Davidson, S. Movafaghi, H. Vahabi, S.R. Khetani, A.K. Kota, Superhydrophobic Coatings with Edible Materials, ACS Appl. Mater. Interfaces. 8 (2016) 18664–18668. doi:10.1021/acsami.6b06958.

[33] J. Ju, X. Yao, X. Hou, Q. Liu, Y.S. Zhang, A. Khademhosseini, A highly stretchable and robust non-fluorinated superhydrophobic surface, J. Mater. Chem. A. 5 (2017) 16273–16280. doi:10.1039/C6TA11133E.

[34] A. Milionis, R. Ruffilli, I.S. Bayer, Superhydrophobic nanocomposites from biodegradable thermoplastic starch composites (Mater-Bi®), hydrophobic nano-silica and lycopodium spores, RSC Adv. 4 (2014) 34395–34404. doi:10.1039/C4RA04117H.

[35] A. Milionis, K. Dang, M. Prato, E. Loth, I.S. Bayer, Liquid repellent nanocomposites obtained from one-step water-based spray, J. Mater. Chem. A. 3 (2015) 12880–12889. doi:10.1039/C5TA02672E.

[36] S. Naderizadeh, J.A. Heredia-Guerrero, G. Caputo, S. Grasselli, A. Malchiodi, A. Athanassiou, I.S. Bayer, Superhydrophobic Coatings from Beeswax-in-Water Emulsions with Latent Heat Storage Capability, Adv. Mater. Interfaces. 6 (2019) 1801782.

doi:10.1002/admi.201801782.

[37] A.M. Rather, N. Jana, S. Begum, H.K. Srivastava, U. Manna, Exceptional control on physical properties of a polymeric material through alcoholic solvent-mediated environment-friendly Michael addition reaction, Green Chem. 19 (2017) 4527–4532. doi:10.1039/C7GC02286G.

[38] M. Ma, R.M. Hill, Superhydrophobic surfaces, Curr. Opin. Colloid Interface Sci. 11 (2006) 193–202. doi:10.1016/J.COCIS.2006.06.002.

[39] H.P.C. Barry Jones, Technical Director, Fluoropolymers for Coating Applications, JCT CoatingsTech Mag. 5 (2008) 44–48.

[40] J.W. Martin, S.A. Mabury, K.R. Solomon, D.C.G. Muir, Progress toward understanding the bioaccumulation of perfluorinated alkyl acids, Environ. Toxicol. Chem. 32 (2013) 2421–2423. doi:10.1002/etc.2376.

[41] T.M. Schutzius, I.S. Bayer, M.K. Tiwari, C.M. Megaridis, Novel Fluoropolymer Blends for the Fabrication of Sprayable Multifunctional Superhydrophobic Nanostructured Composites, Ind. Eng. Chem. Res. 50 (2011) 11117–11123. doi:10.1021/ie200814r.

[42] C.P. Chengelis, J.B. Kirkpatrick, A. Radovsky, M. Shinohara, A 90-day repeated dose oral (gavage) toxicity study of perfluorohexanoic acid (PFHxA) in rats (with functional observational battery and motor activity determinations), Reprod. Toxicol. 27 (2009) 342–351. doi:10.1016/J.REPROTOX.2009.01.006.

[43] S.G. Lee, D.S. Ham, D.Y. Lee, H. Bong, K. Cho, Transparent Superhydrophobic/Translucent Superamphiphobic Coatings Based on Silica–Fluoropolymer Hybrid Nanoparticles, Langmuir. 29 (2013) 15051–15057. doi:10.1021/la404005b.

[44] M.-G. Jeong, H.O. Seo, K.-D. Kim, D.H. Kim, Y.D. Kim, D.C. Lim, Quenching of photocatalytic activity and enhancement of photostability of ZnO particles by polydimethysiloxane coating, J. Mater. Sci. 47 (2012) 5190–5196. doi:10.1007/s10853-012-6402-6.

[45] H. Chang, K. Tu, X. Wang, J. Liu, Facile preparation of stable superhydrophobic coatings on wood surfaces using silica-polymer nanocomposites, BioResources. 10 (2015) 2585–2596. doi:10.15376/biores.10.2.2585-2596.

[46] M.E. Yazdanshenas, M. Shateri-Khalilabad, One-Step Synthesis of Superhydrophobic Coating on Cotton Fabric by Ultrasound Irradiation, Ind. Eng. Chem. Res. 52 (2013) 12846–12854. doi:10.1021/ie401133q.

[47] D. Lv, H. Shao, X. Gao, K. Lu, H. Lu, H. Ma, Fabrication and corrosion resistance properties of super-hydrophobic coatings on iron and steel substrates by creating micro-/nano-structures

and modifying rough surfaces, RSC Adv. 6 (2016) 93419–93427. doi:10.1039/C6RA17655K.

[48] A.M. Kansara, S.G. Chaudhri, P.S. Singh, A facile one-step preparation method of recyclable superhydrophobic polypropylene membrane for oil–water separation, RSC Adv. 6 (2016) 61129–61136. doi:10.1039/C6RA11008H.

[49] X.Y. Ling, I.Y. Phang, G.J. Vancso, J. Huskens, D.N. Reinhoudt, Stable and Transparent Superhydrophobic Nanoparticle Films, Langmuir. 25 (2009) 3260–3263. doi:10.1021/la8040715.

[50] J. Bravo, L. Zhai, Z. Wu, R.E. Cohen, M.F. Rubner, Transparent superhydrophobic films based on silica nanoparticles, Langmuir. 23 (2007) 7293–7298. doi:10.1021/la070159q.

[51] M. Drahansky, M.. Paridah, A. Moradbak, A.. Mohamed, F. abdulwahab taiwo Owolabi, M. Asniza, S.H.. Abdul Khalid, We are IntechOpen , the world ' s leading publisher of Open Access books Built by scientists , for scientists TOP 1 %, Intech. i (2016) 13. doi:http://dx.doi.org/10.5772/57353.

[52] X.-F. Zhang, J.-P. Zhao, J.-M. Hu, Abrasion-Resistant, Hot Water-Repellent and Self-Cleaning Superhydrophobic Surfaces Fabricated by Electrophoresis of Nanoparticles in Electrodeposited Sol–Gel Films, Adv. Mater. Interfaces. 4 (2017) 1700177. doi:10.1002/admi.201700177.

[53] P. Nikolay, C. Jagannath, S. Georgi, S. Alla, I. Leonid, Anti-Icing Superhydrophobic Surfaces Based on Core-Shell Fossil Particles, Adv. Mater. Interfaces. 2 (2015) 1500124. doi:10.1002/admi.201500124.

[54] C.-H. Xue, J. Chen, W. Yin, S.-T. Jia, J.-Z. Ma, Superhydrophobic conductive textiles with antibacterial property by coating fibers with silver nanoparticles, Appl. Surf. Sci. 258 (2012) 2468–2472. doi:10.1016/J.APSUSC.2011.10.074.

[55] C. Gao, Z. Sun, K. Li, Y. Chen, Y. Cao, S. Zhang, L. Feng, Integrated oil separation and water purification by a double-layer TiO2-based mesh, Energy Environ. Sci. 6 (2013) 1147–1151. doi:10.1039/C3EE23769A.

[56] A.L. Moore, L. Shi, Emerging challenges and materials for thermal management of electronics, Mater. Today. 17 (2014) 163–174. doi:10.1016/j.mattod.2014.04.003.

[57] X.C. Tong, Advanced Materials for Thermal Management of Electronic Packaging, 2011. doi:10.1007/978-1-4419-7759-5.

[58] Z. Han, A. Fina, Thermal conductivity of carbon nanotubes and their polymer nanocomposites: A review, Prog. Polym. Sci. 36 (2011) 914–944. doi:10.1016/j.progpolymsci.2010.11.004.

[59] X. Huang, P. Jiang, T. Tanaka, A review of dielectric polymer composites with high thermal conductivity, IEEE Electr. Insul. Mag. 27 (2011) 8–16. doi:10.1109/MEI.2011.5954064.

[60] S.Y. Kim, Y.J. Noh, J. Yu, Thermal conductivity of graphene nanoplatelets filled composites fabricated by solvent-free processing for the excellent filler dispersion and a theoretical approach for the composites containing the geometrized fillers, Compos. Part A Appl. Sci. Manuf. 69 (2015) 219–225. doi:10.1016/J.COMPOSITESA.2014.11.018.

[61] A. Bjorneklett, L. Halbo, H. Kristiansen, Thermal conductivity of epoxy adhesives filled with silver particles, Int. J. Adhes. Adhes. 12 (1992) 99–104. doi:10.1016/0143-7496(92)90030-Y.

[62] W. Zhou, C. Wang, T. Ai, K. Wu, F. Zhao, H. Gu, A novel fiber-reinforced polyethylene composite with added silicon nitride particles for enhanced thermal conductivity, Compos. Part A Appl. Sci. Manuf. 40 (2009) 830–836. doi:10.1016/j.compositesa.2009.04.005.

[63] H. Chen, V. V. Ginzburg, J. Yang, Y. Yang, W. Liu, Y. Huang, L. Du, B. Chen, Thermal conductivity of polymer-based composites: Fundamentals and applications, Prog. Polym. Sci. 59 (2016) 41–85. doi:10.1016/J.PROGPOLYMSCI.2016.03.001.

[64] W. Buck, S. Rudtsch, Thermal Properties, in: H. Czichos, T. Saito, L. Smith (Eds.), Springer Handb. Mater. Meas. Methods, Springer Berlin Heidelberg, Berlin, Heidelberg, 2006: pp. 399–429. doi:10.1007/978-3-540-30300-8_8.

[65] J.M. Corsan, Axial Heat Flow Methods of Thermal Conductivity Measurement for Good Conducting Materials, in: K.D. Maglić, A. Cezairliyan, V.E. Peletsky (Eds.), Compend. Thermophys. Prop. Meas. Methods Vol. 2 Recomm. Meas. Tech. Pract., Springer US, Boston, MA, 1992: pp. 3–31. doi:10.1007/978-1-4615-3286-6_1.

[66] W. Nunes dos Santos, P. Mummery, A. Wallwork, Thermal diffusivity of polymers by the laser flash technique, Polym. Test. 24 (2005) 628–634. doi:10.1016/J.POLYMERTESTING.2005.03.007.

[67] S.Y. Kwon, S. Lee, Precise measurement of thermal conductivity of liquid over a wide temperature range using a transient hot-wire technique by uncertainty analysis, Thermochim. Acta. 542 (2012) 18–23. doi:10.1016/j.tca.2011.12.015.

[68] E. Solórzano, M.A. Rodriguez-Perez, J.A. De Saja, Thermal conductivity of cellular metals measured by the transient plane source method, Adv. Eng. Mater. 10 (2008) 596–602. doi:10.1002/adem.200800182.

[69] C. Heinle, D. Drummer, Potential of thermally conductive polymers for the cooling of mechatronic parts, Phys. Procedia. 5 (2010) 735–744. doi:10.1016/J.PHPRO.2010.08.106.

[70] Y.V. Trofimov, On application of heat-conductive plastics in LED technology, Semicond.

Phys. Quantum Electron. Optoelectron. 16 (2013) 198–200. doi:10.15407/spqeo16.02.198.

[71] B. Lee, J.Z. Liu, B. Sun, C.Y. Shen, G.C. Dai, Thermally conductive and electrically insulating EVA composite encapsulant for solar photovoltaic (PV) cell, Express Polym. Lett. 2 (2008) 357–363. doi:10.3144/expresspolymlett.2008.42.

[72] H. Maleki, J.R. Selman, R.B. Dinwiddie, H. Wang, High thermal conductivity negative electrode material for lithium-ion batteries, J. Power Sources. 94 (2001) 26–35. doi:10.1016/S0378-7753(00)00661-3.

[73] H. Ogihara, J. Xie, J. Okagaki, T. Saji, Simple Method for Preparing Superhydrophobic Paper: Spray-Deposited Hydrophobic Silica Nanoparticle Coatings Exhibit High Water-Repellency and Transparency, Langmuir. 28 (2012) 4605–4608. doi:10.1021/la204492q.

[74] J. Zhang, B. Li, L. Wu, A. Wang, Facile preparation of durable and robust superhydrophobic textiles by dip coating in nanocomposite solution of organosilanes, Chem. Commun. 49 (2013) 11509–11511. doi:10.1039/C3CC43238F.

[75] S. Naderizadeh, A. Athanassiou, I.S. Bayer, Interfacing superhydrophobic silica nanoparticle films with graphene and thermoplastic polyurethane for wear/abrasion resistance, J. Colloid Interface Sci. 519 (2018) 285–295. doi:10.1016/J.JCIS.2018.02.065.

[76] D. Goswami, S.K. Medda, G. De, Superhydrophobic films on glass surface derived from trimethylsilanized silica gel nanoparticles, ACS Appl. Mater. Interfaces. 3 (2011) 3440–3447. doi:10.1021/am200666m.

[77] T. Karakouz, B.M. Maoz, G. Lando, A. Vaskevich, I. Rubinstein, Stabilization of Gold Nanoparticle Films on Glass by Thermal Embedding, ACS Appl. Mater. Interfaces. 3 (2011) 978–987. doi:10.1021/am100878r.

[78] J.F.F. E.Enríqueza, M . A. de la Rubiab, F. Gonzálezc, A. Alburquerquec, Efficient encapsulation of low dimensional particles in thin films to obtain functional coatings, Mater. Des. 104 (2016) 87–94. doi:10.1016/J.MATDES.2016.05.024.

[79] I.S. Bayer, K.G. Krishnan, R. Robison, E. Loth, D.H. Berry, T.E. Farrell, J.D. Crouch, Thermal Alternating Polymer Nanocomposite (TAPNC) Coating Designed to Prevent Aerodynamic Insect Fouling, Sci. Rep. 6 (2016) 38459. http://dx.doi.org/10.1038/srep38459.

[80] Q. Xi, X. Chen, D.G. Evans, W. Yang, Gold Nanoparticle-Embedded Porous Graphene Thin Films Fabricated via Layer-by-Layer Self-Assembly and Subsequent Thermal Annealing for Electrochemical Sensing, Langmuir. 28 (2012) 9885–9892. doi:10.1021/la301440k.

[81] A.S. Ilker S. Bayer, Alexander J. Davis, Eric. Loth, Water jet resistant superhydrophobic carbonaceous films by flame synthesis and tribocharging, Mater. Today Commun. 3 (2015) 57–68. doi:10.1016/J.MTCOMM.2015.04.004.

[82] I.S. Bayer, A.J. Davis, A. Biswas, Robust superhydrophobic surfaces from small diffusion flame treatment of hydrophobic polymers, RSC Adv. 4 (2014) 264–268. doi:10.1039/C3RA44169E.

[83] M.C.B. H. J. Qia, Stress–strain behavior of thermoplastic polyurethanes, Mech. Mater. 37 (2005) 817–839. doi:10.1016/J.MECHMAT.2004.08.001.

[84] F. Chang, M.-Y. Yang, Mechanical fracture behavior of polyacetal and thermoplastic polyurethane elastomer toughened polyacetal, Polym. Eng. Sci. 30 (1990) 543–552. doi:10.1002/pen.760300907.

[85] D.K. Chattopadhyay, K.V.S.N. Raju, Structural engineering of polyurethane coatings for high performance applications, Prog. Polym. Sci. 32 (2007) 352–418. doi:10.1016/j.progpolymsci.2006.05.003.

[86] K. Kojio, M. Furukawa, Y. Nonaka, S. Nakamura, Control of Mechanical Properties of Thermoplastic Polyurethane Elastomers by Restriction of Crystallization of Soft Segment, Materials (Basel). 3 (2010) 5097–5110. doi:10.3390/ma3125097.

[87] H.-Y. Mi, M.R. Salick, X. Jing, B.R. Jacques, W.C. Crone, X.-F. Peng, L.-S. Turng, Characterization of thermoplastic polyurethane/polylactic acid (TPU/PLA) tissue engineering scaffolds fabricated by microcellular injection molding, Mater. Sci. Eng. C. 33 (2013) 4767–4776. doi:10.1016/j.msec.2013.07.037.

[88] J. Tan, Y. Mei Ding, X. Tao He, Y. Liu, Y. An, W. Min Yang, Abrasion resistance of thermoplastic polyurethane materials blended with ethylene-propylene-diene monomer rubber, J. Appl. Polym. Sci. 110 (2008) 1851–1857. doi:10.1002/app.28756.

[89] H.-Y. Mi, X. Jing, B.N. Napiwocki, B.C. Hagerty, G. Chen, L.-S. Turng, Biocompatible, Degradable Thermoplastic Polyurethane Based on Polycaprolactone-Block-Polytetrahydrofuran-Block-Polycaprolactone Copolymer for Soft Tissue Engineering, J. Mater. Chem. B. 5 (2017) 4137–4151. doi:10.1039/C7TB00419B.

[90] A. Milionis, J. Languasco, E. Loth, I.S. Bayer, Analysis of wear abrasion resistance of superhydrophobic acrylonitrile butadiene styrene rubber (ABS) nanocomposites, Chem. Eng. J. 281 (2015) 730–738. doi:10.1016/j.cej.2015.06.086.

[91] J.O.F. West, G.W. Critchlow, D.R. Lake, R. Banks, Development of a superhydrophobic polyurethane-based coating from a two-step plasma-fluoroalkyl silane treatment, Int. J. Adhes. Adhes. 68 (2016) 195–204. doi:10.1016/j.ijadhadh.2016.03.007.

[92] R.C. Pietro. Cataldi, Ilker S. Bayer, Gabriele. Nanni, Athanassia. Athanassioua, Francesco. Bonaccorso, Vittorio. Pellegrini, Antonio Esaudel Rio Castillo, Filiberto. Ricciardella, Sergey. Artyukhin, Marc-AdrienTronche, Yury. Gogotsi, Effect of graphene nano-platelet

morphology on the elastic modulus of soft and hard biopolymers, Carbon N. Y. 109 (2016) 331–339. doi:10.1016/J.CARBON.2016.08.026.

[93] C.A. P., Z.S. A., B.A. A., Computer program for the grain analysis of AFM images of nanoparticles placed on a rough surface, Surf. Interface Anal. 38 (2006) 679–681. doi:10.1002/sia.2294.

[94] M.T. Masood, J.A. Heredia-Guerrero, L. Ceseracciu, F. Palazon, A. Athanassiou, I.S. Bayer, Superhydrophobic high impact polystyrene (HIPS) nanocomposites with wear abrasion resistance, Chem. Eng. J. 322 (2017) 10–21. doi:10.1016/J.CEJ.2017.04.007.

[95] J. Li, R. Wu, Z. Jing, L. Yan, F. Zha, Z. Lei, One-Step Spray-Coating Process for the Fabrication of Colorful Superhydrophobic Coatings with Excellent Corrosion Resistance, Langmuir. 31 (2015) 10702–10707. doi:10.1021/acs.langmuir.5b02734.

[96] Y. Li, S. Chen, M. Wu, J. Sun, All Spraying Processes for the Fabrication of Robust, Self-Healing, Superhydrophobic Coatings, Adv. Mater. 26 (2014) 3344–3348. doi:10.1002/adma.201306136.

[97] M.J. Roberts, G.A. Lindsay, W.N. Herman, K.J. Wynne, Thermally Stable Nonlinear Optical Films by Alternating Polyelectrolyte Deposition on Hydrophobic Substrates, J. Am. Chem. Soc. 120 (1998) 11202–11203. doi:10.1021/ja9822613.

[98] P.G. Jessop, Searching for green solvents, Green Chem. 13 (2011) 1391–1398. doi:10.1039/C0GC00797H.

[99] K. Chen, S. Zhou, L. Wu, Facile fabrication of self-repairing superhydrophobic coatings, Chem. Commun. 50 (2014) 11891–11894. doi:10.1039/C3CC49251F.

[100] Y. Liu, Z. Liu, Y. Liu, H. Hu, Y. Li, P. Yan, B. Yu, F. Zhou, One-Step Modification of Fabrics with Bioinspired Polydopamine@Octadecylamine Nanocapsules for Robust and Healable Self-Cleaning Performance, Small. 11 (2015) 426–431. doi:10.1002/smll.201402383.

[101] Z. Dai, K. Yang, Q. Dong, Mechanical, Thermal and Morphology Properties of Thermoplastic Polyurethane Copolymers Incorporating α,ω-Dihydroxy-[poly(propyleneoxide)-poly (dimethylsiloxane)-poly(propyleneoxide)] of Varying Poly(propyleneoxide) Molecular Weight, Open J. Synth. Theory Appl. 4 (2015) 41–57. doi:10.4236/ojsta.2015.43005.

[102] G.H. Lopes, J. Junges, R. Fiorio, M. Zeni, A.J. Zattera, Thermoplastic polyurethane synthesis using POSS as a chain modifier, Mater. Res. 15 (2012) 698–704. doi:10.1590/S1516-14392012005000085.

[103] J.-T. Chen, W.-L. Chen, P.-W. Fan, I.-C. Yao, Effect of Thermal Annealing on the Surface

Properties of Electrospun Polymer Fibers, Macromol. Rapid Commun. 35 (2014) 360–366. doi:10.1002/marc.201300290.

[104] T. Ge, G.S. Grest, M.O. Robbins, Tensile Fracture of Welded Polymer Interfaces: Miscibility, Entanglements, and Crazing, Macromolecules. 47 (2014) 6982–6989. doi:10.1021/ma501473q.

[105] R. Di Mundo, F. Palumbo, R. D'Agostino, Nanotexturing of polystyrene surface in fluorocarbon plasmas: from sticky to slippery superhydrophobicity, Langmuir. 24 (2008) 5044–5051. doi:10.1021/la800059a.

[106] M. Munz, C.E. Giusca, R.L. Myers-Ward, D.K. Gaskill, O. Kazakova, Thickness-Dependent Hydrophobicity of Epitaxial Graphene, ACS Nano. 9 (2015) 8401–8411. doi:10.1021/acsnano.5b03220.

[107] H. Wang, S.W. Tay, R.S. Hong, P.K. Pallathadka, L. Hong, From the solvothermally treated poly(vinylidenefluoride) colloidal suspension to sticky hydrophobic coating, Colloid Polym. Sci. 292 (2014) 807–815. doi:10.1007/s00396-013-3126-3.

[108] I. Bayer, I. S., On the Durability and Wear Resistance of Transparent Superhydrophobic Coatings, Coatings. 7 (2017) 12. doi:10.3390/coatings7010012.

[109] M.J. Nine, M.A. Cole, D.N.H. Tran, D. Losic, Graphene: a multipurpose material for protective coatings, J. Mater. Chem. A. 3 (2015) 12580–12602. doi:10.1039/C5TA01010A.

[110] A. Steele, A. Davis, J. Kim, E. Loth, I.S. Bayer, Wear Independent Similarity, ACS Appl. Mater. Interfaces. 7 (2015) 12695–12701. doi:10.1021/acsami.5b00725.

[111] S.S. Mahajan, G. Subbarayan, B.G. Sammakia, Estimating thermal conductivity of amorphous silica nanoparticles and nanowires using molecular dynamics simulations, Phys. Rev. E - Stat. Nonlinear, Soft Matter Phys. 76 (2007) 1–14. doi:10.1103/PhysRevE.76.056701.

[112] K.M.F. Shahil, A.A. Balandin, Thermal properties of graphene and multilayer graphene: Applications in thermal interface materials, Solid State Commun. 152 (2012) 1331–1340. doi:10.1016/J.SSC.2012.04.034.

[113] B.S. Yilbas, A. Ibrahim, H. Ali, M. Khaled, T. Laoui, Hydrophobic and optical characteristics of graphene and graphene oxide films transferred onto functionalized silica particles deposited glass surface, Appl. Surf. Sci. 442 (2018) 213–223. doi:10.1016/J.APSUSC.2018.02.176.

[114] P. Wang, M. Chen, H. Han, X. Fan, Q. Liu, J. Wang, Transparent and abrasion-resistant superhydrophobic coating with robust self-cleaning function in either air or oil, J. Mater. Chem. A. 4 (2016) 7869–7874. doi:10.1039/C6TA01082B.

[115] N. Zhang, S. Lu, W. Xu, Y. Zhang, Controlled growth of CuO–Cu3Pt/Cu micro-nano binary architectures on copper substrate and its superhydrophobic behavior, New J. Chem. 38 (2014) 4534–4540. doi:10.1039/C4NJ00660G.

[116] S. Jia, M. Liu, Y. Wu, S. Luo, Y. Qing, H. Chen, Facile and scalable preparation of highly wear-resistance superhydrophobic surface on wood substrates using silica nanoparticles modified by VTES, Appl. Surf. Sci. 386 (2016) 115–124. doi:10.1016/J.APSUSC.2016.06.004.

[117] D. Ebert, B. Bhushan, Transparent, Superhydrophobic, and Wear-Resistant Coatings on Glass and Polymer Substrates Using SiO2, ZnO, and ITO Nanoparticles, Langmuir. 28 (2012) 11391–11399. doi:10.1021/la301479c.

[118] D. Ebert, B. Bhushan, Wear-resistant rose petal-effect surfaces with superhydrophobicity and high droplet adhesion using hydrophobic and hydrophilic nanoparticles, J. Colloid Interface Sci. 384 (2012) 182–188. doi:10.1016/J.JCIS.2012.06.070.

[119] Y. Lu, S. Sathasivam, J. Song, C.R. Crick, C.J. Carmalt, I.P. Parkin, Robust self-cleaning surfaces that function when exposed to either air or oil, Science (80-.). 347 (2015) 1132 LP-1135. http://science.sciencemag.org/content/347/6226/1132.abstract.

[120] W.S.Y. Wong, Z.H. Stachurski, D.R. Nisbet, A. Tricoli, Ultra-Durable and Transparent Self-Cleaning Surfaces by Large-Scale Self-Assembly of Hierarchical Interpenetrated Polymer Networks, ACS Appl. Mater. Interfaces. 8 (2016) 13615–13623. doi:10.1021/acsami.6b03414.

[121] C. Cai, N. Sang, S. Teng, Z. Shen, J. Guo, X. Zhao, Z. Guo, Superhydrophobic surface fabricated by spraying hydrophobic R974 nanoparticles and the drag reduction in water, Surf. Coatings Technol. 307 (2016) 366–373. doi:10.1016/J.SURFCOAT.2016.09.009.

[122] Y. Wang, B. Bhushan, Wear-Resistant and Antismudge Superoleophobic Coating on Polyethylene Terephthalate Substrate Using SiO2 Nanoparticles, ACS Appl. Mater. Interfaces. 7 (2015) 743–755. doi:10.1021/am5067755.

[123] B. Chen, J. Qiu, E. Sakai, N. Kanazawa, R. Liang, H. Feng, Robust and Superhydrophobic Surface Modification by a “Paint + Adhesive” Method: Applications in Self-Cleaning after Oil Contamination and Oil–Water Separation, ACS Appl. Mater. Interfaces. 8 (2016) 17659–17667. doi:10.1021/acsami.6b04108.

[124] M. Stepien, G. Chinga-Carrasco, J.J. Saarinen, H. Teisala, M. Tuominen, M. Aromaa, J. Haapanen, J. Kuusipalo, J.M. Mäkelä, M. Toivakka, Wear resistance of nanoparticle coatings on paperboard, Wear. 307 (2013) 112–118. doi:10.1016/J.WEAR.2013.08.022.

[125] X. Tian, T. Verho, R.H.A. Ras, Moving superhydrophobic surfaces toward real-world

applications, Science (80-.). 352 (2016) 142 LP-143. doi:10.1126/science.aaf2073.

[126] H. Zhang, H. Zhang, L. Tang, L. Zhou, C. Eger, Z. Zhang, Comparative study on the optical, surface mechanical and wear resistant properties of transparent coatings filled with pyrogenic and colloidal silica nanoparticles, Compos. Sci. Technol. 71 (2011) 471–479. doi:10.1016/J.COMPSCITECH.2010.12.022.

[127] W. Zhang, P. Lu, L. Qian, H. Xiao, Fabrication of superhydrophobic paper surface via wax mixture coating, Chem. Eng. J. 250 (2014) 431–436. doi:10.1016/J.CEJ.2014.04.050.

[128] X. Zhao, T. Hu, J. Zhang, Superhydrophobic coatings with high repellency to daily consumed liquid foods based on food grade waxes, J. Colloid Interface Sci. 515 (2018) 255–263. doi:10.1016/J.JCIS.2018.01.034.

[129] I.S. Bayer, D. Fragouli, P.J. Martorana, L. Martiradonna, R. Cingolani, A. Athanassiou, Solvent resistant superhydrophobic films from self-emulsifying carnauba wax–alcohol emulsions, Soft Matter. 7 (2011) 7939–7943. doi:10.1039/C1SM05710C.

[130] M.G.A. Vieira, M.A. da Silva, L.O. dos Santos, M.M. Beppu, Natural-based plasticizers and biopolymer films: A review, Eur. Polym. J. 47 (2011) 254–263. doi:10.1016/J.EURPOLYMJ.2010.12.011.

[131] I. Krupa, G. Miková, A.S. Luyt, Phase change materials based on low-density polyethylene/paraffin wax blends, Eur. Polym. J. 43 (2007) 4695–4705. doi:10.1016/J.EURPOLYMJ.2007.08.022.

[132] W. Mhike, W.W. Focke, J.P. Mofokeng, A.S. Luyt, Thermally conductive phase-change materials for energy storage based on low-density polyethylene, soft Fischer–Tropsch wax and graphite, Thermochim. Acta. 527 (2012) 75–82. doi:10.1016/J.TCA.2011.10.008.

[133] M.J. Mochane, A.S. Luyt, Preparation and properties of polystyrene encapsulated paraffin wax as possible phase change material in a polypropylene matrix, Thermochim. Acta. 544 (2012) 63–70. doi:10.1016/J.TCA.2012.06.017.

[134] F. Fratini, G. Cilia, B. Turchi, A. Felicioli, Beeswax: A minireview of its antimicrobial activity and its application in medicine, Asian Pac. J. Trop. Med. 9 (2016) 839–843. doi:10.1016/J.APJTM.2016.07.003.

[135] E.M. Shchukina, D.G. Shchukin, LbL coated microcapsules for delivering lipid-based drugs, Adv. Drug Deliv. Rev. 63 (2011) 837–846. doi:10.1016/J.ADDR.2011.03.009.

[136] L. Sagalowicz, M.E. Leser, Delivery systems for liquid food products, Curr. Opin. Colloid Interface Sci. 15 (2010) 61–72. doi:10.1016/J.COCIS.2009.12.003.

[137] G. Bortnowska, Multilayer Oil-in-Water Emulsions: Formation, Characteristics and Application as the Carriers for Lipophilic Bioactive Food Components – a Review, Polish J.

Food Nutr. Sci. 65 (2015) 157–166. doi:https://doi.org/10.2478/v10222-012-0094-0.

[138] M.Y. Koroleva, T.Y. Nagovitsina, D.A. Bidanov, O.S. Gorbachevski, E.V. Yurtov, Nano- and microcapsules as drug-delivery systems, Resour. Technol. 2 (2016) 233–239. doi:10.1016/J.REFFIT.2016.10.013.

[139] S. Soradech, I. Petchtubtim, J. Thongdon-A, T. Muangman, Development of Wax-Incorporated Emulsion Gel Beads for the Encapsulation and Intragastric Floating Delivery of the Active Antioxidant from Tamarindus indica L., Mol. . 21 (2016). doi:10.3390/molecules21030380.

[140] A.S. Johns, C.D. Bain, Ink-Jet Printing of High-Molecular-Weight Polymers in Oil-in-Water Emulsions, ACS Appl. Mater. Interfaces. 9 (2017) 22918–22926. doi:10.1021/acsami.7b04454.

[141] E. Sansonetti, B. Andersons, I. Andersone, Novel alkyd-linseed oil emulsion formulations for wood coatings, IOP Conf. Ser. Mater. Sci. Eng. 111 (2016) 12020. doi:10.1088/1757-899X/111/1/012020.

[142] S. Galus, J. Kadzińska, Food applications of emulsion-based edible films and coatings, Trends Food Sci. Technol. 45 (2015) 273–283. doi:10.1016/J.TIFS.2015.07.011.

[143] D.J. McClements, J. Rao, Food-Grade Nanoemulsions: Formulation, Fabrication, Properties, Performance, Biological Fate, and Potential Toxicity, Crit. Rev. Food Sci. Nutr. 51 (2011) 285–330. doi:10.1080/10408398.2011.559558.

[144] T.G. Mason, J.N. Wilking, K. Meleson, C.B. Chang, S.M. Graves, Nanoemulsions: formation, structure, and physical properties, J. Phys. Condens. Matter. 18 (2006) R635–R666. doi:10.1088/0953-8984/18/41/R01.

[145] A. Sharma, V.V. Tyagi, C.R. Chen, D. Buddhi, Review on thermal energy storage with phase change materials and applications, Renew. Sustain. Energy Rev. 13 (2009) 318–345. doi:10.1016/J.RSER.2007.10.005.

[146] T.M. Schutzius, I.S. Bayer, J. Qin, D. Waldroup, C.M. Megaridis, Water-Based, Nonfluorinated Dispersions for Environmentally Benign, Large-Area, Superhydrophobic Coatings, ACS Appl. Mater. Interfaces. 5 (2013) 13419–13425. doi:10.1021/am4043307.

[147] R. Greta, H.J. Alejandro, M.M. T., C. Luca, D. Alexander, C. Riccardo, P. Mirko, B.I. S., A. Athanassia, Highly Effective Antiadhesive Coatings from pH-Modified Water-Dispersed Perfluorinated Acrylic Copolymers: The Case of Vulcanizing Rubber, Adv. Mater. Interfaces. 3 (2016) 1600069. doi:10.1002/admi.201600069.

[148] Gregory BorsingerAbbas Hassan, (12) United States Patent site th still, 2 (2010).

[149] W.M. Gravatt, N.J. Us, C.P. Smith, M.A. Kocur, A. Schwark, (12) United States Patent (10

) Patent No .: (45) Date of Patent : Primary Examiner — Ling Choi, 2 (2016).

[150] C.A. Moody, J.A. Field, Perfluorinated Surfactants and the Environmental Implications of Their Use in Fire-Fighting Foams, Environ. Sci. Technol. 34 (2000) 3864–3870. doi:10.1021/es991359u.

[151] L. Caillier, E. Taffin de Givenchy, R. Levy, Y. Vandenberghe, S. Geribaldi, F. Guittard, Polymerizable semi-fluorinated gemini surfactants designed for antimicrobial materials, J. Colloid Interface Sci. 332 (2009) 201–207. doi:10.1016/J.JCIS.2008.12.038.

[152] A. Dinker, M. Agarwal, G.D. Agarwal, Experimental Study on Thermal Performance of Beeswax as Thermal Storage Material, Mater. Today Proc. 4 (2017) 10529–10533. doi:10.1016/J.MATPR.2017.06.414.

[153] S. Merk, A. Blume, M. Riederer, Phase behaviour and crystallinity of plant cuticular waxes studied by Fourier transform infrared spectroscopy, Planta. 204 (1997) 44–53. doi:10.1007/s004250050228.

[154] V.A. M., B. R., D. G., X-ray photoelectron spectroscopy investigation of pumice-supported nickel catalysts, Surf. Interface Anal. 23 (2018) 239–247. doi:10.1002/sia.740230408.

[155] E. Pierce, F.J. Carmona, A. Amirfazli, Understanding of sliding and contact angle results in tilted plate experiments, Colloids Surfaces A Physicochem. Eng. Asp. 323 (2008) 73–82. doi:10.1016/J.COLSURFA.2007.09.032.

[156] B.S. Yilbas, G. Hassan, A. Al-Sharafi, H. Ali, N. Al-Aqeeli, A. Al-Sarkhi, Water Droplet Dynamics on a Hydrophobic Surface in Relation to the Self-Cleaning of Environmental Dust, Sci. Rep. 8 (2018) 2984. doi:10.1038/s41598-018-21370-5.

[157] O. De Castro, P. Colombo, L. Gianguzzi, R. Perrone, Flower and fruit structure of the endangered species Petagnaea gussonei (Sprengel) Rauschert (Saniculoideae, Apiaceae) and implications for its reproductive biology, Plant Biosyst. - An Int. J. Deal. with All Asp. Plant Biol. 149 (2015) 1042–1051. doi:10.1080/11263504.2015.1014007.

[158] W. Su, J. Darkwa, G. Kokogiannakis, Review of solid–liquid phase change materials and their encapsulation technologies, Renew. Sustain. Energy Rev. 48 (2015) 373–391. doi:10.1016/J.RSER.2015.04.044.

[159] T.A. P., H.L. L., Canadian beeswax: Analytical values and composition of hydrocarbons, free acids and long chain esters, J. Am. Oil Chem. Soc. 49 (1972) 696–699. doi:10.1007/BF02609202.

[160] Y. Gaillard, A. Mija, A. Burr, E. Darque-Ceretti, E. Felder, N. Sbirrazzuoli, Green material composites from renewable resources: Polymorphic transitions and phase diagram of beeswax/rosin resin, Thermochim. Acta. 521 (2011) 90–97. doi:10.1016/J.TCA.2011.04.010.

[161] A.A. Attama, B.C. Schicke, C.C. Müller-Goymann, Further characterization of theobroma oil–beeswax admixtures as lipid matrices for improved drug delivery systems, Eur. J. Pharm. Biopharm. 64 (2006) 294–306. doi:10.1016/J.EJPB.2006.06.010.

[162] R. Buchwald, M.D. Breed, A.R. Greenberg, The thermal properties of beeswaxes: unexpected findings, J. Exp. Biol. 211 (2008) 121 LP-127. http://jeb.biologists.org/content/211/1/121.abstract.

[163] H.W. Starkweather, P. Zoller, G.A. Jones, The heat of fusion of poly(ethylene terephthalate), J. Polym. Sci. Polym. Phys. Ed. 21 (2018) 295–299. doi:10.1002/pol.1983.180210211.

[164] M. Regert, S. Colinart, L. Degrand, O. Decavallas, Chemical Alteration and Use of Beeswax Through Time: Accelerated Ageing Tests and Analysis of Archaeological Samples from Various Environmental Contexts, Archaeometry. 43 (2001) 549–569. doi:10.1111/1475-4754.00036.

[165] F.L. Tan, S.C. Fok, Cooling of helmet with phase change material, Appl. Therm. Eng. 26 (2006) 2067–2072. doi:10.1016/J.APPLTHERMALENG.2006.04.022.

[166] B. Li, T. Liu, L. Hu, Y. Wang, L. Gao, Fabrication and Properties of Microencapsulated Paraffin@SiO2 Phase Change Composite for Thermal Energy Storage, ACS Sustain. Chem. Eng. 1 (2013) 374–380. doi:10.1021/sc300082m.

[167] A.M. Youssef, S.M. EL-Sayed, H.S. EL-Sayed, H.H. Salama, A. Dufresne, Enhancement of Egyptian soft white cheese shelf life using a novel chitosan/carboxymethyl cellulose/zinc oxide bionanocomposite film, Carbohydr. Polym. 151 (2016) 9–19. doi:10.1016/J.CARBPOL.2016.05.023.

[168] I.S. Bayer, A. Steele, P.J. Martorana, E. Loth, L. Miller, Superhydrophobic cellulose-based bionanocomposite films from Pickering emulsions, Appl. Phys. Lett. 94 (2009) 163902. doi:10.1063/1.3120548.

[169] J.B. Binder, J.J. Blank, A. V Cefali, R.T. Raines, Synthesis of Furfural from Xylose and Xylan, ChemSusChem. 3 (2010) 1268–1272. doi:10.1002/cssc.201000181.

[170] G. Nanni, A.J. Heredia-Guerrero, C.U. Paul, S. Dante, G. Caputo, C. Canale, A. Athanassiou, D. Fragouli, S.I. Bayer, Poly(furfuryl alcohol)-Polycaprolactone Blends, Polym. . 11 (2019). doi:10.3390/polym11061069.

[171] S. Vishwanatham, N. Haldar, Furfuryl alcohol as corrosion inhibitor for N80 steel in hydrochloric acid, Corros. Sci. 50 (2008) 2999–3004. doi:10.1016/J.CORSCI.2008.08.005.

[172] FURFURYL ALCOHOL RESINS ARE PROMINENT IN CORROSION RESISTANT CONSTRUCTION, Chem. Eng. News Arch. 31 (1953) 4475. doi:10.1021/cen-v031n043.p4475.

[173] P. Luckeneder, J. Gavino, R. Kuchernig, A. Petutschnigg, G. Tondi, Sustainable Phenolic Fractions as Basis for Furfuryl Alcohol-Based Co-Polymers and Their Use as Wood Adhesives, Polym. . 8 (2016). doi:10.3390/polym8110396.

[174] H. Wang, J. Yao, Use of Poly(furfuryl alcohol) in the Fabrication of Nanostructured Carbons and Nanocomposites, Ind. Eng. Chem. Res. 45 (2006) 6393–6404. doi:10.1021/ie0602660.

[175] L. He, D. Li, G. Zhang, P.A. Webley, D. Zhao, H. Wang, Synthesis of Carbonaceous Poly(furfuryl alcohol) Membrane for Water Desalination, Ind. Eng. Chem. Res. 49 (2010) 4175–4180. doi:10.1021/ie901886c.

[176] H.Y. Ling, Z. Su, H. Chen, L. Hencz, M. Zhang, Y. Tang, S. Zhang, Biomass-Derived Poly(Furfuryl Alcohol)–Protected Aluminum Anode for Lithium-Ion Batteries, Energy Technol. 0 (2018). doi:10.1002/ente.201800995.

[177] E.A. Melo-Espinosa, Y. Sánchez-Borroto, M. Errasti, R. Piloto-Rodríguez, R. Sierens, J. Roger-Riba, A. Christopher-Hansen, Surface Tension Prediction of Vegetable Oils Using Artificial Neural Networks and Multiple Linear Regression, Energy Procedia. 57 (2014) 886–895. doi:10.1016/J.EGYPRO.2014.10.298.

[178] B. Esteban, J.-R. Riba, G. Baquero, R. Puig, A. Rius, Characterization of the surface tension of vegetable oils to be used as fuel in diesel engines, Fuel. 102 (2012) 231–238. doi:10.1016/J.FUEL.2012.07.042.

[179] Z. Chu, Y. Feng, S. Seeger, Oil/Water Separation with Selective Superantiwetting/Superwetting Surface Materials, Angew. Chemie Int. Ed. 54 (2015) 2328–2338. doi:10.1002/anie.201405785.

[180] S. Nishimoto, B. Bhushan, Bioinspired self-cleaning surfaces with superhydrophobicity, superoleophobicity, and superhydrophilicity, RSC Adv. 3 (2013) 671–690. doi:10.1039/C2RA21260A.

[181] M.J. Nine, M.A. Cole, L. Johnson, D.N.H. Tran, D. Losic, Robust Superhydrophobic Graphene-Based Composite Coatings with Self-Cleaning and Corrosion Barrier Properties, ACS Appl. Mater. Interfaces. 7 (2015) 28482–28493. doi:10.1021/acsami.5b09611.

[182] G. Wang, H. Wang, Z. Guo, A robust transparent and anti-fingerprint superhydrophobic film, Chem. Commun. 49 (2013) 7310–7312. doi:10.1039/C3CC43677B.

[183] N. Ke, X. Wang, X. Xu, Y.A. Abassi, The xCELLigence System for Real-Time and Label-Free Monitoring of Cell Viability BT - Mammalian Cell Viability: Methods and Protocols, in: M.J. Stoddart (Ed.), Humana Press, Totowa, NJ, 2011: pp. 33–43. doi:10.1007/978-1-61779-108-6_6.

[184] C.L. Burket, R. Rajagopalan, A.P. Marencic, K. Dronvajjala, H.C. Foley, Genesis of porosity

in polyfurfuryl alcohol derived nanoporous carbon, Carbon N. Y. 44 (2006) 2957–2963. doi:10.1016/J.CARBON.2006.05.029.

[185] M. Choura, N.M. Belgacem, A. Gandini, Acid-Catalyzed Polycondensation of Furfuryl Alcohol: Mechanisms of Chromophore Formation and Cross-Linking, Macromolecules. 29 (1996) 3839–3850. doi:10.1021/ma951522f.

[186] S. Yu, H. Li, Fabrication of superhydrophobic and oleophobic zinc coating on steel surface, Mater. Sci. Technol. 33 (2017) 1290–1297. doi:10.1080/02670836.2017.1288675.

[187] M. Sedlaček, B. Podgornik, J. Vižintin, Correlation between standard roughness parameters skewness and kurtosis and tribological behaviour of contact surfaces, Tribol. Int. 48 (2012) 102–112. doi:10.1016/J.TRIBOINT.2011.11.008.

[188] E.S. Gadelmawla, M.M. Koura, T.M.A. Maksoud, I.M. Elewa, H.H. Soliman, Roughness parameters, J. Mater. Process. Technol. 123 (2002) 133–145. doi:10.1016/S0924-0136(02)00060-2.

[189] A. Larsson, The interaction between a lightning flash and an aircraft in flight, Comptes Rendus Phys. 3 (2002) 1423–1444. doi:10.1016/S1631-0705(02)01410-X.

[190] J. Han, H. Zhang, M. Chen, D. Wang, Q. Liu, Q. Wu, Z. Zhang, The combination of carbon nanotube buckypaper and insulating adhesive for lightning strike protection of the carbon fiber/epoxy laminates, Carbon N. Y. 94 (2015) 101–113. doi:10.1016/J.CARBON.2015.06.026.

[191] D.K. Chakravarthi, V.N. Khabashesku, R. Vaidyanathan, J. Blaine, S. Yarlagadda, D. Roseman, Q. Zeng, E. V. Barrera, Carbon Fiber-Bismaleimide Composites Filled with Nickel-Coated Single-Walled Carbon Nanotubes for Lightning-Strike Protection, Adv. Funct. Mater. 21 (2011) 2527–2533. doi:10.1002/adfm.201002442.

[192] M. Gagné, D. Therriault, Lightning strike protection of composites, Prog. Aerosp. Sci. 64 (2014) 1–16. doi:10.1016/J.PAEROSCI.2013.07.002.

[193] A. Katunin, K. Krukiewicz, A. Herega, G. Catalanotti, CONCEPT OF A CONDUCTING COMPOSITE MATERIAL FOR LIGHTNING STRIKE PROTECTION, (n.d.). doi:10.1515/adms-2016-0007.

[194] R. Qian, J. Yu, C. Wu, X. Zhai, P. Jiang, Alumina-coated graphene sheet hybrids for electrically insulating polymer composites with high thermal conductivity, RSC Adv. 3 (2013) 17373–17379. doi:10.1039/C3RA42104J.

[195] Z. Shen, J. Feng, Highly Thermally Conductive Composite Films Based on Nanofibrillated Cellulose in Situ Coated with a Small Amount of Silver Nanoparticles, ACS Appl. Mater. Interfaces. 10 (2018) 24193–24200. doi:10.1021/acsami.8b07249.

[196] J. Che, M. Jing, D. Liu, K. Wang, Q. Fu, Largely enhanced thermal conductivity of HDPE/boron nitride/carbon nanotubes ternary composites via filler network-network synergy and orientation, Compos. Part A Appl. Sci. Manuf. 112 (2018) 32–39. doi:10.1016/J.COMPOSITESA.2018.05.016.

[197] S.Y. Kim, Y.J. Noh, J. Yu, Thermal conductivity of graphene nanoplatelets filled composites fabricated by solvent-free processing for the excellent filler dispersion and a theoretical approach for the composites containing the geometrized fillers, Compos. Part A Appl. Sci. Manuf. 69 (2015) 219–225. doi:10.1016/J.COMPOSITESA.2014.11.018.

[198] P. Cataldi, A. Athanassiou, I.S. Bayer, Graphene Nanoplatelets-Based Advanced Materials and Recent Progress in Sustainable Applications, Appl. Sci. 8 (2018). doi:10.3390/app8091438.

[199] K. Pashayi, H.R. Fard, F. Lai, S. Iruvanti, J. Plawsky, T. Borca-Tasciuc, High thermal conductivity epoxy-silver composites based on self-constructed nanostructured metallic networks, J. Appl. Phys. 111 (2012) 104310. doi:10.1063/1.4716179.

[200] C. Yu, W. Gong, W. Tian, Q. Zhang, Y. Xu, Z. Lin, M. Hu, X. Fan, Y. Yao, Hot-pressing induced alignment of boron nitride in polyurethane for composite films with thermal conductivity over 50 Wm−1 K−1, Compos. Sci. Technol. 160 (2018) 199–207. doi:10.1016/j.compscitech.2018.03.028.

[201] L. Ren, Q. Li, J. Lu, X. Zeng, R. Sun, J. Wu, J.-B. Xu, C.-P. Wong, Enhanced thermal conductivity for Ag-deposited alumina sphere/epoxy resin composites through manipulating interfacial thermal resistance, Compos. Part A Appl. Sci. Manuf. 107 (2018) 561–569. doi:10.1016/J.COMPOSITESA.2018.02.010.

[202] S. Yu, H. Jung, J. Lee, G. Song, J.H. Choi, C. Park, High performance thermal conduction of silver microparticles thermos-compressed in three-dimensionally interconnected polystyrene beads, Int. J. Nanotechnol. 13 (2016) 376–384. doi:10.1504/IJNT.2016.077087.

[203] X. Huang, P. Jiang, L. Xie, Ferroelectric polymer/silver nanocomposites with high dielectric constant and high thermal conductivity, Appl. Phys. Lett. 95 (2009) 242901. doi:10.1063/1.3273368.

[204] C.-H. Xue, J. Chen, W. Yin, S.-T. Jia, J.-Z. Ma, Superhydrophobic conductive textiles with antibacterial property by coating fibers with silver nanoparticles, Appl. Surf. Sci. 258 (2012) 2468–2472. doi:10.1016/J.APSUSC.2011.10.074.

[205] W. Liang, L. Wang, Z. Zhu, C. Qian, H. Sun, B. Yang, A. Li, In Situ Preparation of Polyethylene Glycol/ Silver Nanoparticles Composite Phase Change Materials with Enhanced Thermal Conductivity, ChemistrySelect. 2 (2017) 3428–3436.

doi:10.1002/slct.201700381.

[206] L. Qi, Z. Liu, N. Wang, Y. Hu, Facile and efficient in situ synthesis of silver nanoparticles on diverse filtration membrane surfaces for antimicrobial performance, Appl. Surf. Sci. 456 (2018) 95–103. doi:10.1016/J.APSUSC.2018.06.066.

[207] K. Zou, Q. Liu, J. Chen, J. Du, Silver-decorated biodegradable polymer vesicles with excellent antibacterial efficacy, Polym. Chem. 5 (2014) 405–411. doi:10.1039/C3PY00966A.

[208] S. Nishimura, D. Mott, A. Takagaki, S. Maenosono, K. Ebitani, Role of base in the formation of silver nanoparticles synthesized using sodium acrylate as a dual reducing and encapsulating agent, Phys. Chem. Chem. Phys. 13 (2011) 9335–9343. doi:10.1039/C0CP02985H.

[209] Y.M. Yukhin, A.I. Titkov, G.K. Kulmukhamedov, N.Z. Lyakhov, Synthesis of silver nanoparticles via reduction of silver carboxylates by ethylene glycol, Theor. Found. Chem. Eng. 49 (2015) 490–496. doi:10.1134/S004057951504020X.

[210] Q. Chen, G. Liu, G. Chen, T. Mi, J. Tai, Green Synthesis of Silver Nanoparticles with Glucose for Conductivity Enhancement of Conductive Ink, Bioresour. Vol 12, No 1. (2016). http://ojs.cnr.ncsu.edu/index.php/BioRes/article/view/BioRes_12_1_608_Chen_Green_Synthesis_Silver_Nanoparticles.

[211] M. Darroudi, M.B. Ahmad, A.K. Zak, R. Zamiri, M. Hakimi, Fabrication and characterization of gelatin stabilized silver nanoparticles under UV-light, Int. J. Mol. Sci. 12 (2011) 6346–6356. doi:10.3390/ijms12096346.

[212] Y. Sun, Y. Xia, Large-Scale Synthesis of Uniform Silver Nanowires Through a Soft, Self-Seeding, Polyol Process, Adv. Mater. 14 (2002) 833–837. doi:10.1002/1521-4095(20020605)14:11<833::AID-ADMA833>3.0.CO;2-K.

[213] Y. Zhou, X. Zhuang, F. Wu, F. Liu, High-Performance Thermal Management Nanocomposites: Silver Functionalized Graphene Nanosheets and Multiwalled Carbon Nanotube, (2018). doi:10.20944/PREPRINTS201808.0290.V1.

[214] J. Liang, M.C. Saha, M.C. Altan, Effect of Carbon Nanofibers on Thermal Conductivity of Carbon Fiber Reinforced Composites, Procedia Eng. 56 (2013) 814–820. doi:10.1016/J.PROENG.2013.03.201.

[215] J. Gou, Y. Tang, F. Liang, Z. Zhao, D. Firsich, J. Fielding, Carbon nanofiber paper for lightning strike protection of composite materials, Compos. Part B Eng. 41 (2010) 192–198. doi:10.1016/J.COMPOSITESB.2009.06.009.

[216] M.B. Jakubinek, M.A. White, M. Mu, K.I. Winey, Temperature dependence of thermal conductivity enhancement in single-walled carbon nanotube/polystyrene composites, Appl.

Phys. Lett. 96 (2010) 83105. doi:10.1063/1.3323095.

[217] J. Chen, B. Liu, X. Gao, D. Xu, A review of the interfacial characteristics of polymer nanocomposites containing carbon nanotubes, RSC Adv. 8 (2018) 28048–28085. doi:10.1039/C8RA04205E.

[218] A. Lakshmanan, S. Srivastava, A. Ramazani, V. Sundararaghavan, Thermal conductivity of pillared graphene-epoxy nanocomposites using molecular dynamics, Appl. Phys. Lett. 112 (2018) 151902. doi:10.1063/1.5022755.

[219] B. Zhang, S.A. Soltani, L.N. Le, R. Asmatulu, Fabrication and assessment of a thin flexible surface coating made of pristine graphene for lightning strike protection, Mater. Sci. Eng. B. 216 (2017) 31–40. doi:10.1016/J.MSEB.2017.02.008.

[220] L. He, H. Wang, H. Zhu, Y. Gu, X. Li, X. Mao, Thermal Properties of PEG/Graphene Nanoplatelets (GNPs) Composite Phase Change Materials with Enhanced Thermal Conductivity and Photo-Thermal Performance, Appl. Sci. . 8 (2018). doi:10.3390/app8122613.

[221] M. Zahid, M.T. Masood, A. Athanassiou, I.S. Bayer, Sustainable thermal interface materials from recycled cotton textiles and graphene nanoplatelets, 113 (2018) 44103. doi:10.1063/1.5044719.

[222] H. Zhao, J. Bai, Highly Sensitive Piezo-Resistive Graphite Nanoplatelet–Carbon Nanotube Hybrids/Polydimethylsilicone Composites with Improved Conductive Network Construction, ACS Appl. Mater. Interfaces. 7 (2015) 9652–9659. doi:10.1021/acsami.5b01413.

[223] W.G.I.U. Rathnayake, H. Ismail, A. Baharin, A.G.N.D. Darsanasiri, S. Rajapakse, Synthesis and characterization of nano silver based natural rubber latex foam for imparting antibacterial and anti-fungal properties, Polym. Test. 31 (2012) 586–592. doi:10.1016/J.POLYMERTESTING.2012.01.010.

[224] J. Pinto, D. Magrì, P. Valentini, F. Palazon, J.A. Heredia-Guerrero, S. Lauciello, S. Barroso-Solares, L. Ceseracciu, P.P. Pompa, A. Athanassiou, D. Fragouli, Antibacterial Melamine Foams Decorated with in Situ Synthesized Silver Nanoparticles, ACS Appl. Mater. Interfaces. 10 (2018) 16095–16104. doi:10.1021/acsami.8b01442.

[225] Z. Lu, J. Xiao, Y. Wang, M. Meng, In situ synthesis of silver nanoparticles uniformly distributed on polydopamine-coated silk fibers for antibacterial application, J. Colloid Interface Sci. 452 (2015) 8–14. doi:10.1016/J.JCIS.2015.04.015.

[226] P. Cataldi, L. Ceseracciu, A. Athanassiou, I.S. Bayer, Healable Cotton-Graphene Nanocomposite Conductor for Wearable Electronics, ACS Appl. Mater. Interfaces. 9 (2017) 13825–13830. doi:10.1021/acsami.7b02326.

[227] M. Zahid, E.L. Papadopoulou, A. Athanassiou, I.S. Bayer, Strain-responsive mercerized conductive cotton fabrics based on PEDOT:PSS/graphene, Mater. Des. 135 (2017). doi:10.1016/j.matdes.2017.09.026.

[228] J.F. Gomes, A.C. Garcia, E.B. Ferreira, C. Pires, V.L. Oliveira, G. Tremiliosi-Filho, L.H.S. Gasparotto, New insights into the formation mechanism of Ag, Au and AgAu nanoparticles in aqueous alkaline media: alkoxides from alcohols, aldehydes and ketones as universal reducing agents, Phys. Chem. Chem. Phys. 17 (2015) 21683–21693. doi:10.1039/C5CP02155C.

[229] L. Qi, Z. Liu, N. Wang, Y. Hu, Facile and efficient in situ synthesis of silver nanoparticles on diverse filtration membrane surfaces for antimicrobial performance, Appl. Surf. Sci. 456 (2018) 95–103. doi:10.1016/J.APSUSC.2018.06.066.

[230] A. Fahmy, W.H. Eisa, M. Yosef, A. Hassan, Ultra-Thin Films of Poly(acrylic acid)/Silver Nanocomposite Coatings for Antimicrobial Applications, J. Spectrosc. 2016 (2016) 1–11. doi:10.1155/2016/7489536.

[231] S. Chalal, N. Haddadine, N. Bouslah, A. Benaboura, Preparation of Poly(acrylic acid)/silver nanocomposite by simultaneous polymerization-reduction approach for antimicrobial application, J. Polym. Res. 19 (2012). doi:10.1007/s10965-012-0024-1.

[232] V. de A.M. Gonzaga, B.A. Chrisostomo, A.L. Poli, C.C. Schmitt, Preparation, Characterization and Photostability of Nanocomposite Films Based on Poly(acrylic acid) and Montmorillonite, Mater. Res. 21 (2018). doi:10.1590/1980-5373-mr-2017-1024.

[233] A. Fahmy, W.H. Eisa, A.M.A. Hassan, Electrosprayed of Polyacrylic Acid / Silver Nanocomposite Thin Films and its Antimicrobial Application Electrosprayed of Polyacrylic Acid / Silver Nanocomposite Thin Films and its, (2015).

[234] A.J. Ryan, W. Bras, G.R. Mant, G.E. Derbyshire, A direct method to determine the degree of crystallinity and lamellar thickness of polymers: application to polyethylene, Polymer (Guildf). 35 (1994) 4537–4544. doi:10.1016/0032-3861(94)90799-4.

[235] E. SEGERMAN, P.G. STERN, Two-phase Model for Structure of Polymers, Nature. 210 (1966) 1258–1259. doi:10.1038/2101258a0.

[236] B. Jiang, B. Peng, A. Zhu, C. Zhang, Y. Li, Eco-friendly synthesis of graphene nanoplatelets via a carbonation route and its reinforcement for polytetrafluoroethylene composites, J. Mater. Sci. 53 (2018) 626–636. doi:10.1007/s10853-017-1526-3.

[237] S. He, J. Zhang, X. Xiao, X. Hong, Effects of ultrasound vibration on the structure and properties of polypropylene/graphene nanoplatelets composites, Polym. Eng. Sci. 58 (2018) 377–386. doi:10.1002/pen.24584.

[238] P. Cataldi, L. Ceseracciu, S. Marras, A. Athanassiou, I.S. Bayer, Electrical conductivity enhancement in thermoplastic polyurethane-graphene nanoplatelet composites by stretch-release cycles, Appl. Phys. Lett. 110 (2017) 121904. doi:10.1063/1.4978865.

[239] S. Lee, J.-Y. Hong, J. Jang, The effect of graphene nanofiller on the crystallization behavior and mechanical properties of poly(vinyl alcohol), Polym. Int. 62 (2013) 901–908. doi:10.1002/pi.4370.

[240] E.L. Heeley, D.J. Hughes, P.G. Taylor, A.R. Bassindale, Crystallization and morphology development in polyethylene–octakis(n-octadecyldimethylsiloxy)octasilsesquioxane nanocomposite blends, RSC Adv. 5 (2015) 34709–34719. doi:10.1039/C5RA03267A.

[241] K.J. Lee, J. Lee, J.-Y. Hong, J. Jang, Influence of amorphous polymer nanoparticles on the crystallization behavior of poly(vinyl alcohol) nanocomposites, Macromol. Res. 17 (2009) 476–482. doi:10.1007/BF03218895.

[242] C. Monteserín, M. Blanco, E. Aranzabe, A. Aranzabe, J.M. Laza, A. Larrañaga-Varga, J.L. Vilas, Effects of Graphene Oxide and Chemically-Reduced Graphene Oxide on the Dynamic Mechanical Properties of Epoxy Amine Composites, Polym. . 9 (2017). doi:10.3390/polym9090449.

[243] J. Hu, Y. Huang, Y. Yao, G. Pan, J. Sun, X. Zeng, R. Sun, J.-B. Xu, B. Song, C.-P. Wong, Polymer Composite with Improved Thermal Conductivity by Constructing a Hierarchically Ordered Three-Dimensional Interconnected Network of BN, ACS Appl. Mater. Interfaces. 9 (2017) 13544–13553. doi:10.1021/acsami.7b02410.

[244] J.M.A.R.B. Jayasinghe, R.T. De Silva, R.M. de Silva, K.M.N. de Silva, M.M.M.G.P.G. Mantilaka, V.A. Silva, Effect of networked hybridized nanoparticle reinforcement on the thermal conductivity and mechanical properties of natural rubber composites, RSC Adv. 9 (2019) 636–644. doi:10.1039/C8RA08543A.

[245] C. Hopmann, C. Windeck, A. Cohnen, J. Onken, B. Krause, P. Pötschke, T. Hickmann, Development of a polymer composite with high electrical conductivity and improved impact strength for the application as bipolar plate, AIP Conf. Proc. 1779 (2016) 30017. doi:10.1063/1.4965487.

[246] J. Zhou, G. Lubineau, Improving Electrical Conductivity in Polycarbonate Nanocomposites Using Highly Conductive PEDOT/PSS Coated MWCNTs, ACS Appl. Mater. Interfaces. 5 (2013) 6189–6200. doi:10.1021/am4011622.

[247] P.-C. Ma, M.-Y. Liu, H. Zhang, S.-Q. Wang, R. Wang, K. Wang, Y.-K. Wong, B.-Z. Tang, S.-H. Hong, K.-W. Paik, J.-K. Kim, Enhanced Electrical Conductivity of Nanocomposites Containing Hybrid Fillers of Carbon Nanotubes and Carbon Black, ACS Appl. Mater.

Interfaces. 1 (2009) 1090–1096. doi:10.1021/am9000503.

[248] R.D. Farahani, J.E. Klemberg-Sapieha, D. Therriault, Enhanced conductivity of nanocomposite films through heterogeneous distribution of nanofillers during processing, Mater. Des. 88 (2015) 1175–1182. doi:10.1016/J.MATDES.2015.09.088.

[249] H. Wu, L.T. Drzal, Graphene nanoplatelet paper as a light-weight composite with excellent electrical and thermal conductivity and good gas barrier properties, Carbon N. Y. 50 (2012) 1135–1145. doi:10.1016/j.carbon.2011.10.026.

[250] J. Wang, F. Ma, M. Sun, Graphene, hexagonal boron nitride, and their heterostructures: properties and applications, RSC Adv. 7 (2017) 16801–16822. doi:10.1039/c7ra00260b.

[251] R. Jan, A. Habib, H.Y. Abbasi, High aspect ratio graphene nanosheets cause a very low percolation threshold for polymer nanocomposites, Acta Phys. Pol. A. 129 (2016) 478–481. doi:10.12693/APhysPolA.129.478.

[252] M. Bhattacharya, Polymer nanocomposites-A comparison between carbon nanotubes, graphene, and clay as nanofillers, Materials (Basel). 9 (2016) 1–35. doi:10.3390/ma9040262.

[253] Y. Li, H. Zhang, Y. Liu, H. Wang, Z. Huang, T. Peijs, E. Bilotti, Synergistic effects of spray-coated hybrid carbon nanoparticles for enhanced electrical and thermal surface conductivity of CFRP laminates, Compos. Part A Appl. Sci. Manuf. 105 (2018) 9–18. doi:10.1016/J.COMPOSITESA.2017.10.032.

[254] S. Iyahraja, J.S. Rajadurai, Study of thermal conductivity enhancement of aqueous suspensions containing silver nanoparticles, AIP Adv. 5 (2015) 57103. doi:10.1063/1.4919808.

[255] A. Gupta, R. Kumar, Role of Brownian motion on the thermal conductivity enhancement of nanofluids, Appl. Phys. Lett. 91 (2007) 223102. doi:10.1063/1.2816903.

[256] K. V Wong, M.J. Castillo, Heat Transfer Mechanisms and Clustering in Nanofluids, Adv. Mech. Eng. 2 (2010) 795478. doi:10.1155/2010/795478.